

**Synthesis, Growth and Characterization  
of Oxide Phosphors for Thin Film  
Electroluminescent Devices**

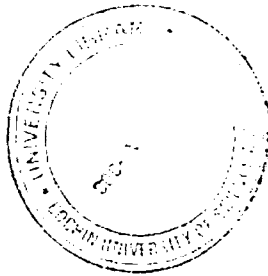
Thesis submitted to  
**COCHIN UNIVERSITY OF SCIENCE AND TECHNOLOGY**  
in partial fulfillment of the requirements  
for the award of the degree of  
**DOCTOR OF PHILOSOPHY**

**Anoop G**

**Department of Physics  
Cochin University of Science and Technology  
Kochi - 682 022, Kerala, India**

**December 2008**

T 250



## **Synthesis, Growth and Characterization of Oxide Phosphors for Thin Film Electroluminescent Devices**

*Ph.D thesis in the field of materials science*

*Author:*

Anoop G  
Optoelectronic Devices Laboratory  
Department of Physics  
Cochin University of Science and Technology  
Kochi – 682 022, Kerala, India  
email: anoopnemom@gmail.com

T  
539.232  
fno

*Supervisor:*

Dr. M.K. Jayaraj  
Reader  
Optoelectronics Device Laboratory  
Department of Physics  
Cochin University of Science and Technology  
Cochin – 682 022, Kerala, India  
email: mkj@cusat.ac.in

Back cover: Photograph of Alternating current thin film electroluminescent device fabricated using  $\text{ZnGa}_2\text{O}_4:\text{Mn}$  active layer.

December 2008

**Dr. M.K. Jayaraj**

Reader

Department of Physics

Cochin University of Science and Technology

Kochi – 682 022

---

3<sup>rd</sup> December 2008

## **Certificate**

Certified that the work presented in this thesis entitled “*Synthesis, Growth and Characterization of Oxide Phosphors for Thin Film Electroluminescent Devices*” is based on the authentic record of research done by Mr. Anoop G under my guidance in the Department of Physics, Cochin University of Science and Technology, Kochi – 682 022 and has not been included in any other thesis submitted for the award of any degree.



Dr. M. K. Jayaraj

(Supervising Guide)

---

Phone : +91 484 2577404 extn 33 Fax: 91 484 2577595 email: [mkj@cusat.ac.in](mailto:mkj@cusat.ac.in)

## Declaration

Certified that the work presented in this thesis entitled "*Synthesis, Growth and Characterization of Oxide Phosphors for Thin Film Electroluminescent Devices*" is based on the original research work done by me under the supervision and guidance of Dr. M. K. Jayaraj, Reader, Department of Physics, Cochin University of Science and Technology, Cochin-682022 has not been included in any other thesis submitted previously for the award of any degree.

Kochi – 22  
3<sup>rd</sup> December 2008



Anoop G

---

## Acknowledgements

---

*A journey is easier when we travel together. Interdependence is certainly more valuable than independence. This thesis is the result of four years of work, whereby I have been accompanied and supported by many people. It is a pleasant aspect that I have now the opportunity to express my gratitude for all of them.*

*First and foremost, my heartily profound thanks and appreciation are addressed to my Ph.D advisor, Dr. M. K. Jayaraj, Reader, Department of Physics, Cochin University of Science and Technology. I express my deep sense of gratitude for his excellent guidance, competent advice, keen observations and persistent encouragement given to me during the entire course of work, without which the successful completion of this work would not have been possible. I owe him lots of gratitude for having me shown this way of research.*

*I would like to express my sincere gratitude to Prof. Godfrey Louis, Head of the Department and all the former Heads of the Department - Prof. K. P. Vijayakumar, Prof. V. C. Kuriakose and Prof. Ramesh Babu Thayyullathil - for permitting me to use the facilities in the Department of Physics, CUSAT. I also gratefully acknowledge the help and inspiration from all the other faculty members of the Department of Physics.*

*I specially express my sincere gratitude to Dr. M. R. Anantharaman sir (Reader, Department of Physics, CUSAT) for his personal care and attention shown to me.*

*With pleasure, I acknowledge Prof. V Unnikrishnan Nayar, Dean, Faculty of Science, Cochin University of Science and Technology, former Professor & Head, Dept. of Optoelectronics, University of Kerala and Dr. V. P. Mahadevan Pillai, Professor and Head, Dept. of Optoelectronics, University of Kerala for their encouragement and guidance right from my M.Phil class.*

*I am deeply indebted to all my teachers especially Dr. K. Mohanan Pillai (Principal, D. B. Pampa college, Parumala) and my Jayasree teacher (Lecturer in Physics, D. B. College, Thalayolaparampu), who really inspired me to pursue career in research with timely advices.*

*I specially acknowledge Dr. K. Manzoor, Assistant Professor, Amritha Institute of Medical Sciences for his valuable suggestions and help during the final stage of my research work. Also I thank Mr. Saji, Amritha Institute of Medical Sciences for EDX measurements.*

*I owe a lot to my brother, Ajimsha for his sincere support, encouragement and holding my temper through out.*

*I would like to thank my dear friend and colleague Mini for her selfless support, fruitful discussions especially in understanding physics behind anything and full-hearted fiscal support whenever I was in financial trouble during my research days at cusat.*

*I am grateful to my Joshy sir and family for their constant encouragement, support, timely advices and for always remembering me and my family in their prayers.*

*Also I thank Anila teacher for her sincere love and care that had shown to me.*

*I express my sincere thanks to Saji who had been always there with me especially in understanding many experimental as well as theoretical problems during my research.*

*I remember with gratitude the sincere support of Dr. Aldrin and Dr. Manoj for all the guidance offered during the initial stages of my research.*

*I would like to express my sincere appreciation to my colleagues in the OED lab Reshmi, Aneesh, Arun, Ratheesh, Krishna Prasad, Sanal, Sreeja, Ragitha, Vineetha, Rahana, Nisha, Asha, Vanaja teacher and James Sir for all the help they had extended.*

*I am thankful to all office (present and former) and library staff of the Department of Physics, office staff of CELOS and the technical staff at VSIC for all the help and cooperation.*

*Now its time to remember my friends, Sibi, Sreeprasanth, Aswathy, Anjana, Nissy, Krishnan, Sreejith Pisharody, Raj Mohan, Renjith and Swarish for the love and care that they had showered to me. Also I remember every moment I spent with my friends-Manu Punnen, Sajeevettan, Jijo, Sagar, Hysen, Ratheesh, Kishore, Sreekumar (Solar), Radhakrishnan and Chithira during my research life at cusat. I specially*

*acknowledge Swapnechi and Unniyettan for their affection shown to me and my family.*

*My deepest feelings of gratitude are directed to my teachers who had inspired me.*

*It is my proud privilege to remember my parents, brother Aneesh and in-laws for their selfless support, motivation, encouragements, patience and tolerance throughout.*

*Last but not least, I have been fortunate with my better half, Rani who is there for me always with patience and prayers.*

*I express my sincere thanks to Department of Science and Technology and Centre for Excellence in Lasers and Optoelectronic Sciences (CELOS) for financial support at various levels of my Ph.D program.*

*I thank all my well wishers.*

*The chain of my gratitude would be definitely incomplete if I would forget to thank the first cause of this chain, using Aristotle's words, The Prime Mover.*

*Anoop G*

<i>Preface</i>	<i>i</i>
<b>CHAPTER 1</b>	
<b>An introduction to electroluminescence and oxide phosphors</b>	
<i>1.1 Introduction</i>	<i>5</i>
<i>1.2 Electroluminescence</i>	<i>8</i>
<i>1.3 EL device structure</i>	<i>9</i>
<i>1.4 Ideal ACTFEL device</i>	<i>10</i>
<i>1.5 The EL mechanism</i>	<i>12</i>
<i>1.6 Space charge in EL devices</i>	<i>15</i>
<i>1.7 ACTFEL materials</i>	<i>18</i>
<i>1.7.1 Substrate</i>	<i>18</i>
<i>1.7.2 Electrodes</i>	<i>18</i>
<i>1.7.3 Insulators</i>	<i>19</i>
<i>1.7.4 Phosphor layer</i>	<i>20</i>
<i>1.8 Oxide Phosphors</i>	<i>22</i>
<i>1.9 Zinc gallium oxide- ZnGa<sub>2</sub>O<sub>4</sub></i>	<i>24</i>
<i>1.9.1 Crystal structure</i>	<i>25</i>

1.9.2 Photoluminescence	26
1.10 Zinc germanate- $Zn_2GeO_4$	33
1.11 Yttrium Oxide- $Y_2O_3$	34
1.11.1 Crystal structure	35
1.11.2 Photoluminescence	36
References	38
<b>CHAPTER 2</b>	
<b>Experimental techniques and characterization tools</b>	
2.1 Bulk synthesis techniques	53
2.2 Thin film growth techniques	55
2.2.1 Thermal evaporation by resistive heating	55
2.2.2 Sputtering	56
2.2.3 Sputtering parameters	59
(a) Sputtering gas	59
(b) Sputtering power	61
(c) Ground shields	61
(d) Target cooling	62
(e) Control of sputtering parameters	63
2.2.4 Pulsed laser deposition (PLD)	64

<i>2.3 Device Fabrication</i>	70
<i>2.4 Characterization tools</i>	71
<i>2.4.1 Thin film thickness</i>	71
<i>2.4.2 Structural characterization</i>	72
<i>2.4.3 Morphological analysis</i>	74
<i>(a) Scanning electron microscope (SEM)</i>	74
<i>(b) Atomic force microscope (AFM)</i>	76
<i>2.4.4 Compositional analysis</i>	79
<i>(a) Energy dispersed X-ray analysis (EDX)</i>	79
<i>(b) X-ray fluorescence (XRF)</i>	80
<i>2.4.5 Optical analysis</i>	81
<i>(a) Determination of Band gap energy</i>	81
<i>(b) Photoluminescence</i>	84
<i>2.4.6 Electro-Optic characterization</i>	89
<i>(a) Luminescence-Voltage characterization</i>	89
<i>(b) Efficiency-Voltage Characterization</i>	92
<i>(c) Color and chromaticity coordinates</i>	92
<i>2.4.7 Electrical characterization</i>	97
<i>References</i>	102

## CHAPTER 3

### Synthesis and Characterization of oxide phosphors

#### Part A

#### Synthesis and characterization of $\text{Zn}_2\text{GeO}_4:\text{Mn}^{2+}$ phosphor

<i>3A.1. Introduction</i>	111
<i>3A.2. Experiment</i>	111
<i>3A.3. Results and Discussion</i>	112
<i>3A.3.1. X-ray diffraction studies</i>	113
<i>3A.3.2 Optical characterization</i>	117
<i>(a) Diffused reflectance spectra (DRS) analysis</i>	117
<i>(b) Photoluminescence studies</i>	119
<i>3A.3.3 Electron spin resonance (ESR) studies</i>	124
<i>Conclusion</i>	127

#### Part B

#### Synthesis and characterization of $\text{Mg}_2\text{GeO}_4:\text{Mn}^{2+}$ phosphor

<i>3B.1 Introduction</i>	131
<i>3B.2 Experiment</i>	132
<i>3B.3 Results and discussion</i>	132
<i>3B.3.1 X-ray diffraction studies</i>	132

<i>3B.3.2 Diffused reflectance spectra (DRS) analysis</i>	134
<i>3B.3.3 Photoluminescence studies</i>	136
<i>3B.3.4 Electron spin resonance studies</i>	139
<i>Conclusion</i>	141
<i>References</i>	141

## **CHAPTER 4**

### **Growth and Characterization of oxide phosphor thin films**

#### **Part A**

#### **Growth and characterization of RF magnetron sputtered $\text{ZnGa}_2\text{O}_4:\text{Mn}^{2+}$ thin films**

<i>4A.1 Introduction</i>	151
<i>4A.2 Experiment</i>	152
<i>4A.3 Results and Discussion</i>	153
<i>4A.3.1. X-ray diffraction studies</i>	153
<i>4A.3.2 Atomic force microscopy</i>	159
<i>4A.3.3 Optical Characterization</i>	160
<i>(a) Transmission spectra</i>	160
<i>(b) Photoluminescence Studies</i>	161
<i>4A.3.4 The CIE coordinates</i>	168

*Conclusion* 168

## **Part B**

### **Growth and characterization of RF magnetron sputtered $\text{Zn}_2\text{GeO}_4\text{:Mn}$ thin films**

*4B.1 Introduction* 173

*4B.2 Experiment* 174

*4B.3 Results and Discussion* 175

*4B.3.1. X-ray diffraction studies* 175

*4B.3.2 Band gap* 180

*4B.3.3 Scanning electron microscopy* 181

*4B.3.4 Photoluminescence studies* 183

*Conclusion* 185

## **Part C**

### **Growth and characterization of $\text{Y}_2\text{O}_3\text{:Eu}$ phosphor thin films**

*4C.1 Introduction* 189

*4C.2 Experiment* 191

*4C.3 Results and Discussion* 192

*4C.3.1. X-ray diffraction studies* 192

*4C.3.2 Scanning electron microscopy* 195

*4C.3.3 Photoluminescence studies* 197

4C.3.4 <i>The CIE coordinates</i>	202
<i>Conclusion</i>	203
<i>References</i>	203
<b>CHAPTER 5</b>	
<b>Fabrication of ACTFEL devices</b>	
5.1 <i>Introduction</i>	213
5.2 <i>Experiment</i>	214
5.3 <i>Results and discussion</i>	215
5.3.1. <i>Electroluminescence studies</i>	215
5.3.2 <i>Luminance -Voltage characteristics</i>	222
5.3.3 <i>The CIE coordinates</i>	223
5.3.4 <i>Charge-Voltage characteristics</i>	224
5.4 <i>Zn<sub>2</sub>GeO<sub>4</sub>:Mn and Y<sub>2</sub>O<sub>3</sub>:Eu based devices</i>	225
<i>Conclusion</i>	228
<i>References</i>	228
<b>CHAPTER 6</b>	
<b>Summary and scope for future work</b>	
6.1 <i>Summary</i>	231
6.2 <i>Scope for future work</i>	234

---

## Preface

---

For centuries, humans have been using displays in various forms, for satisfying communication needs. In the present world, electronic displays have a striking impact on our day to day life. For centuries, CRTs have been used in the display industry. Flat panel displays have been emerged as a new technology that could overcome certain disadvantages of cathode ray tubes (CRTs), especially the matter of portability. Presently in our laptops and mobiles we use liquid crystal displays (LCDs) that are portable and light weight. In the FPD technologies, electroluminescent (EL) displays have own place due to its inherent advantages like wide angle view, ruggedness and has a solid state environment. Sulphide phosphors have been widely used to fabricate ACTFEL devices due to relatively lesser crystallization temperature and better charge transport capabilities. But due to its lesser life time and out-gassing of harmful gases, the researchers switch over to oxide phosphors which overcome these defects of sulphides. But rather due to higher crystallization temperature and low charge transport capability, oxides did not get in to main stream of the electroluminescent display industry. As mentioned above, due to higher crystallization temperature, the devices based on oxide phosphors were fabricated on thick dielectric substrates, which act both as substrate and dielectric. This has a unique advantage that we can use high temperature post-deposition annealing ( $> 1000^{\circ}\text{C}$ ). But it prevents the use of conventional substrate-glass for device fabrication. So it is indeed a requisite to deposit the oxide phosphor thin films on glass substrates, at lower substrate/post annealing

temperatures. The thesis is focused on synthesis of oxide phosphors and growing thin films from them at lower temperatures with out any post-deposition treatments for possible applications in TFEL devices using glass substrates.

The thesis is organized in six chapters. Chapter 1 is a general introduction about ACTFEL devices and oxide phosphors that are used in lighting industry. A literature review on  $\text{ZnGa}_2\text{O}_4\text{:Mn}$ ,  $\text{Zn}_2\text{GeO}_4\text{:Mn}$  and  $\text{Y}_2\text{O}_3\text{:Eu}$  phosphors are also given in this chapter.

Chapter 2 deals with experimental techniques for preparing bulk oxide phosphor and growing thin films and analytical tools used for characterizing the developed oxide phosphors.

The preparation and characterization of bulk oxide phosphors like  $\text{Zn}_2\text{GeO}_4\text{:Mn}$  and  $\text{Mg}_2\text{GeO}_4\text{:Mn}$  phosphors is the main focus of chapter 3. The chapter is divided in to two parts Part A and Part B. Part A deals with the effect of Mg co-doping in  $\text{Zn}_2\text{GeO}_4\text{:Mn}$  and Part B deals with the effect of Zn co-doping in  $\text{Mg}_2\text{GeO}_4\text{:Mn}$  on structural and luminescent properties and both systems has been characterized using .

Chapter 4 deals with the growth of oxide phosphor thin films. It is divided in to three parts. Part A deals with the growth of  $\text{ZnGa}_2\text{O}_4\text{:Mn}$  thin films by rf magnetron sputtering. The influence of a dopant source on structural and luminescent characteristics has been studied. Two dopant sources namely  $(\text{CH}_3\text{COO})_2\text{Mn}$  and  $\text{MnO}$  are used to incorporate Mn in to host lattice. The as deposited films were characterized using XRD, Photoluminescence, AFM etc. Part B deals with the growth of growth of  $\text{Zn}_2\text{GeO}_4\text{:Mn}$  thin films using rf magnetron sputtering. Even though crystallization temperature of  $\text{Zn}_2\text{GeO}_4\text{:Mn}$  was found to be  $650^\circ\text{C}$ , in the literature there are no reports on growth of

crystalline  $Zn_2GeO_4:Mn$  on amorphous substrates via substrate heating using either sputtering or PLD. Reports suggest that only through post deposition annealing or using single crystalline substrates, crystalline films could be grown. Here crystalline  $Zn_2GeO_4:Mn$  was deposited on amorphous quartz substrate with and without ZnO buffer layer and the effect of this ZnO buffer layer on structural and luminescent characteristics are studied. Part C deals with growth of Eu doped  $Y_2O_3$  thin films using pulsed laser deposition. The effect of oxygen partial pressure and substrate temperature on structural and luminescent characteristics has been extensively studied.

Chapter 5 deals with the fabrication of green emitting ACTFEL devices using  $ZnGa_2O_4:Mn$  as active layer. The device was fabricated on conventional ITO/ATO coated glass substrates and with out any post deposition treatments. The effect of active layer thickness on luminescent properties has been studied. The EL emission spectra suggest the occupancy of Mn at different sites in the host lattice.

And finally chapter 6 gives the summary of the present work and recommendations for future work.

**Part of the thesis has been published in the internationally referred journals.**

**Publications related to the work presented in the thesis**

International journals

1. The effect of Mg incorporation on structural and optical properties of  $\text{Zn}_2\text{GeO}_4:\text{Mn}^{2+}$  phosphor.  
**G. Anoop**, K. Mini Krishna and M. K. Jayaraj, *J. Electrochem. Soc.*, **155**, J7 (2008)
2. Influence of dopant source on structural and optical properties of Mn doped  $\text{ZnGa}_2\text{O}_4$  thin films.  
**G. Anoop**, K. Mini Krishna and M. K. Jayaraj, *Appl. Phys. A*, **90**, 711 (2008)
3.  $\text{Mg}_{1.96-1.96x}\text{Zn}_{1.96x}\text{GeO}_4:\text{Mn}_{0.04}$  phosphors for electroluminescent display applications.  
**G. Anoop**, K. Mini Krishna and M. K. Jayaraj, *J. Alloys. Compd.* (in press) doi: 10.1016/j.jallcom.2008.01.043
4. Effect of ZnO buffer on structural and luminescent properties of  $\text{Zn}_2\text{GeO}_4:\text{Mn}^{2+}$  phosphors.  
**G. Anoop**, K. Mini Krishna, K. Rajeev Kumar and M. K. Jayaraj. (under revision in *J. Electrochem. Soc.*)

5. Structural and Luminescent characteristics of Eu doped  $Y_2O_3$  thin films grown on amorphous silica substrates.  
**G. Anoop** and M.K Jayaraj (to be communicated)
6.  $ZnGa_2O_4:Mn^{2+}$  Thin Film Electroluminescent devices fabricated on glass substrates.  
**G. Anoop**, K. Mini Krishna and M.K Jayaraj (to be communicated)

### **Conference Presentations**

1. Alternating Current Powder Electroluminescent device using  $ZnGa_2O_4:Mn$  phosphor.  
**G. Anoop**, K. Mini Krishna, R. Reshmi and M. K. Jayaraj (Photonics 2004).
2. Zinc Gallate Phosphor For Electroluminescent Device Applications.  
**G. Anoop**, R. Manoj, M. Nisha, R. Reshmi, K. Mini Krishna and M. K. Jayaraj (NCLA 2005).
3. Photoluminescent Studies in Co-sputtered  $ZnGa_2O_4:Mn$  Phosphor Thin Films.  
**G. Anoop**, K. Mini Krishna and M. K. Jayaraj (ASID 2006).

### **Other publication to which author has contributed**

1. Host-sensitized white luminescence in  $ZnGa_2O_4:Dy^{3+}$  phosphor.  
K. Mini Krishna, **G. Anoop** and M. K. Jayaraj, *J. Electrochem. Soc.*, **154**, J310 (2007)
2. The effect of substrate temperature on structural and luminescent characteristics of RF magnetron sputtered  $ZnGa_2O_4:Dy^{3+}$  thin films.

K. Mini Krishna, **G. Anoop** and M. K. Jayaraj, *J. Electrochem. Soc.* **154**, J379 (2007)

3. Luminescent bio-compatible ZnO quantum dots prepared using laser ablation in liquid media.

R.S.Ajimsha, **G. Anoop**, Arun Aravind and M.K Jayaraj, *Electrochem. Solid St. Lett.*, **11**, K14 (2008)

4. White ACTFEL devices on glass substrates using  $\text{ZnGa}_2\text{O}_4:\text{Dy}^{3+}$  active layer

K. Mini Krishna, **G. Anoop** and M. K. Jayaraj (to be communicated)

5. Red shift in the photoluminescence emission of SrS:Cu, Cl phosphor.

E. I. Anila, G. Anoop, **K. Mini Krishna**, I. P. Sanjay Kumar and M. K. Jayaraj (Photonics 2006).

## **CHAPTER 1**

---

# **An Introduction to Electroluminescence and Oxide Phosphors**

---

*This chapter gives an introduction about the device structure, mechanism of electroluminescence and materials used in alternating current thin film electroluminescent (ACTFEL) devices. A general review on oxide phosphors particularly  $ZnGa_2O_4$ ,  $Zn_2GeO_4$  and  $Y_2O_3$  is also given in this chapter.*

ac thin film EL (ACTFEL), ac powder EL (ACPEL), dc thin film EL and dc powder EL. DCEL has been widely used for small displays on glass in automobiles usually as yellow fixed messages and for backlighting purposes. AC electroluminescence has opened up a whole new world, however. Figure 1.1 outlines some comparative remarks on the four kinds of EL devices. ZnS:Mn based ACTFEL displays of laptop personal computers and word processors and ACPEL backlights for liquid crystal displays are today commercially available. Powder EL displays have virtually unlimited potential, i.e., uniform light emission, thin profile and low power consumption [1]. Flexible powder EL devices can be made on polyethylene terephthalate (PET) coated indium tin oxide (ITO) substrates [2, 3]. Powder EL lights have been used for architectural and decorative lighting and as LCD backlights in cellular phones, personal digital assistants (PDA) and palmtop computers. But they also possess multiplexing limitations and suffer from low luminance, high operating voltage, poor contrast and significant luminance degradation over fairly short time (~ 500 hours). With the development of thin-film process technology in the 1960's, the initial efforts to utilize the phenomenon of electroluminescence on powder EL devices helped in developing thin-film EL devices.

Thin film phosphors have several advantages in comparison to the powders, such as higher lateral resolution from smaller grains, better thermal stability, reduced out-gassing, and better adhesion to the solid surface [4]. However, the biggest drawback in the use of phosphor thin films is their low brightness and efficiencies in comparison to those of bulk powder materials which are primarily associated with factors such as internal reflection, the small

interaction volume between incident beam and solid and absorption of generated light by substrate materials.

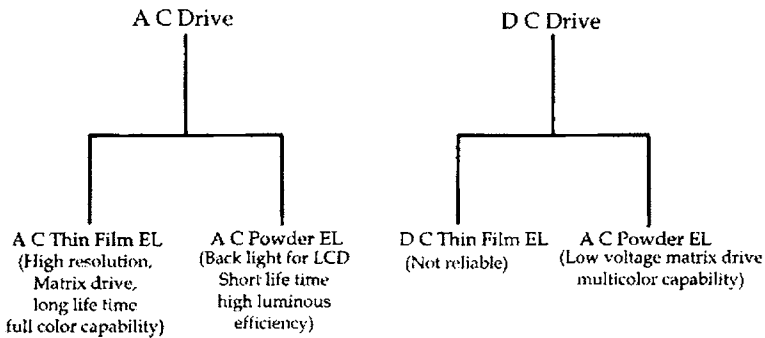


Figure 1.1 Comparison between the four types of EL displays

The ACTFEL displays have emerged as the most dependable emissive display technology owing to its unique features are explained below.

**Solid-state nature:** Fundamental to an EL device is its solid state construction which enables it to be fully integrated onto the substrate of the drive electronics. The solid-state nature makes them extremely rugged, a characteristic desirable for an FPD used in portable applications and harsh environments. The solid state construction makes it more resistant to shocks and vibrations. The luminous emission in a solid-state environment eliminates the risks involved in maintaining a vacuum or plasma environment, as in the case of VFDs, PDPs or FEDs.

**Ruggedness:** These solid-state devices are insensitive to shocks and wide temperature variation. They can, therefore, withstand aggressive environments - cold, heat, wind, dust, vibration, sunlight. So TFEL displays are very apt to be used in military equipments and spacecrafts.

**Wide viewing angle:** The emissive EL displays offer a viewing angle greater than  $160^\circ$  which is an inherent problem with the LCD displays. The absence of optical elements in the light path (other than the glass substrate) renders them this property and so very useful for medical and industrial applications.

**Wide operating temperature:** EL panels can be operated over a wide temperature range of  $-25^\circ\text{C}$  to  $60^\circ\text{C}$  (limited by the drive electronics) and therefore can serve in many critical military and industrial applications. They don't freeze or get slow or dim even at low temperatures.

**Long life:** The panel itself has no significant wear-out mechanism. Display panels have demonstrated device lifetimes of over 50,000 hours with less than 10% luminance change.

**High contrast:** This property gives EL displays what we call "at a glance" readability. This property makes them highly efficient in a very high ambient illumination environment such as in industrial instrumentation

**Better display qualities:** Fast response, high resolution and small pixel size are some of the best qualities of an EL display. They operate at video rates high enough to produce high information content FPDs with the image quality of the CRT.

## 1.2 Electroluminescence

Electroluminescence is a non-thermal generation of light resulting from the application of an electric field to a substance. The effect was first discovered by G. Destriau in 1936 in ZnS, when a large electric field was applied to it. There are two classes of EL devices. One is Light emitting diodes (LEDs) where light is generated by electron-hole pair recombination at a p-n junction which is also

known as injection luminescence while in high field EL, light is generated by impact excitation of a luminescent center (also called activator) by high energy electrons. Typical electric field through which electrons are accelerated is nearly  $10^6$  V/cm. So this type of luminescence is also referred as high field luminescence. Based on this high field luminance there are four types of EL devices namely ac thin film EL, ac powder EL, dc thin film EL and dc powder EL. They are categorized on the basis of drive voltage and the phosphor configuration. Since the thesis is focused on ac thin film EL devices, the structure and physics of ACTFEL devices are discussed in detail.

### **1.3 EL device Structure**

There are three general configurations for thin film EL device structures. One is conventional standard structure that comprises of Metal–insulator–semiconductor–insulator–metal (MISIM) structure [fig. 1.2(a)]. Second one is an inverted type structure [fig. 1.2(b)] and in third one usually one insulator normally a thick dielectric/ceramic [fig. 1.2(c)] is used. In the standard structure phosphor layer is sandwiched between two insulators (dielectric). Here bottom electrode which is transparent (usually ITO) while top electrode is opaque (usually Al/Au/In). In the inverted structure, the electrodes are simply inverted so that no light emission will take place in the opposite direction through the substrate unlike that in standard case. The advantage is that we can use non-transparent substrates like silicon which could withstand higher temperatures. In the standard structure, normally glass substrates are used and it will not withstand high processing temperatures.

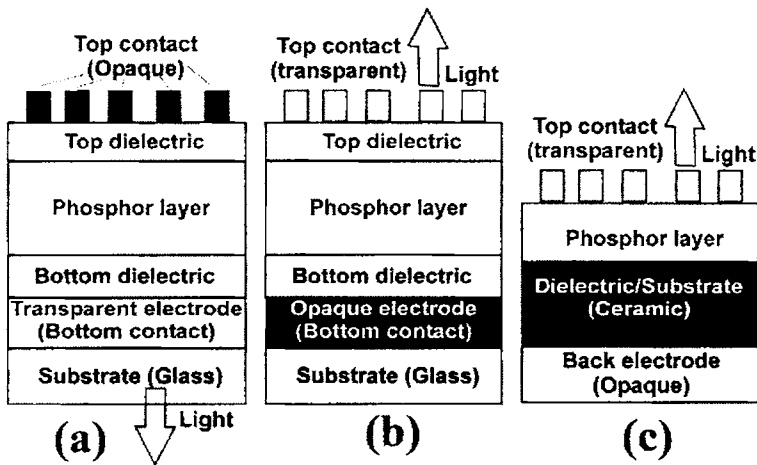


Figure 1.2 Three general configurations of TFEL devices

Some researchers employ the structure shown in figure 1.2(c) which consists of only single insulator that acts as substrate/insulator. The thickness of this ceramic insulator/substrate will be 0.2mm while that of other layers will be in nm/ $\mu\text{m}$  regime. The bottom opaque electrode will be deposited on the back side of the dielectric sheet and top electrode will be transparent and light emits through this electrode. Here we have an advantage that the structure is simple and higher post deposition annealing temperatures ( $1100^{\circ}\text{C}$ ) could be employed to improve the crystalline quality of the phosphor layer which is not possible in the case of glass substrates.

## 1.4 Ideal ACTFEL device

The basic ACTFEL device structure can be modeled as a simple circuit where the insulators are represented by perfect capacitors and the phosphor layer is represented by a capacitor below the threshold voltage and a pair of back-to-

back diodes above threshold voltage[5]. The equivalent-circuit model shown in figure 1.3 very well demonstrates the essential phenomenological physics of a thin-film EL device.

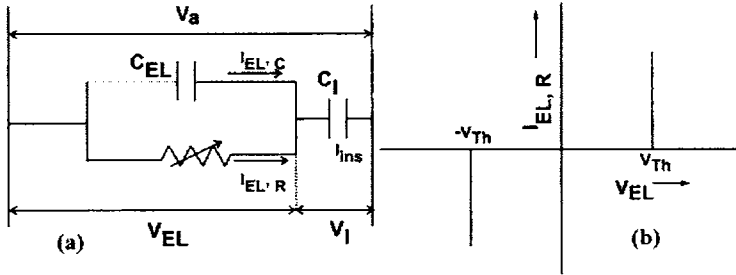


Figure 1.3 (a) Equivalent circuit of an ideal ACTFEL device and (b) Ideal I-V characteristics of the non-linear resistor of the phosphor layer

Below the threshold voltage, the model treats the TFEL device as a three series capacitor circuit where the voltage drop across each layer is proportional to the dielectric constant and the layer thickness. The first and second insulating layers are incorporated into one effective insulating layer with the effective capacitance per unit area,  $C_1$ , given by

$$C_1 = \frac{C_{I1}C_{I2}}{C_{I1} + C_{I2}} \quad (1.1)$$

where  $C_{I1}$  and  $C_{I2}$  are capacitances per unit area of the first and second insulating layers, respectively. The thin-film phosphor also behaves as a capacitor below the threshold voltage  $V_{th}$  with the capacitance per unit area  $C_{EL}$ . However, above the threshold voltage real (dissipative) current flows in the phosphor layer and gives rise to the light emission. Therefore, the phosphor layer is described as a capacitor in parallel with a non-linear resistor with the I-V

characteristic shown in figure 1.3(b). In an ideal case, this non-linear resistor can be simulated by back-to-back Zener diodes. The dependence of the device performance such as transferred charge density, power dissipation and luminance are expressed in terms of device parameters such as layer thickness, dielectric constant, dielectric breakdown strength, threshold field and luminous efficiency.

Voltage applied across the device,

$$V_a = V_I + V_{EL} \quad (1.2)$$

where  $V_I$  and  $V_{EL}$  represents the voltage across the insulating layers and the phosphor layer respectively. Now apply a pulse P1 whose magnitude is less than the threshold voltage. Below  $V_{th}$ ,  $V_a$  is capacitively divided. When  $V_a$  exceeds  $V_{th}$ , the resistive branch turns on and current flows (with accompanying light emission) to discharge the voltage across the phosphor capacitor back to the threshold level. After electron injection begins in an ideal device, all of the additional externally applied voltage is dropped across the dielectric layer(s) and the phosphor layer voltage remains constant. So the resistive branch must supply current to charge up the insulating layer capacitor by an equal voltage.

## 1.5 The EL Mechanism

The basic mechanism of electroluminescence as in the case of double insulator structure (standard) is discussed below. As we are discussing about AC-TFEL device, there are many waveforms like sine, triangular, trapezoidal, square that are generally used for exciting the devices. The usual convention is to refer the applied voltage to bottom electrode so that positive voltage is applied to Al (opaque) electrode. Since phosphor and insulator are wide band gap

semiconductors, we assume that there are no free charge carriers when the device is operated below threshold and it looks like a simple capacitor. The applied voltage is dropped in the dielectric and phosphor layer due to their capacitance. When the applied voltage reaches threshold voltage the device no longer behaves like a capacitor as the field in the phosphor increases and charge will start flowing through the device. Beyond the threshold voltage the device operation can be simply visualized as in the energy band diagram shown in the figure 1.4. Due to the disorder encountered on an atomic scale at the insulator-phosphor interface, large number of allowed electronic states is present with in the phosphor band gap at the interface. Ideally these states can be regarded as single discrete trap level with a large occupancy of electrons. When the phosphor field exceeds a particular threshold, these trapped electrons at the interface level begin to tunnel emit in to the phosphor conduction band as shown in the process (1) in the figure. Due to large electric field experienced by these electrons when they enter the phosphor conduction band, these electrons will drift across the phosphor layer (process 2). As electrons moves, in the diagram it is shown farther and farther higher in energy from the conduction band, showing that electron is gaining kinetic energy from the electric field. As it traverse the phosphor field, an electron may randomly collide with the atoms in the lattice, losing energy in the process, before again gaining the energy from the field. If a sufficiently energetic electron (energy for exciting the luminescent center) collides with a luminescent impurity, which is then excited in to higher energy state (process 3). The electron will continue traversing the phosphor layer due to the presence of electric field until it reaches the conduction band discontinuity between the phosphor and dielectric layers at the anodic side of the device. Here

it thermalizes, releasing heat energy to the lattice, to the bottom of conduction band and is re-trapped in a deep level at the interface states at phosphor-dielectric interface at anodic side (process 4). In the mean time the excited electron in the luminescent center will relax back to ground state (process 5) eventually emitting a photon, provided the transition is radiative. This photon is out-coupled from the device (process 6) through the transparent contact. When the applied voltage reaches maximum value in temporal scale, electron emission rapidly ceases. As electrons are emitted from the cathodic interface and drifted across the phosphor layer reaches the anodic interface, a net positive charge is left at the cathodic interface and a net negative charge adds to the anodic interface thereby introducing a polarization charge effect. This polarization field has some effects on the device operation. It can act as a negative feed back mechanism which makes it difficult to inject more electrons from the cathode. If a high density of electrons are available at the interface discrete trap level, they are injected fast enough that, even while the external voltage is increasing, the phosphor field remains at a steady state value or we can say that after electron injection begins, all the additional voltage applied to the device will drop across the dielectric layers keeping the phosphor layer voltage /field a constant. Other effect of polarization charge when the applied voltage reaches a zero value, this polarization field becomes prominent. This field causes the electrons that are trapped at the anodic side to re-emit in to the phosphor layer. This charge is mentioned as leakage charge. More over when the following negative pulse is applied to the device the external field is augmented by the polarization field which reduces the phosphor threshold at a lower external applied voltage than the threshold, termed as turn on voltage. Additionally, electrons begin to tunnel

at a lower external voltage and trap occupancy is larger and more charge is transferred across the device than during the previous one.

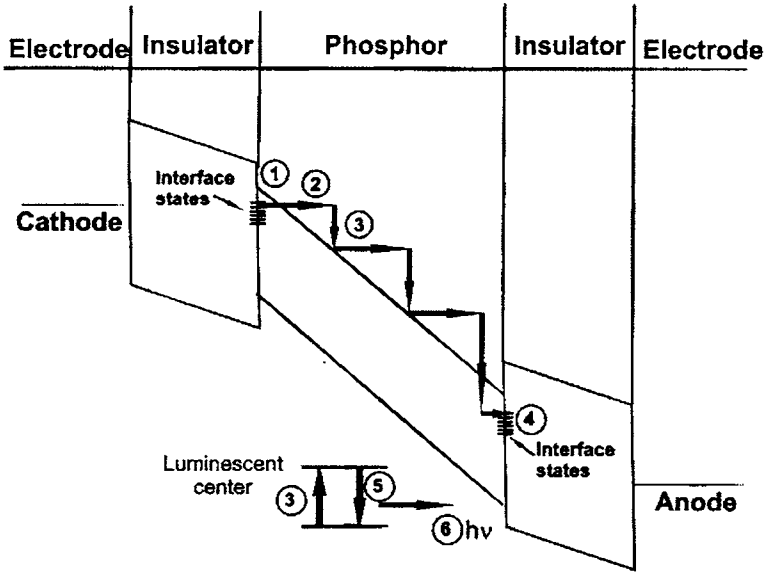


Figure 1.4 Energy band diagram of ACTFEL device

This establishes a larger polarization field so that turn on voltage is further reduced and the transferred charge amplification repeats. This process will continue till a steady state operating condition is established. In an ideal phosphor system, steady state operation may be established after only a few cycles.

## 1.6 Space charge in EL devices

One of the major deviations from the ideal operation of ACTFEL devices is the formation of space charge within the phosphor layer. "Space" in

the ACTFEL context refers to positive space charge and can arise in a number of ways. First and foremost reason is, with in the phosphor region, traps may be ionized via thermal or field emission or as a result of electron impingement. The removed electron is swept away by the electric field as the electrons experience a high field in the phosphor layer. Now the trap is positively charged and therefore acts to bend the energy band locally downwards. The ionized center may be intentionally added impurity which could act as a donor due to valency mismatch or a luminescent impurity whose excited states lie close to conduction band or a vacancy or a point defect. Another common source of space charge is band to band impact ionization of the lattice. Along with the band to band impact ionization, a hole is also left or created in the valence band while an electron is promoted to the conduction band as a delocalized charge carrier. This hole may drift towards the cathode a short distance before it is trapped resulting in a localized positive charge which will pull the band downward. The space charge induced curvature of band under device bias is shown in the figure 1.5. The dotted lines show the spatial dependence of the phosphor layer energy band locations in the absence of space charge. The linearity of band is indicative of the fact that a uniform electric field exists throughout the phosphor. The effect of space charge is bending of the band represented by curved lines. Compared to a phosphor layer with no space charge, electric field near cathode is greater for a phosphor layer with space charge, even though the externally applied potential is same in both cases, since the tunnel emission rate of electrons is a strong function of electric field. On the contrary electric field near anode will be reduced due to lesser field experienced due to the presence of space charge. This results in lesser density of energetic electrons in this region, which reduces

the probability of impact excitation. But it creates hot electron induced damage at the anodic phosphor-insulator interface. The lower electric field at the anodic region may lead to efficient carrier trapping, which is not appreciable at the high field cathodic region. Depending on the mechanism of space charge creation and light emission in a particular phosphor system, this will have noticeable effect in device operation.

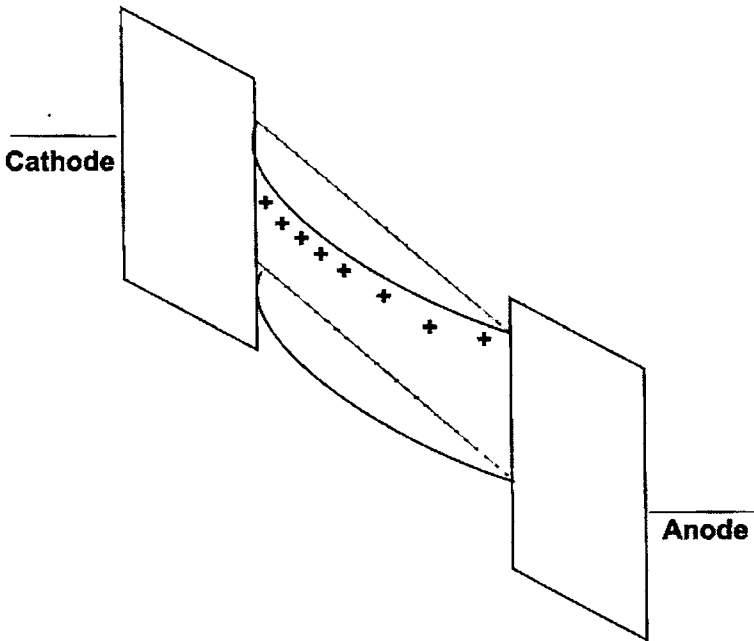


Figure 1.5 Space-charge induced band bending of phosphor layer in ACTFEL device

Space charge in ACTFEL devices can be classified in to either static or dynamic depending on the nature of spatio-temporal distribution. Normally the space charge created will be annihilated at some characteristic rate. The annihilation may be due to recombination of an electron with an ionized trap or the re-emission of trapped hole. If the annihilation proceeds at a slow rate

compared to ac drive wave form, the space charge forms a steady-state distribution and is denoted as static. Dynamic space is that portion of total space charge that is not in steady state but both created and annihilated with in one period of the drive waveform.

All well known ACTFEL phosphor systems have been found to exhibit space charge effects. The presence of space charge reduces the voltage necessary for drive operation which will in turn improve reliability and efficiency. On the other hand, if the space charge is dynamic, the energy expended creating and maintaining the space charge may reduce efficiency.

## **1.7 ACTFEL Materials**

The materials that are used in ACTFEL devices are

### **1.7.1 Substrate**

For a standard device, the primary requirements for the substrates are transparency, smooth surface, ability to withstand thermal treatments and the material should be inexpensive in a commercial view point. Therefore most commonly used substrate is glass. In the present study, the devices were fabricated on ITO/ATO coated ohara and NEG glass was supplied by Planar Inc., U.S.A.

### **1.7.2 Electrodes**

There are two types of electrodes used in standard structure, one is transparent through which light is viewed and other is opaque.

### **(a) Transparent electrode**

The transparent electrode should be sufficiently conducting, transparent in the entire visible region of the electromagnetic spectra and it should withstand higher thermal processing of subsequent layers. The most commonly used material is indium tin oxide (ITO). A thickness of 200 nm is generally used. Another material that is used as transparent electrode in ACTFEL device is ZnO:Al. In the present study ITO is used as transparent electrode.

### **(b) Opaque electrode**

The critical requirements for opaque electrode in a standard device structure are it should be highly conducting, good adhesion to the top insulator. Al is most commonly used electrode, and also in this study. The advantages of Al are, it is inexpensive, can be easily deposited using thermal evaporation, it has low melting point which enhances the possibility for self-healing breakdown fusing of metal surrounding the short. Typically the thickness of the electrode lies in 100-200 nm range.

## **1.7.3 Insulators**

The insulating layers of are important layers of the device structure. The insulator undergoes same thermal processing as the phosphor layer and therefore must have good thermal stability and chemical compatibility with the bottom electrode. The critical requirements of insulator layers are

1. High dielectric constant,  $\epsilon_0\epsilon_r$
2. High dielectric breakdown electric field,  $F_{BD}$
3. Small number of pinholes and defects
4. Good adhesion

### 5. Small loss factor, $\tan\delta$

In order to maximize the voltage drop across the device, the capacitance of the phosphor layer should be low as compared to insulators. The capacitance of the layers is calculated as

$$C = \frac{\epsilon_0 \epsilon_r A}{d}$$

Where  $\epsilon_0 \epsilon_r$  is the dielectric constant of the insulator material, A is the area of cross-section and d is the thickness of the insulator layer. Therefore to optimize/maximize the insulator capacitance the dielectric constant should be high and thickness layer should decrease. It is also logical to reduce the layer thickness instead of selecting high dielectric constant material. However there is a lower limit to thickness, as defects and pin holes will be high, if the thickness is low. Moreover the breakdown field strength is inversely proportional to the thickness of the layer ( $E = V/d$ ). Therefore thinner layer will have higher electric field. It is generally observed that materials with higher dielectric constant have a small breakdown strength and vice-versa. Further more, the high dielectric constant material tend to exhibit propagating breakdown. The dielectric materials used in this study are ATO, which is a stack of  $\text{Al}_2\text{O}_3$  and  $\text{TiO}_2$  and BTO ( $\text{BaTa}_2\text{O}_6$ ). The ATO layer was deposited by Atomic layer epitaxy method (ALE) by Planar Inc. In the present study, the top insulator BTO was deposited using rf magnetron sputtering.

### 1.7.4 Phosphor layer

The phosphor layer also called active layer typically comprises of a host and an activator/luminescent center. The host by its definition is the material/environment for activator or luminescent center which converts input

energy in to visible light. Generally sulphides are used as host materials in the ACTFEL devices. However oxides, due to its inherent advantages over sulphides, are also used as hosts for ACTFEL devices. The requirements for a phosphor host that are used in ACTFEL devices are

1. The host bandgap must be large enough not to absorb any emission from the luminescent center. For complete visible transmission, this requires a band gap of at least 3.1eV.
2. The host must be a good insulator below threshold. This is required to maintain a voltage drop and subsequent electric field across the phosphor layer, leading to the sub-threshold capacitive nature of the phosphor.
3. The host must have high breakdown strength to allow for efficient acceleration of electrons. This requires that the breakdown field of the phosphor must be at least 1MV/cm.
4. The host must have good crystallinity and a low phonon-coupling coefficient to minimize electron scattering.
5. Must be able to withstand the requisite post annealing treatments.

The emission of a phosphor is determined by activator/luminescent center. In addition, the host lattice influences the color emitted by an activator, since different hosts provide different crystal field environment for these activators. In the case of transition metals ( $\text{Mn}^{2+}$ ,  $\text{Cr}^{3+}$ ,  $\text{Ag}^+$ ,  $\text{Cu}^+$ ,  $\text{Ti}^{4+}$  etc) that are used as activators, the emitted light is highly influenced by the crystal field environment as outer d shell is involved in the emission process. But in the case of rare earth ions ( $\text{Eu}^{3+}$ ,  $\text{Dy}^{3+}$ ,  $\text{Tm}^{3+}$ ,  $\text{Tb}^{3+}$ ,  $\text{Ce}^{3+}$ ) that are used as activators, the emitted light is not much influenced by the crystal field environment, because

inner f shell is involved in the light emission process. The requirements of a luminescent material for suitable application in TFEL devices are

1. should be properly incorporated into host material and emit visible light
2. should have a large cross section for impact excitation
3. Stable in the high electric field ( $>10^6$  V/cm).

In the present work oxide phosphor hosts like  $\text{ZnGa}_2\text{O}_4$ ,  $\text{Zn}_2\text{GeO}_4$ ,  $\text{Mg}_2\text{GeO}_4$  and  $\text{Y}_2\text{O}_3$  are studied and activators used are  $\text{Mn}^{2+}$  and  $\text{Eu}^{3+}$ .

## 1.8 Oxide Phosphors

In the early 1990s oxide phosphors were introduced as a substitute to commercially available and well established phosphor class namely sulphides. Due to their inherent disadvantages like lack of primary color emission, instability in vacuum, inferior chemical, mechanical and thermal stability, corrosive gas emission under electron bombardment, it became a necessity to find a substitute that could satisfy the requirements of the display industry. So researchers around the world started working on another class of phosphors namely-oxide phosphors. Several binaries, ternaries and complex oxide phosphors were proposed and still continue proposing.  $\text{ZnO}$ , is such a binary oxide is also used a phosphor by doping with Mn.

First report of high luminance oxide phosphor TFEL device using  $\text{Zn}_2\text{SiO}_4:\text{Mn}$ , a ternary compound host material came in the early 1990s [6]. After that high luminance red and green emissions were realized using Mn/Eu doped oxide hosts [7, 8]. The table shows emission colour of certain oxide phosphors.

Table 1.1 Emission colour of certain oxide phosphors

Phosphor	Color	Reference
$\text{Ba}_3(\text{PO}_4)_2:\text{Eu}$	Blue-Violet	9
$\text{Ba}_3(\text{PO}_4)_2:\text{Ti}$	Blue-Violet	9
$\text{ZnGa}_2\text{O}_4$	Blue	10
$\text{ZnGa}_2\text{O}_4:\text{Ce}^{3+}$	Blue	11
$\text{Y}_2\text{SiO}_5:\text{Ce}^{3+}$	Blue	12
$\text{Y}_3\text{Al}_5\text{O}_{12}:\text{Tm}^{3+}$	Blue	12
$\text{LaAlGe}_2\text{O}_7:\text{Tm}$	Blue	13
$\text{BaMgAl}_{10}\text{O}_{16}:\text{Eu}^{2+}$	Blue	12
$\text{TaZn}_3\text{O}_8$	Blue	14
$\text{Ga}_2\text{O}_3:\text{Mn}^{2+}$	Green	7
$\text{ZnGa}_2\text{O}_4:\text{Mn}^{2+}$	Green	11
$\text{ZnGa}_2\text{O}_4:\text{Tb}^{3+}$	Green	15
$\text{Zn}_2\text{GeO}_4:\text{Mn}^{2+}$	Green	16
$\text{Zn}_2\text{SiO}_4:\text{Mn}$	Green	17
$\text{Y}_3\text{Al}_5\text{O}_{12}:\text{Tb}^{3+}$	Green	12
$\text{Zn}_3\text{Ta}_2\text{O}_8:\text{Tb}^{3+}$	Green	18
$\text{Ca}_3\text{Sc}_2\text{Si}_3\text{O}_{12}:\text{Ce}^{3+}$	Green	19
$\text{CaSc}_2\text{O}_4:\text{Ce}^{3+}$	Green	20
$\text{TaZn}_3\text{O}_8:\text{Mn}$	Green	14
$\text{ZnAl}_2\text{O}_4:\text{Mn}$	Green	21
$\text{Y}_3\text{Al}_5\text{O}_{12}:\text{Eu}^{3+}$	Red	12

Table 1.1 continued...

$\text{ZnGa}_2\text{O}_4:\text{Cr}^{3+}$	Red	22
$\text{Ga}_2\text{O}_3:\text{Eu}^{3+}$	Red	23
$\text{Y}_2\text{O}_3:\text{Eu}^{3+}$	Red	24
$\text{Zn}_3\text{Ta}_2\text{O}_8:\text{Eu}^{3+}$	Red	18
$\text{LiInO}_2:\text{Eu}^{3+}$	Red	25
$\text{CaIn}_2\text{O}_4:\text{Eu}^{3+}$	White	26
$\text{KSrPO}_4:\text{Eu}^{2+}$	White	27
$\text{SrIn}_2\text{O}_4:\text{Dy}^{3+}, \text{Pr}^{3+}, \text{Tb}^{3+}$	White	28
$\text{Sr}_2\text{SiO}_4:\text{Eu}^{2+}, \text{Ce}^{3+}$	White	29
$\text{CaMgSi}_2\text{O}_6:\text{Eu}^{2+}, \text{Mn}^{2+}$	White	30, 31
$\text{CaAl}_2\text{Si}_2\text{O}_8:\text{Eu}^{2+}, \text{Mn}^{2+}$	White	32
$\text{SrZn}_2(\text{PO}_4)_2:\text{Eu}^{2+}, \text{Mn}^{2+}$	White	33
$\text{La}_{0.827}\text{Al}_{11.9}\text{O}_{19.09}:\text{Eu}^{2+}, \text{Mn}^{2+}$	White	34
$\text{Ca}_2\text{P}_2\text{O}_7:\text{Eu}^{2+}, \text{Mn}^{2+}$	White	35

## 1.9 Zinc gallium oxide- $\text{ZnGa}_2\text{O}_4$

Zinc gallate or Zinc gallium oxide is a ternary oxide phosphor which has been proved as an efficient host material for electroluminescent devices.

$\text{ZnGa}_2\text{O}_4$  is a low voltage cathodoluminescent (LVCL) phosphor. Itoh *et al.* has utilized this property in realizing vacuum fluorescent displays [10].  $\text{ZnGa}_2\text{O}_4$  does not cause damage to filaments in VFDs, unlike conventional sulfide phosphors. Blue luminescence at 470 nm and a chromaticity at  $X = 0.170$  and  $Y = 0.130$  was observed from the bulk phosphors prepared at various firing

temperatures. A luminous efficiency of 0.7 lm/W has been obtained, when the VFD with this phosphor is operated at 30 V dc and the device shows excellent stability [10]. Since  $\text{ZnGa}_2\text{O}_4$  has a wide band gap, it has been investigated as a UV-transparent electronic conductor [36].

Doped and undoped  $\text{ZnGa}_2\text{O}_4$  bulk phosphor has been prepared using various preparation techniques like solid state reaction [36-48], oxalate gel synthesis [49], sol-gel route [50], aerosol pyrolysis [51], citrate gel process [52], microencapsulation method [53], multi-stage precipitation method [55]. Omata *et al.* has investigated  $\text{ZnGa}_2\text{O}_4$  phosphor for possible application in uv-transparent conducting oxide [36]. In solid state reaction using the mixture of  $\text{ZnO}$  and  $\text{Ga}_2\text{O}_3$  in 1:1 molar ratio, single phase of  $\text{ZnGa}_2\text{O}_4$  has been formed when the mixture was fired at and above  $1000^\circ\text{C}$  for 24 hrs [39]. From the XPS analysis, the separation between the  $\text{Zn } 2p_{3/2}$  and  $\text{Ga } 2p_{3/2}$  peaks, can be used as a sensitive tool to distinguish between a complete formation of  $\text{ZnGa}_2\text{O}_4$  compound and a mixture of  $\text{ZnO}$  and  $\text{Ga}_2\text{O}_3$  powders [39].

### 1.9.1 Crystal Structure

$\text{ZnGa}_2\text{O}_4$  with formulae  $\text{AB}_2\text{O}_4$  has a cubic-spinel structure which can be viewed as a combination of rock salt and zinc blende structures. It has a close packed cubic arrangement of anions with one half of the octahedral holes and one eighth of tetrahedral holes filled with cations (fig.1.6). If  $\text{A}^{2+}$  are in tetrahedral sites and  $\text{B}^{3+}$  are at octahedral sites, we call the spinel as normal spinel. If  $\text{A}^{2+}$  are at octahedral sites and half of the  $\text{B}^{3+}$  are at tetrahedral and the other half at octahedral sites, then it is called inverse spinel structure. The distribution of cations can be intermediate which is known as mixed spinel structure. The  $\text{ZnGa}_2\text{O}_4$  is found to be a normal spinel with all  $\text{Zn}^{2+}$  ions at

tetrahedral sites and  $\text{Ga}^{3+}$  at octahedral sites with lattice constant  $a = 8.37 \text{ \AA}$ . The oxygen ions are in the face centered cubic closed packing. For a sub cell of this structure, there are four atoms, four tetrahedral interstices and eight octahedral interstices. This makes a total of twelve interstices to be filled up with three cations, one divalent and other two trivalent.

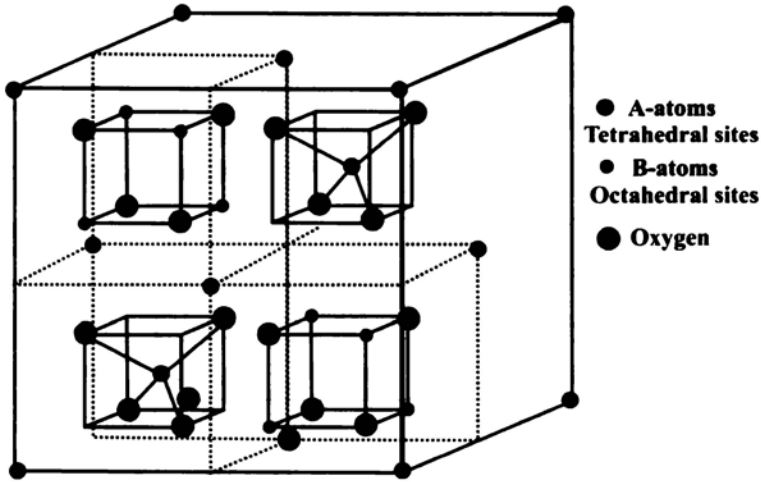


Figure 1.6 The spinel structure of  $\text{ZnGa}_2\text{O}_4$

In each elementary cell two octahedral sites are filled and one is tetrahedral. Eight of these elementary cells are arranged so as to form a unit cell containing 32 oxygen ions, 16 octahedral cations and 8 tetrahedral cations.

The optical band gap of  $\text{ZnGa}_2\text{O}_4$  is found to be 4.4 eV which is a direct band gap.

### 1.9.2 Photoluminescence

$\text{ZnGa}_2\text{O}_4$  exhibits strong blue luminescence due to transition via self activated center on excitation with ultraviolet light or low energy electrons.

ZnGa<sub>2</sub>O<sub>4</sub> doped with Mn or Cr exhibits green or red luminescence. In ZnGa<sub>2</sub>O<sub>4</sub>, Ga acts as sensitizer. The effect of excess Ga<sup>3+</sup> ions is proposed just like Cr<sup>3+</sup> ions in the spinel structure [41]. The wave functions of the S,P,D... terms are similar to those s,p,d,... orbitals, because the terms differ slightly from those of the corresponding orbitals, and so they may transform differently in a particular point group. For example, in the octahedral structure, p orbitals transform as T<sub>1g</sub>, the P term which is derived from the d configuration transforms as T<sub>1g</sub>. Because of the interactions, the orbitals of the transformed p term with the orbitals of the six oxygen ligands, result in shifts in the energy levels of the individual orbitals resulting in the splitting of the 3d energy levels occurs and degeneracy is lifted. The most commonly observed octahedral or tetrahedral environments lead to different arrangements. The effect of the strength of ligand field in an octahedral environment on the resultant energy levels, labelled by their spectroscopic terms <sup>4</sup>A<sub>2</sub>, <sup>4</sup>T<sub>1</sub>, <sup>4</sup>T<sub>2</sub> and <sup>2</sup>E are shown in the figure 1.7.

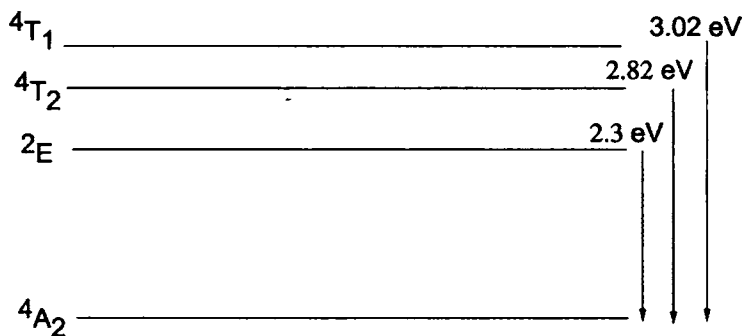


Figure 1.7 Ga<sup>3+</sup> level splitting in an octahedral environment

A broad fluorescence band peaking at 432 nm is observed when excited with UV light of 260 nm. This luminescence originates from self activated Ga at octahedral site. Jeong *et al.* [41] investigated compositional dependence of the luminescence of zinc gallate prepared by solid state reaction technique, firing at 1250°C for 4 hrs. They prepared phosphors with nominal formulae  $ZnGa_xO_{1+1.5x}$  with  $x$  (Ga/Zn ratio) varying from 1.98 to 3. They observed a broad emission band peaking at 432 nm, for the excitation band peak at 260 nm. The intensity of the band increases continuously as Ga/Zn ratio increases from 1.98 to 2.02. This increase in intensity was attributed to the increase in oxygen vacancy due to excess  $Ga_2O_3$ . When Ga/Zn ratio was above 2.03, the excitation and emission were very different from those of stoichiometric  $ZnGa_2O_4$ . A shoulder peak at 246 nm was developed with decrease in intensity of excitation peak at 260 nm. The emission wavelength shifted to 360 nm. This peak cannot be considered to be originated from  $\beta$ - $Ga_2O_3$  even though the excitation and emission spectra of  $\beta$ - $Ga_2O_3$  heat treated at same conditions showed similar behaviour. Most spinels show a solid solution with  $B_2O_3$  type oxides, hence solubility of  $Ga_2O_3$  in the  $ZnGa_2O_4$  lattice is expected. Therefore the absorption band peaking at 260 nm and emission at 432 nm corresponds to transition in octahedral Ga-O groups in the spinel lattice. The absorption and fluorescence at 246 nm and 360 nm can be related with self activated optical centers due to the tetrahedral Ga-O group. Randomness of the spinel structure having the formulae  $(A_{1-x}B_x)^{IV}(B_{2-x}A_x)^{VI}O_4$  is also reported and this randomness is not necessarily a constant. In some cases this randomness can be varied by appropriate heat treatment.

The randomness of the spinel structure can be determined by X-ray diffraction and neutron diffraction. If there is a sufficient difference between the

X-ray scattering powers of Zn and Ga, it might have been possible to determine the distribution of these atoms by the usual methods of X-ray crystallography. In  $\text{ZnGa}_2\text{O}_4$  the scattering powers of Zn and Ga, are almost the same. Another possibility is to distinguish from IR spectra. In the IR spectrum of zinc gallate, vibration peaks appear at  $420\text{ cm}^{-1}$  and  $570\text{ cm}^{-1}$ . However, to differentiate the peak of the tetrahedral Ga-O from that of the octahedral Ga-O was difficult. Even though it is not possible to identify the Ga site neither by XRD nor by IR spectroscopy,  $\text{Ga}^{3+}$  ions be not only on the octahedral sites but also on the tetrahedral sites when the zinc gallate is synthesized with  $\beta\text{-Ga}_2\text{O}_3$  under the gallate rich environment. Therefore, the excitation band at shorter wavelength (peaking at 246 nm) and the fluorescence band at 360 nm is considered to originate from the gallium at the tetrahedral sites when excess gallium is introduced in the spinel. Moreover color tuning has been observed via oxidation or reduction process of  $\text{ZnGa}_2\text{O}_4$  phosphor. The color oscillates between ultraviolet (360 nm) and blue (430 nm). The ultraviolet emission of reduced  $\text{ZnGa}_2\text{O}_4$  always accompanies 680 nm emission originating from single oxygen vacancies ( $V_{\text{O}}^*$ ). They observed an increase in the difference in binding energy between  $\text{Ga}^{3+}$  and  $\text{O}^{2+}$  in reduced  $\text{ZnGa}_2\text{O}_4$  indicates that the configuration of octahedral sites is distorted due to  $V_{\text{O}}^*$  generation and it becomes more ionic which shifts the emission band from 430 to 360 nm.

$\text{ZnGa}_2\text{O}_4$  exhibits green emission on doping  $\text{Mn}^{2+}$  ions. The excitation energy of zinc gallate is transferred in a non-radiative manner from the host lattice, Ga-O group acts as sensitizer to  $\text{Mn}^{2+}$  center. In order to get green emission of good color and purity,  $\text{ZnGa}_2\text{O}_4:\text{Mn}$  phosphor has to be annealed in a reducing atmosphere to convert  $\text{Mn}^{4+}/\text{Mn}^{3+}$  to  $\text{Mn}^{2+}$ . Interestingly during this

annealing process in a reducing atmosphere, not only reduction of Mn ions will take place but also redistribution of Ga ions in the spinel structure will occur. As the spectral overlap of and is large, the transfer will occur in a non-radiative way from  $\text{Mn}^{2+}$  to  $\text{Mn}^{3+}$  reducing the luminance output. Yu and Lin reported a weak red emission at 666 nm when excited at 325 nm [37]. The green emission at 508nm is observed which can be attributed to  ${}^4\text{T}_1\text{-}{}^6\text{A}_1$  transitions of tetrahedrally coordinated Mn ions. The PLE of the phosphor when monitored at 508 nm was observed at 245 nm and 290 nm. The band at 245 nm is the direct excitation of the host, in particular the Ga-O group and that at 290 nm corresponds to direct excitation or the charge transfer band of the  $\text{Mn}^{2+}$  ions. Shea *et al.* [55] observed the green emission at 506nm while Tran *et al.* [56] measured this luminance at 503 nm. More over Trans *et al.* reported that the emission at lower temperature can be attributed to three emission centers 1) Mn at tetrahedral Zn site, 2) at  $\text{Zn}^{2+}$  site with distorted tetrahedron and 3) Mn at octahedral  $\text{Ga}^{3+}$  site [56]. But Poort *et al.* reported emission from only one centre which is  $\text{Mn}^{2+}$  at  $\text{Zn}^{2+}$  site [57]. They calculated the effective distance of energy transport as 40Å at 4.2 K. Uheda *et al.* suggested that the long term phosphorescence of  $\text{ZnGa}_2\text{O}_4\text{:Mn}$  is due to the formation of several trap states, mainly due to Zn vacancies [38]. These trap states lie in the energy range 0.48-0.71 eV above the valence band of the host. Several authors had reported enhancement in luminescent intensity via co-doping the phosphor with other impurities. For example 5% enhancement in luminescent intensity has been observed for Ge and Li codoped  $\text{ZnGa}_2\text{O}_4\text{:Mn}$  phosphor. Cd codoping has resulted in red-shift of emission wavelength in  $\text{ZnGa}_2\text{O}_4\text{:Mn}$  bulk phosphor due to effective change in crystal field. Choi *et al.* observed that the solid solubility limit of Cd in bulk  $\text{ZnGa}_2\text{O}_4$  phosphor is 0.6

and a red shift of emission wavelength from 350 to 520 is observed [40]. The PL and CL emission intensity were found to increase with  $\text{In}_2\text{O}_3$  doping also [41].

Thin films of doped and undoped  $\text{ZnGa}_2\text{O}_4$  has been deposited on various amorphous and single crystalline substrates using physical vapour deposition techniques like pulsed laser deposition [58-70], rf magnetron sputtering [71-82], solvent evaporation [83], sol-gel process [84] and electrophoretic deposition [86]. Thin films were deposited using pulsed laser deposition on various substrates including single crystalline substrates like  $\text{Al}_2\text{O}_3$ , MgO and Si. The effect of Se doping on luminescent characteristics of  $\text{ZnGa}_2\text{O}_4:\text{Mn}$  phosphor thin films deposited on MgO substrates were studied by Jeong *et al.* and they found that MgO is one of the promising substrates to grow highly crystalline thin films of  $\text{ZnGa}_2\text{O}_4$  [62]. The brightness of the phosphor was found to increase by a factor of 3.1 compared to as deposited phosphor without Se [62]. Bae *et al.* [63] reported that  $\text{Al}_2\text{O}_3$  (sapphire) is also one of the most promising substrate to grow high quality thin films compared to Si. An increase in  $\beta\text{-Ga}_2\text{O}_3$  phase is observed as the annealing temperature was  $600^\circ\text{C}$  and above [63]. Epitaxial thin films of  $\text{ZnGa}_2\text{O}_4:\text{Mn}$  has also been deposited on MgO substrates using pulsed laser ablation and the effect of Zn/Ga ratio on crystalline luminescence were studied and a Zn/Ga ratio of 0.4 resulted in bluish-white light [64]. PLD has been used for growing high crystalline quality epitaxial thin films, rf magnetron sputtering has been used by several authors to deposit polycrystalline thin films of doped and undoped  $\text{ZnGa}_2\text{O}_4$ . Hsieh *et al.* has observed low voltage cathodoluminescence from rf magnetron sputtered  $\text{ZnGa}_2\text{O}_4$  thin film and the effect of substrate temperature and annealing temperature were studied [70]. Chung *et al.* has studied the effect of annealing of

sputtered  $\text{ZnGa}_2\text{O}_4$  grown on various substrates like  $\text{ZnO:Al/glass}$ ,  $\text{ZnO:Ga/glass}$ ,  $\text{ZnO/ITO/glass}$  and  $\text{ITO/glass}$ . The surface morphology and luminescent properties of thin films depend on the crystallinity of the substrates. But the annealing conditions didn't affect the surface morphology while luminescent characteristics and Zn/Ga ratio were susceptible to annealing conditions [71]. The sputtered  $\text{ZnGa}_2\text{O}_4$  on Si substrate resulted in lower grain size film and higher PL intensity than grown on  $\text{ITO/glass}$  substrate [73]. Better crystalline films were obtained when  $\text{ZnGa}_2\text{O}_4$  was deposited over  $\text{In}_2\text{O}_3$  buffer layer and a white luminescence is observed from the films [75]. The microstructural characteristics of thin film  $\text{ZnGa}_2\text{O}_4$  :Mn phosphors grown by rf planar magnetron sputter deposition has been investigated by Kim *et al.*. The energetic particle bombardment has been found to have dramatic effects on the cross-sectional microstructure, degree of porosity, surface morphology, and film density of the deposited thin films [76, 77]. The  $\text{ZnGa}_2\text{O}_4$  thin films deposited at  $600^\circ\text{C}$  were found to show better luminescence while post deposition annealing improves the PL and CL performance of the phosphor.

$\text{ZnGa}_2\text{O}_4$  has been demonstrated as an excellent host material for multicolor-emitting phosphor layers in ACTFEL devices. Minami *et al.* has fabricated Mn, Cr, Ce, doped  $\text{ZnGa}_2\text{O}_4$  ACTFEL devices using the single insulating layered structure [11]. The phosphor layers were sputter deposited onto 0.2 mm thick ceramic sheets of  $\text{BaTiO}_3$ .  $\text{ZnO:Al/ITO}$  and  $\text{Al/Ag}$  were used as top and bottom electrodes respectively. The as-deposited devices were post-annealed at  $1020^\circ\text{C}$  for 5 hrs in argon ambient [11, 85, 86] or subjected to in-situ RTA (rapid thermal annealing) [87] to improve their performance. These devices gave a green EL emission with luminance over  $600 \text{ cd/m}^2$  and an efficiency

approaching 1 lm/W when driven at 1 KHz. Devices were also fabricated using low-pressure chemical vapor deposition [88] and dip-coating [89] techniques for depositing the light emitting layers. Flynn *et al.* [90] has reported TFEL studies of  $\text{ZnGa}_2\text{O}_4:\text{Mn}$  with an effort to investigate the EL characteristics of the phosphor when post-annealed at lower temperatures. ACPEL devices have also been fabricated by several groups using Mn (Cr) activated  $\text{ZnGa}_2\text{O}_4$  as the active layer with luminescent efficiency approaching 15 lm/W [91, 92].

### 1.10 Zinc Germanate- $\text{Zn}_2\text{GeO}_4$

$\text{Zn}_2\text{GeO}_4$  is also a ternary oxide phosphor, whose structure is similar to  $\text{Zn}_2\text{SiO}_4$ , where Si is replaced by Ge. The most prominent advantage of  $\text{Zn}_2\text{GeO}_4$  over  $\text{Zn}_2\text{SiO}_4$  is its low crystallization temperature. The band gap of  $\text{Zn}_2\text{GeO}_4$  is 4.57 eV. However in the literature, reports on  $\text{Zn}_2\text{GeO}_4$  phosphor are scarce.

The bulk phosphor prepared by solid state reaction is reported to be an intrinsically defect phosphor [93]. By doping  $\text{Zn}_2\text{GeO}_4$  using Mn, the phosphor emits intense green light at 535 nm.

Thin films of  $\text{Zn}_2\text{GeO}_4:\text{Mn}^{2+}$  have been deposited using rf magnetron sputtering [94-97] and PLD [98]. Improved luminescent characteristics have been obtained using post-deposition annealing in this phosphor material. However the thin film phosphor emits green light relatively low annealing temperature (650 – 700°C) via furnace annealing and at 125°C via hydrothermal annealing [99]. ACTFEL devices were also fabricated using sputtered  $\text{Zn}_2\text{GeO}_4:\text{Mn}$  as active layer [95-98]. Minami *et al.* has reported a highest luminance of 1536  $\text{Cd/m}^2$  from  $\text{Zn}_2\text{Si}_{0.5}\text{Ge}_{0.5}\text{O}_4$  at 60Hz drive frequency from the Thick dielectric electroluminescent (TDEL) devices fabricated on ceramic  $\text{BaTiO}_3$  substrates [97]. In all these cases the active layer was deposited using rf

magnetron sputtering. The effect of substrates and deposition parameters on luminescence of laser ablated  $Zn_2GeO_4:Mn$  was studied by Williams et. al [98]. Lewis et. al has fabricated a green ACTFEL device on glass substrates via rapid thermal annealing (RTA treatment on the deposited phosphor layer. The anneal temperature was  $860^\circ C$ . Baker *et al.* has fabricated EL device on Si substrates as a light source for integrated optics systems [99]. The active layer was sputtered  $Zn_2Si_{0.5}Ge_{0.5}O_4$ .

### 1.11 Yttrium oxide - $Y_2O_3$

Since the early 20th century, it has been known that crystals containing a small amount of rare earths emit characteristic luminescence lines, not bands, in the visible spectral region when the crystals are irradiated under an electron beam, ultraviolet light, and X-rays. The luminescence lines are assigned to the radiative transitions in the  $4f^n$  shell of rare-earth ions, which are well shielded electrically with the electrons in the 5d and 6s shells. Because of line luminescence, rather than broad band, scientists paid attention to the crystal field effect, e.g., Stark effect, on rare-earth luminescence. In that time, purification of rare earths was difficult. Rare earths are chemically very close to each other, so that ordinary techniques of analytical chemistry could not separate one from the other. In the late 1960s,  $YVO_4:Eu$  (laser material) was proposed as a phosphor for the red primary in color TV picture tube screens [100]. They claimed improvement of brightness and color fidelity of the screen, thus opening the door for industrial use of yttrium oxide ( $Y_2O_3$ ) and europium oxide ( $Eu_2O_3$ ), and subsequently other rare earths. The red primary phosphor shifted from  $YVO_4:Eu$  to  $Y_2O_3:Eu$ ,  $Gd_2O_3:Eu$ , and finally  $Y_2O_2S:Eu$ . Among the above mentioned

phosphors, being an oxide phosphor,  $Y_2O_3:Eu$  has created much interest among the researchers around the world.

### 1.11.1 Crystal structure

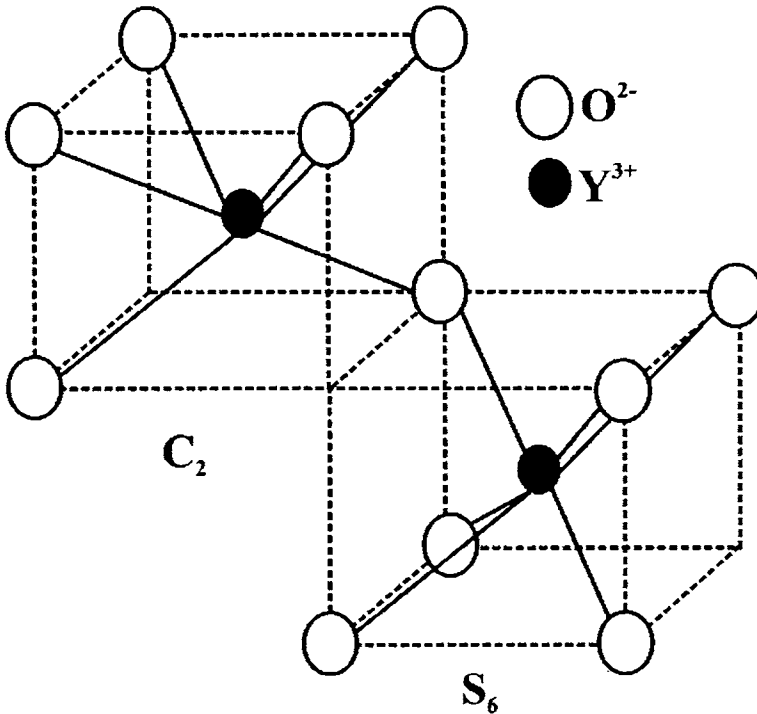


Figure 1.8 Two different types of crystal structures in  $Y_2O_3$  unit cell;  $C_2$  (vacancies along face diagonal) and  $S_6$  (vacancies along body diagonal)

Yttrium oxide has a cubic C-type or bixbyite ( $Mn_2O_3$ ) structure in which eight incomplete fluorite formula units exist with 80 atoms (yttrium:32 and oxygen:48) and a lattice constant  $a = 10.60 \text{ \AA}$  in the unit cell (figure 1.8). While in an ideal fluorite structure ( $CaF_2$ ) each cation is surrounded by eight anions located at the eight cube corners, the structure of  $Y_2O_3:Eu$  is modified

from the ideal fluorite structure by removing a quarter of oxygen atoms to maintain the charge neutrality and then rearranging the remaining six oxygen atoms from the cube corners. Therefore, each yttrium atom is surrounded by only six oxygen neighbors forming two different types of distorted octahedral structure ( $S_6$  and  $C_2$  sites, respectively (Fig. 1.8)) in the unit cell. Eight yttrium atoms occupy the  $S_6$  symmetry and 24 atoms are in the  $C_2$  symmetry [101].

### 1.11.2 Photoluminescence

In  $Y_2O_3:Eu^{3+}$ , the mechanisms that are governing the absorption and subsequent red emission are 1) direct excitation of the  $Eu^{3+}$  ion, 2) excitation via a charge-transfer state between the Eu ion and neighboring O ions or 3) excitation via the  $Y_2O_3$  host lattice [102]. The  $Y_2O_3:Eu$  PL emission consists of large number of lines ranging from 580 – 700 nm and in general these lines can be assigned to  $^5D_0 - ^7F_J$ ,  $J=0,1,2,3$  transitions OF  $Eu^{3+}$  ions. Each of these transitions is partially resolved in to various  $m_J$  transitions. These emission lines corresponds to inner f-f transitions and are electric dipole forbidden. From the emission spectrum, one can speak about local crystal environment of  $Eu^{3+}$  ion, especially analyzing the relative intensity ratio of  $^5D_0 - ^7F_1$  and  $^5D_0 - ^7F_2$  emission lines. The intensities of these transitions highly depend on local crystal environment in different ways [104]. The  $^5D_0 - ^7F_1$  transition is electric dipole forbidden and intensity of this line can be attributed to magnetic dipole operator and almost insensitive to local environment. But  $^5D_0 - ^7F_2$  transition, by mixing with higher allowed transition, is electric dipole allowed and intensity of which being hypersensitive to local environment (ie, the local electric field and local symmetry) [103].

$\text{Eu}^{3+}$  ions are supposed to replace  $\text{Y}^{3+}$  ions in the host lattice, thereby creating a charge transfer state (CTS) with neighboring oxygen atoms. These CT states absorb light from the incoming radiation, from which resonant transfer takes place to  $\text{Eu}^{3+}$  ions resulting in corresponding red PL emission. The emission spectrum consists of several lines which gives information about  $\text{Eu}^{3+}$  site symmetry in the lattice. In  $\text{Y}_2\text{O}_3$ , each yttrium atoms are surrounded by six oxygen atoms (instead of eight) making it intrinsically a defect phosphor. These defects can be along body diagonal ( $\text{C}_2$  symmetry), or along face diagonal of a cube ( $\text{S}_6$  symmetry) [104]. Only  $1/3^{\text{rd}}$  of the Y atoms occupy  $\text{S}_6$  symmetry while remaining  $2/3^{\text{rd}}$  of atoms occupies  $\text{C}_2$  symmetry [104]. The optical transitions in  $\text{Eu}^{3+}$  states are more likely to occur in the  $\text{C}_2$  site rather than in  $\text{S}_6$  site due to its more stable inversion symmetry of the lattice [104]. Therefore only certain magnetic dipole transitions are allowed in the  $\text{S}_6$  sites, while the electric dipole transitions are preferred in  $\text{C}_2$  sites. More over  $\text{S}_6$  site are less in number which will reduce the intensity of PL emission of magnetic dipole transitions. In the observed emission spectra, the lines at 538-585 nm ( ${}^5\text{D}_1 - {}^7\text{F}_1$ ) corresponds to magnetic dipole transitions while that at 590-715 nm ( ${}^5\text{D}_0 - {}^7\text{F}_j$ ,  $j = 0$  to 4) corresponds to electric dipole transitions which include peak emission maximum at 615 nm. In the observed spectra the relative intensity of magnetic dipole transitions are less compared to that of electric dipole transitions. Here, from the PL spectra it is concluded that  $\text{Eu}^{3+}$  ions are incorporated in to the host lattice and most of the ions predominantly replace Yttrium ions with  $\text{C}_2$  symmetry.

The bulk form of RE doped  $\text{Y}_2\text{O}_3$  has been synthesized using several techniques like flame fusion process [24], solid state reaction [105-108], citrate gel acid method [109], ceramic method [110], combustion method [111],

simultaneous addition method (simadd) [112] and self propagating high temperature synthesis [113]. Stimulated emission from single crystals of  $Y_2O_3:Eu$  have been reported [24]. Enhanced cathodoluminescence has been observed from  $Y_2O_3:Eu$  phosphor on co-doping with La, Li and Zn [107, 108, 110]. A white emission has been achieved from  $Y_2O_3$  doped with Eu and Sm, when excited with UV-LED showing it as an excellent phosphor for white LEDs [109]. The thin films of doped and undoped  $Y_2O_3$  has been deposited using spray pyrolysis [114, 115], Sol-gel technique [116-118], electron beam evaporation [119], rf magnetron sputtering [120-123], MOCVD [124] and pulsed laser ablation techniques [125-137]. PLD has been widely used to deposit high quality  $Y_2O_3$  thin films. ACTFEL device using  $Y_2O_3:Eu$  has been fabricated by Suyama *et al.* in conventional MISIM structure [138]. However no EL could be obtained from the devices. EL was observed when they used ZnS as accelerating layers. Multilayers of  $Y_2O_3:Eu$  and ZnS was deposited on Glass/ITO substrates. Due to low electron transport in  $Y_2O_3$ , EL could not be observed from the devices fabricated with out ZnS layer. So ZnS was used to accelerate the electrons as the ZnS have better electron transport property. But high luminance yellow emitting TDEL devices using  $Y_2O_3:Mn$  and combination of  $\{[Y_2O_3-GeO_2] Mn\}$  was fabricated by Minami *et al.* [139, 140].

## References

1. G. Wiedemann, *Ann. Phys. Chem.*, **34**, 446 (1888)
2. A. S. Marfunin, *Spectroscopy, Luminescence and Radiation Centers in Minerals*, translated by V. V. Schiffer, Springer-Verlag, Berlin Heidelberg, New York (1979)

3. D. R. Vij (Ed.), *Luminescence of Solids*, Plenum Press, New York (1998)
4. C. W. E. Van Eijk, *J. Lumin.*, **60**, 936 (1994)
5. D. H. Smith, *J. Lumin.*, **23**, 209 (1981)
6. T. Minami, T. Miyata, S. Takata and I. Fukuda, *Jpn. J. Appl. Phys.*, **30**, L117 (1991) (first report)
7. T. Minami, T. Shirai, T. Nakatani and T. Miyata, *Jpn. J. Appl. Phys.*, **39**, L524 (2000)
8. T. Minami et. al, In *Extend Abstr, 4<sup>th</sup> Int. Conf. Science and Technology of Display Phosphors*, Bend, OR (1998), p. 370
9. T. Miyata, Y. Mochizuki and T. Minami, *Thin Solid Films*, **496**, 174 (2006)
10. S. Itoh, H. Toki, Y. Sato, K. Morimoto, and T. Kishino, *J. Electrochem. Soc.*, **138**, 1509 (1991)
11. T. Minami, Y. Kuroi, T. Miyata, H. Yamada and S. Takata, *J. Lumin.*, **72**, 997 (1997)
12. J. McKittrick, L. E. Shea, C. F. Bacalski and E. J. Bose, *Displays*, **19**, 169 (1999)
13. Y. C. Li, Y. H. Chang, Y. F. Lin, Y. J. Lin and Y. S. Chang, *Appl. Phys. Lett.*, **89**, 081110 (2006)
14. P. D. Rack, M. D. Potter, S. Kurinec, W. Park, J. Penczek, B. K. Wagner and C. J. Summers, *J. Appl. Phys.*, **84**, 4466 (1998)
15. Z. Xu, Y. Li, Z. Liu and D. Wang, *J. Alloys. Comp.*, **391**, 202 (2005)
16. W. D. Partlow and D. W. Feldman, *J. Lumin.*, **6**, 11 (1973)
17. C. Barthou, J. Benoit, P. Benalloul and A. Morell, *J. Electrochem. Soc.*, **141**, 524 (1994)
18. H. Jiao, F. Liao, S. Tian and X. Jing, *J. Electrochem. Soc.*, **150**, H220 (2003)

19. Y. Shimomura, T. Kurushima, M. Shigeiwa and N. Kijima, *J. Electrochem. Soc.*, **155**, J45 (2008)
20. Y. Shimomura, T. Kurushima and N. Kijima, *J. Electrochem. Soc.*, **154**, J234 (2007)
21. Z. Lou and J. Hao, *Appl. Phys. A*, **80**, 151 (2005)
22. J. S. Kim, J. S. Kim, T. W. Kim, H. L. Park, Y.G Kim, S.K Chang and S. D. Han, *Solid State Commun.*, **131**, 493 (2004)
23. T. Minami, T. Miyata, T. Shirai and T. Nakatani, *Proc. Mater. Res. Soc. Symp.*, **621**, Q431 (2000)
24. N. C. Chang, *J. Appl. Phys.*, **34**, 3500 (1963)
25. S. A. Naidu and U. V. Varadaraju, *Electrochem. Solid St. Lett.*, **11**, J40 (2008)
26. X. Liu, C. Lin and J. Lin, *Appl. Phys. Lett.*, **90**, 081904 (2007)
27. Y. S. Tang, S. F. Hu, C. C Lin, N. C Bagkar and R. S Liu, *Appl. Phys. Lett.*, **90**, 151108 (2007)
28. X. Liu, C. Lin, Y. Luo and J. Lin, *J. Electrochem. Soc.*, **154**, J21 (2007)
29. N. Lakshmananarasimhan and U. V. Varadaraju, *J. Electrochem. Soc.*, **152**, H152 (2005)
30. S. H. Lee, J. H. Park, S. M. Son, J. S. Kim and H. L. Park, *Appl. Phys. Lett.*, **89**, 221916 (2006)
31. C. K. Chang and T. M. Chen, *Appl. Phys. Lett.*, **90**, 161901 (2007)
32. W. J. Yang, L. Luo, T. M. Chen and N. S. Wang, *Chem. Mater.*, **17**, 3883 (2005)
33. W. J. Yang and T. M. Chen, *Appl. Phys. Lett.*, **88**, 101903 (2006)

- 
34. Y. H. Won, H. S. Jang, W. B. Im, D. Y. Jeon and J. S. Lee, *Appl. Phys. Lett.*, **89**, 231909 (2006)
  35. Z. Hao, J. Zhang, X. Zhang, X. Sun, Y. Luo, S. Lu, X. J. Wang, *Appl. Phys. Lett.*, **90**, 261113 (2007)
  36. T. Omata, N. Ueda, K. Ueda, H. Kawazoe, *Appl. Phys. Lett.*, **64**, 1077 (1994)
  37. C. F. Yu and P. Lin, *J. App. Phys.*, **79**, 7191 (1996)
  38. K. Uheda, T. Maruyama, H. Takizawa and T. Endo, *J. Alloys Compd.*, **262**, 60 (1997)
  39. A. R. Phani, S. Santucci, S. D. Nardo, L. Lozzi, M. Passacantando and P. Picozzi, *J. Mat. Sci.*, **33**, 3969 (1998)
  40. S. K. Choi, H. S. Moon, S. I. Mho, T. W. Kim and H. L. Park, *Mat. Res. Bull.*, **33**, 693 (1998)
  41. I. K. Jeong, H. L. Park and S. I. Mho, *Solid State Commun.*, **105**, 179 (1998)
  42. K. H. Hsu and K. S. Chen, *Ceramics International*, **25**, 339 (1999)
  43. S. G. Kim, S. H. Lee, N. H. Park, H. L. Park, K. W. Min, S. I. Mho, T. W. Kim and Y. H. Hwang, *Solid State Commun.*, **110**, 515 (1999)
  44. S. H. Yang and M. Yokayama, *J. Vac. Sci. Tech. A*, **19**, 2463 (2001)
  45. J. S. Kim, H. I. Kang, W. N. Kim, J. I. Kim, J. C. Choi, and H. L. Park, G. C. Kim, T. W. Kim, Y. H. Hwang, S. I. Mho, M.C. Jung and M. Han, *Appl. Phys. Lett.*, **82**, 2029 (2003)
  46. V. R. Kumar, K.V. Narasimhalu, N. O. Gopal, H. K. Jung, R. P. S Chakaradhar and J. L. Rao, *J. Phys. Chem. Sol.*, **65**, 1367 (2004)
  47. Z. Xu, Y. Li, Z. Liu and D. Wang, *J. Alloys Compd.*, **391**, 202 (2005)
  48. Y. S. Jeong, J. S. Kim and H. L. Park, *Solid State Commun.*, **139**, 157 (2006)

49. J. H. Park, B. W. Park, N. S. Choi, Y. T. Jeong, J. S. Kim, and J. S. Yang, *Electrochem. Solid State Lett.*, **11**, J12 (2008)
50. R. Withnall, A. L. Lipman, G. R. Fern, A. Rose and J. Silver *J. Mater. Sci.*, **17**, 745 (2006)
51. J. S. Kim, J. S. Kim, T. W. Kim, S. M. Kim and H. L. Park, *Appl. Phys. Lett.*, **86**, 091912 (2005)
52. Y. K. Yoo, G. Y. Hong, S. H. Cho, and J. S. Yoo, *J. Electrochem. Soc.*, **148**, H109 (2001)
53. M. Yu, J. Lin, Y. H. Zhou, S. B. Wang, *Mater. Lett.*, **56**, 1007 (2002)
54. K. H. Hsu and K. S. Chen, *Ceramics International*, **26**, 469 (2000)
55. L. E. Shea, R. K. Datta, J. J. Brown, Jr, *J. Electrochem. Soc.*, **141**, 2198 (1994)
56. T. K. Tran, W. Park, J. W. Tomm, B. K. Wagner, S. M. Jacobsen, C. J. Summers, P. N. Yocom, S. K. McClelland, *J. Appl. Phys.*, **78** 5691(1995)
57. S. H. M. Poort., D. Cetin, A. Meijerink., and G. Blasse, *J. Electrochem. Soc.*, **144**, 2179 (1997)
58. Y. E. Lee, D. P. Norton and J. D. Budai, *Appl. Phys. Lett.*, **74**, 3155 (1999)
59. Y. E. Lee, D. P. Norton, C. Park, and C. M. Rouleau, *J. Appl. Phys.*, **89**, 1653 (2001)
60. S. S. Yi, I. W. Kim, J. S. Bae, B. K. Moon, S. B. Kim and J. H. Jeong, *Mater. Lett.*, **57**, 904 (2002)
61. Y. E. Lee, D. P. Norton, J. D. Budai, P. D. Rack, J. Peterson, and M. D. Potter, *J. Appl. Phys.*, **91**, 2974 (2002)
62. J. H. Jeong, B. K. Moon, H. J. Seo, J. S. Bae, S. S. Yi, W. Kim and H. L. Park, *Appl. Phys. Lett.*, **83**, 1346 (2003)

- 
63. J. S. Bae, B. K. Moon, B. C. Choi, J. H. Jeong, S. S. Yi, W. Kim and J. S Lee, *Thin Solid Films*, **424**, 291 (2003)
  64. S. S. Yi, J. S. Bae, B. K. Moon, J. H. Jeong, I. W. Kim and H. L. Park, *Appl. Phys. A*, **76**, 433 (2003)
  65. J. H. Jeong, J. S. Bae, B. C. Choi, S. S. Yi and P. H. Holloway, *J. Vac. Sci. Tech. A*, **22**, 1751 (2004)
  66. J. S. Bae, B. K. Moon, B. C. Choi, J. H. Jeong, S. S. Yi and J. H. Kim, *Thin Solid Films*, **479**, 238 (2005)
  67. K. Mini Krishna, M. Nisha, R. Reshmi, R. Manoj, A.S Asha and M.K Jayaraj, *Materials Forum*, **29**, 243 (2005)
  68. R. Reshmi, K. Mini Krishna, R. Manoj and M.K Jayaraj, *Surf. Coat. Tech.*, **198**, 345 (2005)
  69. I. Ahmad Md., M. Kottaisami, N. Rama, M. S. R. Rao and S. S. Bhattacharya, *Scripta Mater.*, **54**, 237 (2006)
  70. I. J. Hseih, M. S. Feng, K. T. Kuo, and P. Lin, *J. Electrochem. Soc.*, **141**, 1617 (1994)
  71. S. M. Chung and Y. J. Kim, *J. Vac. Sci. Tech. A*, **22**, 140 (2004)
  72. V. Bondar, *Mater. Sci. Engg. B*, **69**, 505 (2000)
  73. Y. J. Kim, Y.H. Jeong, K.D. Kim, S. G. Kang, K. G. Lee, J. I. Han and Y. K. Park, K. I. Cho, *J. Vac. Sci. Tech. B*, **16**, 1239 (1998)
  74. S. H. Yang, T. J. Hsueh, and S. J. Chang, *J. Electrochem.Soc.*, **152** H191 (2005)
  75. S. H. Yang, C.Y. Lu, and S. J. Chang, *J. Electrochem.Soc.*, **154**, J229 (2007)
  76. J. H. Kim and P. H. Holloway, *Appl. Phys. Lett.*, **84**, 2070 (2004)
  77. J. H. Kim and P.H. Holloway, *J. Vac. Sci. Tech. A*, **24**, 2164 (2006)

78. Y. J. Kim, S. M. Chung, Y.H. Jeong and Y.E. Lee, *J. Vac. Sci. Technol. A*, **19**, 1095 (2001)
79. S. M. Chung, S. H. Han and Y. J. Kim, *Mater. Lett.*, **59**, 786 (2005)
80. J. H. Park, S. H. Lee, J. S. Kim, H. W. Park, J. C. Choi, H. L. Park, G. C. Kim and J. H. Yoo, *J. Cryst. Growth*, **299**, 369 (2007)
81. H. W. Choi, B. J. Hong, S. K. Lee, K. H. Kim, Y. S. Park, *J. Lumin.*, **126**, 359 (2007)
82. Z. Yan, M. Koike and H. Takei, *J. Cryst. Growth*, **165**, 183 (1996)
83. T. Sei, Y. Nomura and T. Tsuchiya, *J. Non-Cry. Solids*, **218**, 135 (1997)
84. S. H. Yang, *J. Electrochem. Soc.*, **150**, H250 (2003)
85. T. Minami, T. Maeno, Y. Kuroi and S. Takata, *Jpn. J. Appl. Phys.*, **34**, L684 (1995)
86. T. Minami, S. Takata, Y. Kuroi and T. Maeno, *J. Soc. Inf. Disp.*, **4**, 53 (1996)
87. T. Minami, H. Toda and T. Miyata, *J. Vac. Sci Technol. A*, **19**, 1742 (2001)
88. T. Minami, Y. Kuroi and S. Takata, *J. Vac. Sci Technol. A*, **14**, 1736 (1996)
89. T. Minami, T. Miyata and Y. Sakagami, *Surf. Coat. Tech.*, **108**, 594 (1998)
90. M. Flynn and A. H. Kitai, *J. Electrochem. Soc.*, **148**, H149 (2001)
91. J. S. Kim, S. G. Lee, H. L. Park, J. Y. Park and S. D. Han, *Mater. Lett.*, **58**, 1354 (2004)
92. B. Qiao, Z. L. Tang, Z. T. Zhang and L. Chen, *Mater. Lett.*, **61**, 401 (2007)
93. Z. Liu, X. Jing and L. Wang, *J. Electrochem.Soc.*, **154**, H500 (2007)
94. V. Bondar, S. Popovich, T. Felter and J. F. Wager, *Mater. Res. Symp. Proc.* **667**, G761 (2001)

- 
95. J. P Bender, J. F Wager, J. Kissick, B. L Clark and D. A. Keszler, *J. Lumin.*, **99**, 311 (2002)
  96. J. S. Lewis and P. H. Holloway, *J. Electrochem. Soc.*, **147**, 3148 (2000)
  97. T. Miyata, Y. Mochizuki and T. Minami, *IEICE Trans. Electron.*, **E88**, 2065 (2005)
  98. L. C. Williams, D. P. Norton, J. Budai and P.H Holloway, *J. Electrochem. Soc.*, **151**, H188 (2004)
  99. C. Baker, J. Heikenfeld and A. J Steckl, *IEEE J. Selected top. Quantum Elec.*, **8**, 1420 (2002)
  100. M. Itoh, *Chem. Rev.*, **103**, 3835, (2003)
  101. K. G. Cho, D. Kumar, S. L. Jones, D. G. Lee, P. H. Holloway and R. K. Singh, *J. Electrochem. Soc.*, **145**, 3456 (1998)
  102. A. Konrad, U. Herr, R. Tidecks, F. Kummer and K. Samwer, *J. Appl. Phys.*, **90**, 3516 (2001)
  103. F. Parsapour, D. F. Kelley and R. S. Williams, *J. Phys. Chem. B*, **102**, 7971 (1998)
  104. S. L. Jones, D. Kumar, R.K. Singh, and P. H. Holloway, *Appl. Phys. Lett.*, **71**, 404 (1997)
  105. R. A. Buchanan, K. A. Wickersheim, J. L. Weaver and E. E. Anderson, *J. Appl. Phys.*, **39**, 4342 (1968)
  106. S. H. Shin, J. H. Kang, D. Y. Jeon, S. H. Choi, S. H. Lee, Y. C. You and D. S. Zang, *Solid State Commun.*, **135**, 30 (2005)
  107. S. H. Shin, J. H. Kang, D. Y. Jeon and D. S. Zang, *J. Lumin.*, **114**, 275 (2005)

108. M. K. Jung, W. J. Park and D. H. Yoon, *Sensor. Actuat. B-Chem*, **126**, 328 (2007)
109. S. Sakuma, H. Kominami, Y. Neo, T. Aoki, Y. Nakanishi and H. Mimura, *Appl. Surf. Sci.*, **244**, 458 (2005)
110. M. V. Nazarov, J. H. Kang, D.Y. Jeon, E.-J. Popovici, L. Muresan and B. S. Tsukerblat, *Solid State Commun.*, **133**, 183 (2005)
111. N. Rakov, W. Lozano B, G. S. Maciel and C. B. de Araujo, *Chem. Phys. Lett.*, **428**, 134 (2006)
112. E. -J. Popovici, L. Muresan, H. Amalia, E. Indrea and M. Vasilecu, *J. Alloys and Compd.*, **434**, 809 (2007)
113. M. Kottaisamy, D. Jeyakumar, R. Jagannathan and M. Mohan Rao, *Mat. Res. Bull.*, **31**, 1013 (1996)
114. Y. C. Kang, H. S. Roh and S. B. Park, *Adv. Mater.*, **12**, 451 (2000)
115. J. Hao, S.A. Studenikin and M. Cocivera, *J. Lumin.*, **93**, 313 (2001)
116. Y. K. Lee, J. R. Oh and Y. R. Do, *Appl. Phys. Lett.*, **91**, 041907 (2007)
117. J. Y. Cho, Y. D. Huh, C. R. Park and Y. R. Do, *J. Electrochem. Soc.*, **154**, J272 (2007)
118. J. Y. Cho, K. Y. Ko and Y. R. Do, *Thin solid films*, **515**, 3373 (2007)
119. T. Travlos, N. Boukos, G. Apostolopoulos and A. Dimoulas, *Appl. Phys. Lett.*, **82**, 4053 (2003)
120. A. F. Jankowski, L. R. Schrawyer and J. P. Hayes, *J. Vac. Sci. Technol. A*, **11**, 1548 (1993)
121. E. K. Evangelou, C. Wiemer, M. Faniculli, M. Sethu and W. Cranton, *J. Appl. Phys.*, **94**, 318 (2003)

- 
122. K. Y. Ko, Y. K. Lee, Y. R. Do and Y. D. Huh, *J. Appl. Phys.*, **102**, 013509 (2007)
  123. D. S. Zang, K. Y. Ko, H. K. Park, D. H. Yoon and Y. R. Do, *J. Electrochem. Soc.*, **155**, J111 (2008)
  124. J. McKittrick, C.F. Bacalski, G.A. Hirata, K. M. Hubbard, S. G. Pattillo, K. V. Salazar and M. Trkula, *J. Am. Ceram. Soc.*, **83**, 1241 (2000)
  125. M. B. Korzenski, Ph. Lecoer, B. Mercey, D. Chippaux, B. Raveau and R. Desfeux, *Chem. Mater.*, **12**, 3139 (2000)
  126. K. G. Cho, D. Kumar, P. H. Holloway and R. K. Singh, *Appl. Phys. Lett.*, **73**, 3058 (1998)
  127. S. Zhang and R. Xiao *J. Appl. Phys.*, **83**, 3842 (1998)
  128. D. Kumar, K. G. Cho, Zhan Chen, V. Craciun, P. H. Holloway, and Rajiv K. Singh, *Phys. Rev. B*, **60**, 331 (1999)
  129. H. J. Gao, D. Kumar, K.G. Cho, P.H. Holloway, R.K. Singh, X.D. Fan, Y. Yan and S.J. Pennycook, *Appl. Phys. Lett.*, **75**, 2223 (1999)
  130. S. L. Hones, D. Kumar, K.G. Cho, R. Singh, and P. H. Holloway, *Displays* **19**, 151 (1999)
  131. V. Craciun, J. Howard, E. S. Lambers, R. K. Singh, D. Craciun and J. Perriere, *Appl. Phys. A*, **69**, S535 (1999)
  132. D. Kumar, J. Sankar, K.G. Cho, V. Craciun and R. K. Singh, *Appl. Phys. Lett.*, **77**, 2518 (2000)
  133. O. P. Y. Moll, J. Perriere, E. Millon, R. M. Defourneau, D. Fourneau, B. Vincent, A. Essahloui, A. Boudrioua and W. Seiler, *J. Appl. Phys.*, **92**, 4885 (2002)

134. J. S. Bae, J. H. Jeong, S. S. Yi and J. C. Park, *Appl. Phys. Lett.*, **82**, 3629 (2003)
135. S. Bar, G. Huber, J. Gonzalo, A. Perea and M. Munz, *Appl. Phys. A*, **80**, 209 (2005)
136. S. H. Yanga, T. J. Hsueha and S. J. Chang, *J. Cryst. Growth*, **287** 194 (2006)
137. S. S. Yi, K. S. Shim, H. K. Yang, B. K. Moon, B. C. Choi, J. H. Jeong, J. H. Kim and J. S. Bae, *Appl. Phys. A*, **87**, 667 (2007)
138. T. Suyama, K. Okamoto and Y. Hamakawa, *Appl. Phys. Lett.*, **41**, 462 (1982)
139. T. Minami, M. Yamazaki, T. Miyata and T. Shirai, *Jpn. J. Appl. Phys.*, **40**, L864 (2001)
140. T. Minami, Y. Kobayashi, T. Miyata and M. Yamazaki, *Thin solid films*, **443**, 91 (2003)

## **CHAPTER 2**

---

### **Experimental Techniques and Characterization Tools**

---

*This chapter describes about the experimental techniques used for preparing bulk oxide phosphors and thin film growth. Also analytical tools that are used to characterize these synthesized phosphors and thin films.*

Growth techniques do play a significant role in influencing the physico-chemical characteristics of bulk powders as well as thin film materials. It has been observed that various physical constants, characteristic to a bulk material, need not remain the same in their corresponding thin films. The structural, electrical and optical properties of thin films are found to be highly sensitive to the technique adopted, the substrate chosen, deposition conditions, the presence of defects and impurities and the film thickness. The appropriate choice of an experimental technique thereby helps in tailoring a material with controlled, reproducible and well-defined properties so as to suit a technological application.

The research work presented in the thesis is focused on development of oxide phosphors for thin film electroluminescent (TFEL) device applications. Physical vapour deposition (PVD) techniques such as radio frequency (rf) magnetron sputtering and pulsed laser deposition (PLD) were used to grow phosphor thin films. Rf magnetron sputtering was used to deposit thin films of  $\text{ZnGa}_2\text{O}_4\text{:Mn}$ ,  $\text{Zn}_2\text{GeO}_4\text{:Mn}$  and top insulator ( $\text{BaTa}_2\text{O}_6$ ) for TFEL device fabrication. PLD was used to grow high quality thin films of  $\text{Y}_2\text{O}_3\text{:Eu}^{3+}$  on amorphous substrate. Thermal evaporation was used to deposit metal electrodes (aluminum) to complete the device structure with top electrical contact. The present chapter discusses the various methodologies adopted for bulk phosphor synthesis and thin film growth. It also briefs on the different analytical techniques used in the present study.

## **2.1. Bulk synthesis techniques**

The targets for both sputtering and PLD techniques, were synthesized in the laboratory from highly pure starting materials. Powder target of

$\text{ZnGa}_2\text{O}_4:\text{Mn}^{2+}$ ,  $\text{Zn}_2\text{GeO}_4:\text{Mn}^{2+}$  was used for sputter deposition. A one inch pellet of  $\text{Y}_2\text{O}_3:\text{Eu}^{3+}$  was used as the target for the laser ablation.

For preparing bulk  $\text{ZnGa}_2\text{O}_4:\text{Mn}^{2+}$ ,  $\text{Zn}_2\text{GeO}_4:\text{Mn}^{2+}$  powders and the powder target for sputtering, stoichiometric quantities of the starting materials were thoroughly mixed in alcohol medium and fired in a high temperature furnace (1350°C for  $\text{ZnGa}_2\text{O}_4:\text{Mn}^{2+}$  and 1200°C for  $\text{Zn}_2\text{GeO}_4:\text{Mn}^{2+}$ ) for a fixed time of 12 hrs.

A two-step firing process is usually adopted for  $\text{Y}_2\text{O}_3:\text{Eu}^{3+}$  pellet synthesis. The constituent materials, after thorough mixing, are calcined at 1200°C. This powder with some suitable amount of binder (Poly vinyl alcohol) is then pressed into a one inch diameter pellet using a hydraulic press on applying a force of 3 tons. The pellet is then sintered to ensure denser pellet for better thin film growth. During sintering, the temperature is to be raised in steps to completely remove moisture from the target. Moisture, if trapped inside the target, leads to cracking during firing. Normally, the outer part of a target heats up faster than the inner part. If the temperature were increased too quickly from room temperature to the high processing temperature, the outer part of the target would become dense before the moisture in the inner part escapes. So the pellet is slowly heated to 100°C and kept there for some time to ensure the whole water has been evaporated. Since we add binder which is an unwanted impurity, should be removed. Normally PVA evaporates at 300°C. So the pellet is now slowly heated to 300°C and kept at this temperature for some time to ensure the evaporation of binder. The sintering temperature, 1500°C is attained through a series of steps with the help of a programmable furnace. In the present study,  $\text{Y}_2\text{O}_3:\text{Eu}^{3+}$  was sintered at 1500°C for 48 hrs in air.

## **2.2. Thin film growth techniques**

A ‘thin film’ has one of its linear dimensions very small compared to the other two and is characterized by a large surface to volume ratio. Any thin film deposition process involves the following sequential steps [1]:

Transition of the condensed phase (solid or liquid) into the gaseous state (atomic/molecular/ionic species)

Transport of the vapor from the source to the substrate

Condensation of the vapor upon arrival on the substrate

The deposition techniques are broadly classified into two - physical and chemical - depending on how the atoms/molecules/ions/clusters of the species are created for condensation process. Various chemical methods have been realized for thin film deposition of phosphor materials. Some of them are sol-gel synthesis [2,3], solvent evaporation epitaxy method [4], electrophoresis [5], spray pyrolysis [6,7] and dip-coating [8]. Thermal and electron-beam evaporation, pulsed ion-beam evaporation [9], chemical vapor deposition (CVD) [10], PLD, rf sputtering, and atomic layer epitaxy (ALE) falls under the stream of physical methods generally adopted for thin film phosphor growth. The following sections briefs the various thin film deposition techniques used in the present work.

### **2.2.1 Thermal evaporation by resistive heating**

Thermal evaporation is a simple and convenient technique widely used for the deposition of thin films of metals, alloys and many compounds. The process, in general, involves heating up of a source material until it evaporates and condenses on a cold target surface, referred to as the substrate. If carried out

in vacuum, the evaporation temperature can be considerably lowered and the formation of oxides and incorporation of impurities in the growing layer can be avoided. Moreover, at pressures as low as  $10^{-6}$  or  $10^{-5}$  Torr, the mean free path of vapor atoms shall be of the same order as the vacuum chamber dimensions. Hence, the particles can travel in straight lines from the evaporation source towards the substrate without being significantly scattered [11].

In thermal evaporation technique, the average energy of vapor atoms reaching the substrate surface is generally low (of the order of  $kT$ , ie. tenths of eV). Here, a refractory metal (tungsten or tantalum) strip or shaped filaments are heated directly by attaching the ends to a low-voltage, high-current supply to evaporate the charge. The characteristics and quality of the deposited film shall depend on the substrate temperature, rate of deposition, ambient pressure, etc. The homogeneity of the film depends on the geometry of the evaporation source and the distance from the source material to the substrate. Excellent and detailed reviews on the know-how of the technique have been discussed by Holland [12].

In the present work, the deposition of metal electrodes (Al) was done using thermal evaporation via resistive heating.

### **2.2.2 Sputtering**

Sputter deposition is one of the most widely used techniques for the fabrication of thin-film structures. In 1852 Sir W.R. Grove discovered surface coatings generated in the valve. It was called as 'Spluttering', meaning the generation of drop out of a liquid surface by an impinging primary drop. The expression 'Sputtering' was a printer's error but was soon adopted as a scientific term. Sputtering is one of the most widely used technologies to prepare thin

films. In sputter deposition, material is removed - as atoms or molecules - from a solid target by energetic ion bombardment and deposited as atomic layers on a substrate. By applying a high RF or DC voltage between the target (cathode) and the substrate (anode), energetic electrons emitted from the target form ions in the process gas, typically argon at 1 to 100 mTorr pressure. Under these conditions, plasma - a partially ionized gas - is formed. When a target is sputtered with ions, following phenomena may occur. 1) The ions may get reflected, probably being neutralized in the process. This reflection is the basis of technology known as ion scattering spectroscopy. 2) The impact of the ion may cause the target to eject an electron, usually referred as secondary electrons. 3) The ion may become buried in the target-known as ion implantation. 4) The ion impact may also be responsible for some structural rearrangements in the target material. Rearrangements include simple vacancies and interstitials or more gross lattice defects such as change in stoichiometry in the case of alloys and compound targets. 5) The ion impact may set up a series of collisions between the atoms of the target, possibly leading to ejection of atoms known as sputtering.

A DC sputtering system cannot be applied to insulator target, because of the immediate build up of positive charge at the surface of target. In order to sustain the glow discharge with an insulator target, rf power should be applied. RF sputtering process operates on the order of megahertz, usually 13.56 MHz, the frequency allotted by international communication authorities. When an rf power is applied to the target, electrons which could exist in the sputtering gas, or could be emitted from the target or chamber wall, are discharged and scattered with sputtering gas, according to current between target and ground. In this process some of the Ar ions are also get ionized. According to rf frequency,

the electrons are accelerated and travel between the electrodes (ground and target). Since Ar atoms are heavier compared to electrons, Ar ions cannot respond to the frequency and therefore oscillates only in short distances. Due to this effect operating pressure to achieve plasma in rf sputtering is lower than that in dc sputtering. Also sputtering yield gets improved. In the case of magnetron sputtering, since electrons are confined around the target, they get more chance to collide with Ar atom, thereby increasing Ar ion plasma to sputter the target. The secondary electrons emitted from the target sustain the plasma near the target. Therefore operating pressure could be reduced further. Since the surface area of the target is less than the ground or the wall of the chamber, the configuration of the electrodes is asymmetric. Due to this asymmetric configuration of the electrodes and mobility difference between electrons and ions, target is displaced to a negative potential with a mean known as dc offset which induces sputtering. Therefore target will acquire a self-bias and will have a value equal to half of the applied rf peak to peak voltage. This dc offset will give rise to sputtering at the target. The rf voltage that gives rise to sputtering will be a function of pressure inside the chamber and the current will be proportional to the ion flux. In 1935 Penning first studied and low pressure dc magnetron sputtering in a system that was composed of coaxial cylindrical electrodes with an axial magnetic field. But these kinds of systems are not used in practice. In the early 1960s, magnetron sputtering was reconsidered as an attractive process for thin film deposition. Gill and Kay proposed an inverted magnetron sputtering system and demonstrated that the sputtering gas pressure was as low as  $10^{-5}$  Torr [13]. Kesaer and Pashkova [14] gave the basic idea of

the planar magnetron sputtering, and Hayakawa and Wasa [15] invented an early planar magnetron sputtering system with a solenoid coil.

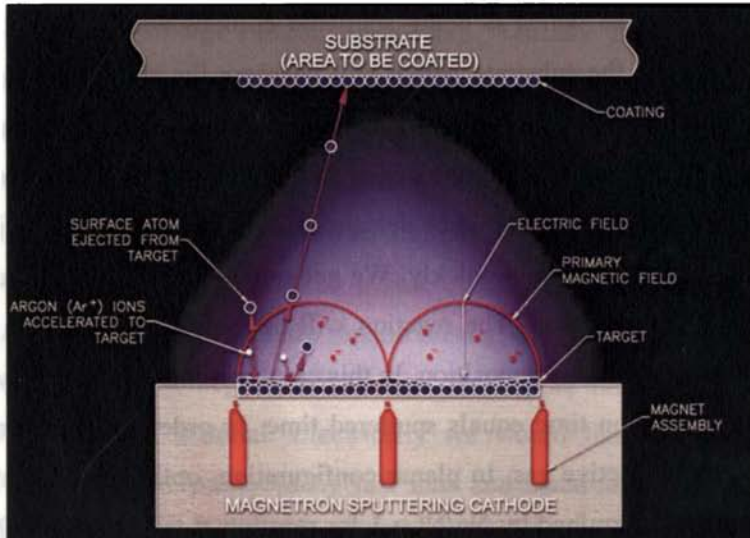


Figure 2.1 Schematic diagram of sputtering process

Nowadays, the planar type using permanent circular magnets is widely used because of such advantages as its simple structure, suitable adaptation, and wide coating area in spite of the disadvantage of the localized erosion of target that causes the deposition rates to change over a period of time.

## 2.2.3 Sputtering Parameters

### a) Sputtering gas

Noble gases are usually used in sputtering due to their chemical inactivity. Among them Ar is a better choice as it is cheaper and has sputtering yield 'two' down on Xe and Kr. The glow discharge is sustained by electrons

making collisional ionizations with Ar gas. Therefore increasing Ar pressure will increase the sputtering yield. A different problem however exists at higher pressures. The material which is being sputtered collides with the Ar ions/gas atoms on its way to the substrate which will decrease the sputtering yield. So there is an appropriate pressure, for which, sputtering yield is a maximum. This is determined by the size and geometry of chamber and gun. The space between ground and target electrodes should be designed not to be narrow or labyrinthine for Ar gas to diffuse easily and quickly. We get stoichiometric films in reactive sputtering due to this reason. The reaction will be taking place at both target surface and substrate during deposition. In this case maximum sputtering yield is obtained when reaction time equals sputtered time. In order to deposit oxides, we use oxygen as reactive gas. In planar configuration, optimum concentration of reactive gas is determined by  $N_g/N_t > 1$  for reaction at target, and  $N_g/N_s > 1$  for reaction at substrate, where  $N_g$  is the number of reactive gas molecules which strike unit area of target/substrate per unit time,  $N_t$  is number of sputtered atoms per unit area of the target per unit time and  $N_s$  is number of deposited atoms per unit area of the substrate per unit time. The minimum oxygen partial pressure can be calculated from the above relations. However in practice optimum partial pressures can be found out by trial and error experiment. If the reaction takes place at the target, sputtering yield is reduced. So the gas inlets of sputtering gas and reactive gas are separated from each other inside the chamber. For example a relatively big ground shield surrounds the target and the sputtering gas is injected through the inlet near to the target at higher pressure than the reactive gas. And by putting the reactive gas inlet near the substrate, the reaction can be improved with a relatively high deposition yield.

## **b) Sputtering Power**

For each operating pressure, target material and sputtering gas, there is a specific voltage-current relationship. Actually target material is not that important even though the secondary electron coefficient varies from target to target. Under similar conditions current densities are very much alike, except for some conducting targets. The sputtering rate of the target is determined by the flux of ions and energetic neutrals and hence the sputtering yield. An ion current of  $1\text{mA}/\text{cm}^2$  corresponds to a flux of  $6 \times 10^{15}$  singly charged ions per  $\text{cm}^2/\text{sec}$ . The sputtering yield rises monotonically with ion energy up to several tens of KeV, where it begins to decrease. This upper limit of ion energy is dependent on target material. Electrically we would like low voltages and because x-rays can be produced by fast ions and electrons we ought to keep energies and voltages below 10KV. In order to transfer the power to the target it is necessary to minimize the impedance between the power supply and target. Thus electric connectors with low capacitance must be used and good electric shields are required in order not to leak the rf power. During the deposition of the film, the impedance changes due to the deposition onto the walls of the chamber and the ground shield. Hence adjustments are sometimes necessary. It is very important for the deposition of the oxides and nitrides whose resistance is very large.

## **c) Ground shields**

The purpose of ground shield, or dark space shield, is to restrict ion bombardment to the target and sputtering to the target only. Otherwise the target backing plate, mounting clips and mechanical supports would also be sputtered and films get contaminated. In order to prevent ion bombardment of the

protected regions, the space between the target and ground shield must be less than the thickness of the dark space. This criterion is such as to prevent the establishment of self-sustained discharge in the space between the target and shield. Occasionally one finds that sharp points or patches of dirt cause local discharges or arcs, particularly with dc discharges, and these should be eliminated. Since the thickness of the dark space decreases with increase in pressure, size of the gap between target and shield sets an upper pressure limit for operating the system. In principle, the gap should be extremely small, but in practice it is limited by spurious discharges and in case of rf discharges, by increasing capacitive target to ground coupling as the gap is decreased which will result in serious loss of electric power. The dark space thickness also decreases with frequency too. So systems operating above 13.56 MHz need to have correspondingly closer ground shields. Generally 2-3 mm of the target-ground separation is reasonable.

#### **d) Target cooling**

Sputtering is a very inefficient process and most of the power input to the gun appears finally as target heating. Such heating can become excessive – local temperatures of 400°C have been reported and can lead to damage of the bonding between the target and backing electrode of the target itself and associated O-rings etc. This is usually avoided by cooling the target with water or another suitable liquid. On the other hand such cooling is complexity and it can be avoided if the power input to the target is not too great. When water is used as coolant, electric current leaks through water. Hence the resistance of water must be high enough. In this sense de-ionised water is the best choice. In

general, with the sputtering gun, the permanent magnets sit in the cooling water to prevent the magnets from losing magnetic field due to over heating.

### **e) Control of sputtering parameters**

The sputtering parameters can be controlled for optimized thin film quality. McMahon *et al.* have developed a fully computerized planar sputtering system for thin film deposition for AlN [16]. They had deposited films under adequate partial pressures of argon and nitrogen gases under following conditions. 1) Control of gas flows under constant rf powers; 2) Control of rf power under constant gas flows; 3) control of target rf voltage instead of rf power under constant gas flows. They reported that the third method was most stable and the films developed in this condition were best. This is an important fact in sputtering deposition. During deposition due to change in impedance between the target and ground shields or the wall of the chamber, the current is changed for a constant power. Therefore instead of controlling the power, it is important to control the target voltage, which accelerates the ions. This result can be applied when oxide films are deposited as well as pure semiconductors.

The advantages of sputtering over evaporation techniques are:

- higher kinetic energy of deposited atoms results in better film adhesion;
- more easily automated for in-line industrial processing;
- no 'spitting' occurs that would leave cluster of material on the substrate;
- sputter source can be mounted in any orientation;
- plasma is energetically hot, but has a small thermal capacity;
- since coverage is independent of line-of-sight, sputtering inherently produces uniform film coatings over non-flat surfaces;

- refractory materials, elements, mixtures and alloys can be sputtered with equal facility;
- most importantly, sputtering with oxygen (or nitrogen) in the argon process gas leaves the target unreacted, yet deposits an oxide (or nitride) film on the substrate.

This last advantage is often used to produce nonconductive film, since 'reactive' DC sputtering of a metal allows higher deposition associated with RF sputtering.

## **2.2.4 Pulsed laser deposition (PLD)**

In material science, lasers play a significant role either as a passive component for process monitoring or as an active tool by coupling its radiation energy to the material being processed, leading to various applications such as localized melting during optical pulling, laser annealing of semiconductors, surface cleaning by desorption and ablation, laser induced rapid quench to improve surface hardening and most recently pulsed laser deposition (PLD) for growing thin films [17]. PLD is the deposition method of choice when one needs to deposit materials with complex stoichiometry. PLD was the first technique successfully used to deposit a superconducting  $\text{YBa}_2\text{Cu}_3\text{O}_{7-d}$  thin film. Since then, many materials, especially multi-element oxides, normally difficult to be deposited by other methods, have been deposited by PLD. This technique offers many potential applications, from integrated circuits and optoelectronics to micro mechanics and medical implants [18].

In a typical PLD process, a focused train of high energy laser pulses, derived from a UV nanosecond pulsewidth laser source, such as the frequency tripled (355 nm) or quadrupled (256 nm) solid state Nd:YAG laser, or the KrF

(248 nm) or ArF (193 nm) excimer laser, is rastered over either a metal, a single crystal oxide, or a compressed oxide powder target in a vacuum chamber. The high pulse energy beam–target interaction creates a plume comprised of atomic and molecular species ablated from the target. A substrate, often heated, is placed at a short distance from the target in the direction of the advancing plume (figure 2.2). Though the actual physical process of material removal is quite complex, one can consider the ejection of material, to occur from rapid explosion of the target surface by superheating. Unlike thermal evaporation, which produces a vapor composition dependent on the vapor pressures of elements in the target material, the laser-induced expulsion produces a plume of material with stoichiometry similar to the target.

The best quality films can be deposited by controlling the fundamental criteria such as the substrate temperature, the relative and absolute arrival rates of atoms and the energy of the depositing flux. PLD offers the best control over these criteria than other vacuum deposition techniques [19].

The main advantages of pulsed laser deposition are:

- **conceptually simple:** a laser beam vaporizes a target surface, producing a film with the same composition as the target.
- **versatile:** many materials can be deposited in a wide variety of gases over a broad range of gas pressures.
- **cost-effective:** one laser can serve many vacuum systems.
- **fast:** high quality samples can be grown reliably in 10 or 15 minutes.
- **scalable:** as complex oxides move toward volume production.

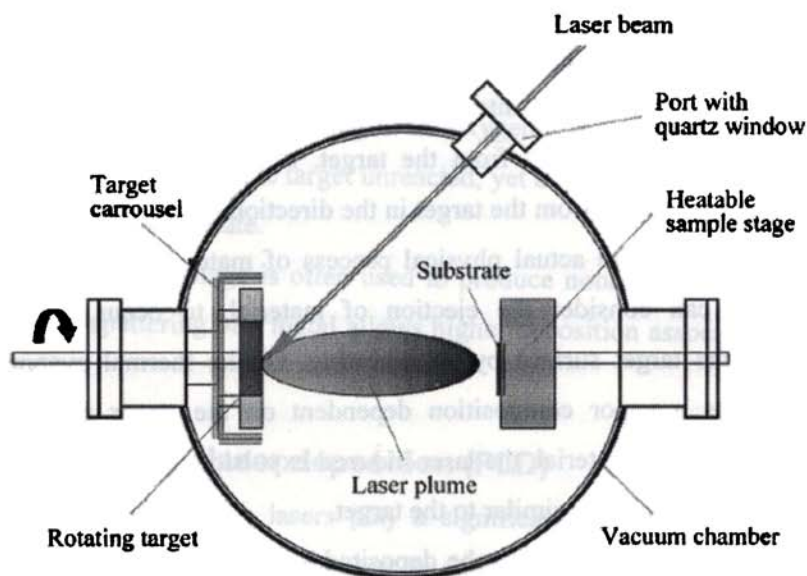


Figure 2.2 Schematic diagram of PLD chamber

The mechanism of pulsed laser deposition, in contrast to the simplicity of the set-up, is a very complex physical phenomenon. It not only involves the physical process of the laser-material interaction, but also the formation plasma plume with high energetic species and even the transfer of the ablated material through the plasma plume onto the substrate surface. Thus the thin film formation in PLD generally can be divided into the following four stages.

1. Laser radiation interaction with the target
2. Dynamics of the ablated materials.
3. Deposition of the ablation materials on the substrate.
4. Nucleation and growth of a thin film on the substrate surface

Each stage in PLD is critical to the formation of quality epitaxial, crystalline, stoichiometric and uniform thin films.

In the first stage, the laser beam is focused onto the surface of the target. At sufficiently high flux densities and short pulse duration, all elements in the target are rapidly heated up to their evaporation temperature. Materials are dissociated from the target surface and ablated out with stoichiometry as in the target. The instantaneous ablation rate is highly dependent on the fluence of the laser shining on the target. The ablation mechanisms involve many complex physical phenomena such as collisional, thermal, and electronic excitation, exfoliation and hydrodynamics.

During the second stage the emitted materials tend to move towards the substrate according to the laws of gas-dynamics and show the forward peaking phenomenon. The spatial thickness varies as a function of  $\cos\theta$ . The spot size of the laser and the plasma temperature has significant effects on the deposited film uniformity. The target-to-substrate distance is another parameter that governs the angular spread of the ablated materials. A mask placed close to the substrate could reduce the spreading. Typical plasma temperature measured by emission spectroscopy during initial expansion of the plume is  $\approx 10,000$  K, which is well above the boiling point of most materials ( $\approx 3000$  K). Heating of the plasma to these temperatures is thought to occur by inverse-Bremsstrahlung absorption of the laser light in a free – free transition of electron ion pair. This high temperature would evaporate the surface layer of the target thereby producing exact composition in the thin films.

The third stage is important to determine the quality of thin film. The ejected high-energy species impinge onto the substrate surface and may induce

various type of damage to the substrate. These energetic species sputter some of the surface atoms and a collision region is formed between the incident flow and the sputtered atoms. Film grows after a thermalized region is formed. The region serves as a source for condensation of particles. When the condensation rate is higher than the rate of particles supplied by the sputtering, thermal equilibrium condition can be reached quickly and film grows on the substrate surface at the expenses of the direct flow of the ablation particles and the thermal equilibrium obtained.

The effect of increasing the energy of the adatoms has a similar effect of increasing substrate temperature on film growth [19]. Typical power densities involved in PLD are approximately  $50 \text{ MWcm}^{-2}$  for a reasonable growth rate. ( $> 1 \text{ A}^\circ/\text{shot}$ ) If plasma is formed during laser target interaction in vacuum or in air then an explicit laser – plasma interaction occurs due to which ions in the plasma are accelerated to as much as  $100 - 1000 \text{ eV}$  [18]. Nucleation-and-growth of crystalline films depends on many factors such as the density, energy, ionization degree, and the type of the condensing material, as well as the temperature and the physico-chemical properties of the substrate. The two main thermodynamic parameters for the growth mechanism are the substrate temperature  $T$  and the supersaturation  $D_m$  related by the following equation:

$$D_m = kT \ln(R/R_e) \quad (2.6)$$

where,  $k$  is the Boltzmann constant,  $R$  is the actual deposition rate, and  $R_e$  is the equilibrium value at the temperature  $T$ .

The nucleation process depends on the interfacial energies between the three phases present - substrate, the condensing material and the vapour. The critical size of the nucleus depends on the driving force, i.e. the deposition rate

and the substrate temperature. For the large nuclei, a characteristic of small super-saturation, they create isolated patches (islands) of the film on the substrate, which subsequently grow and coalesce together. As the super-saturation increases, the critical nucleus shrinks until its height reaches on atomic diameter and its shape is that of a two-dimensional layer. For large super-saturation, the layer-by-layer nucleation will happen for incompletely wetted foreign substrates.

The crystalline film growth depends on the surface mobility of the adatom (vapour atoms). Normally, the adatom will diffuse through several atomic distances before sticking to a stable position within the newly formed film. The surface temperature of the substrate determines the adatom's surface diffusion ability. High temperature favours rapid and defect free crystal growth, whereas low temperature or large supersaturation crystal growth may be overwhelmed by energetic particle impingement, resulting in disordered or even amorphous structures.

The mean thickness ( $N_{99}$ ) at which the growing thin and discontinuous film reaches continuity, is given by the formula:

$$N_{99} = A(1/R)^{1/3} \exp(-1/T) \quad (2.7)$$

where  $A$  is a constant related to the materials [18]. In the PLD process, due to the short laser pulse duration ( $\sim 10$  ns) and hence the small temporal spread ( $\leq 10$  ms) of the ablated materials, the deposition rate can be enormous ( $\sim 10$  nm/s). Consequently a layer-by-layer nucleation is favoured and ultra-thin and smooth film can be produced. In addition, the rapid deposition of the energetic ablation species helps to raise the substrate surface temperature. In this

respect, PLD tends to demand a lower substrate temperature for crystalline film growth.

In the present study, PLD was used to deposit  $Y_2O_3: Eu^{3+}$  phosphor films. Pulsed laser deposition of thin films was carried out in a vacuum chamber pumped by a turbo-molecular pump (Pfeiffer Vacuum Inc, Germany). The laser used was the fourth harmonics (266 nm) of Nd:YAG laser (Spectra Physics model LAB 170).

### 2.3 Device Fabrication

Alternating current thin film electroluminescent (ACTFEL) devices can be fabricated in vacuum and non-vacuum environments. Practical TFEL devices are expensive as a consequence of using vacuum assisted techniques for film growth. To resolve the problem of cost, new techniques have been explored to eliminate the need for vacuum processes. As oxide phosphors are less moisture sensitive, solution coating techniques [20] and sol-gel synthesis [21] can be used for fabricating devices.

In the present work, rf magnetron sputtering was used to deposit the light emitting layer and the top insulating layer of the fabricated ACTFEL devices. The top electrode was thermally evaporated onto the device to complete the standard metal-insulator-semiconductor-insulator-metal (MISIM) structure. Commercially available Ohara (supplied by Planar Inc.) and nippon electric glass (NEG) substrates coated with indium tin oxide (ITO) and aluminium titanium oxide (ATO) were used for device fabrication. These substrates could withstand a temperature of up to a maximum of 650°C.

## **2.4 Characterization tools**

Once the films are grown, the structural, compositional, morphological, optical and electrical analytical tools give a better understanding of the film properties. On the reverse, the characterization techniques help in optimizing the growth conditions to get device quality films. In the following sections, the techniques used for the film characterizations in the present study are discussed briefly.

### **2.4.1 Thin film thickness**

Film thickness has a crucial role in determining its properties unlike a bulk material. The properties of the thin films can be reproduced if thickness, along with other deposition parameters, is kept constant. Film thickness may be measured either by in-situ monitoring of the rate of deposition or after the film deposition. The thicknesses of the thin films prepared for the work presented in this thesis were measured by a stylus profiler (Dektak 6M).

The stylus profiler takes measurements electromechanically by moving the sample beneath a diamond tipped stylus. The high precision stage moves the sample according to a user defined scan length, speed and stylus force. The stylus is mechanically coupled to the core of a linear variable differential transformer (LVDT). While in contact over the moving sample surface, surface variations cause the stylus to be translated vertically. Electrical signals corresponding to the stylus movement are produced as the core position of the LVDT changes. The LVDT scales an ac reference signal proportional to the position change, which in turn is conditioned and converted to a digital format through a high precision, integrating, analog-to-digital converter [21].

To measure the film thickness, a region of the substrate has to be masked during film deposition. This creates a step on the sample. The thickness of the sample can then be measured accurately by measuring the vertical motion of the stylus over the step.

## **2.4.2 Structural Characterization**

The crystallographic nature of a sample very well influences its electrical and optical properties. The structural characterization of the bulk and thin film samples were done in the present study by recording the x-ray diffraction (XRD) pattern. Any material has a characteristic diffraction pattern, whether present in pure state or as one the constituent of a mixture of substances. This fact is made useful in the diffraction method of chemical analysis. The advantage of XRD analysis is that it discloses the presence of a substance, as that substance actually exists in the sample and not in terms of its constituent chemical elements. Hence, diffraction analysis is useful whenever it is necessary to know the state of chemical combination of the elements involved or the particular phase in which they are present. Compared with ordinary chemical analysis the diffraction method has the advantage that it is usually much faster, requires only very small quantity of sample and is non destructive [22].

The basic law involved in the diffraction method of structural analysis is the Bragg's law. When monochromatic beam of x-rays impinge upon the atoms in a crystal lattice, each atom acts as a scattering source. The crystal lattice presents a series of parallel reflecting planes to the incident x-ray beam. The intensity of the reflected beam at certain angles will be maximum when the path difference between two reflected waves from two different crystal planes is an integral multiple of  $\lambda$ . This condition is termed as Bragg's law and is given by,

$$n\lambda = 2d\sin\theta \quad (2.8)$$

where,  $n$  is the order of diffraction,  $\lambda$  is the wavelength of x-rays,  $d$  is the spacing between consecutive parallel planes and  $\theta$  is the glancing angle (or the complement of the angle of incidence) [23].

X-ray diffraction studies give a whole range of information about the crystal structure, orientation, average crystalline size and stress in the powder. Experimentally obtained diffraction patterns of the sample are compared with the standard powder diffraction files published by the International Centre for Diffraction Data (ICDD). The average grain size of the film can be calculated using the Scherrer's formula [22],

$$d = \frac{0.9\lambda}{\beta \cos\theta} \quad (2.9)$$

where,  $\lambda$  is the wavelength of the x-ray used and  $\beta$  is the full width at half maximum in radians. The lattice parameter values for different crystallographic systems can be calculated from the following equations using the (hkl) parameters and the interplanar spacing  $d$ .

$$\text{Cubic system,} \quad \frac{1}{d^2} = \frac{h^2 + k^2 + l^2}{a^2} \quad (2.10)$$

$$\text{Tetragonal system,} \quad \frac{1}{d^2} = \frac{h^2 + k^2}{a^2} + \frac{l^2}{c^2} \quad (2.11)$$

$$\text{Hexagonal system,} \quad \frac{1}{d^2} = \frac{4}{3} \left( \frac{h^2 + hk + k^2}{a^2} \right) + \frac{l^2}{c^2} \quad (2.12)$$

$$\text{Orthorhombic system,} \quad \frac{1}{d^2} = \frac{h^2}{a^2} + \frac{k^2}{b^2} + \frac{l^2}{c^2} \quad (2.13)$$

X-ray diffraction measurements of the samples in the present studies were done using Rigaku automated x-ray diffractometer. The filtered copper  $K_{\alpha}$  radiation ( $\lambda = 1.5418\text{\AA}$ ) was used for recording the diffraction pattern.

### **2.4.3 Morphological analysis**

Surface morphology is an important property while going for multilayer device fabrication. Roughness of the thin film surface plays a vital role, especially while making interfaces. Some of the characterization tools used to study about the surface of thin films is described below.

#### **(a) Scanning electron microscope (SEM)**

The scanning electron microscope (SEM) uses electrons rather than light to form an image. SEM has several advantages over an ordinary light microscope [24]. The SEM has a large depth of field, which allows a large amount of the sample to be in focus at a time. The SEM also produces images of high resolution, which means that closely spaced features can be examined at a high magnification. Preparation of the samples is relatively easy since most SEMs only require that sample should be conductive. The combination of higher magnification, larger depth of focus, greater resolution, and ease of sample observation makes the SEM one of the most heavily used instruments in current research areas.

In a typical SEM, electrons are thermionically emitted from a tungsten or lanthanum hexaboride ( $\text{LaB}_6$ ) cathode and are accelerated towards an anode. Alternatively, electrons can be emitted via field emission. The most common is the Tungsten hairpin gun.

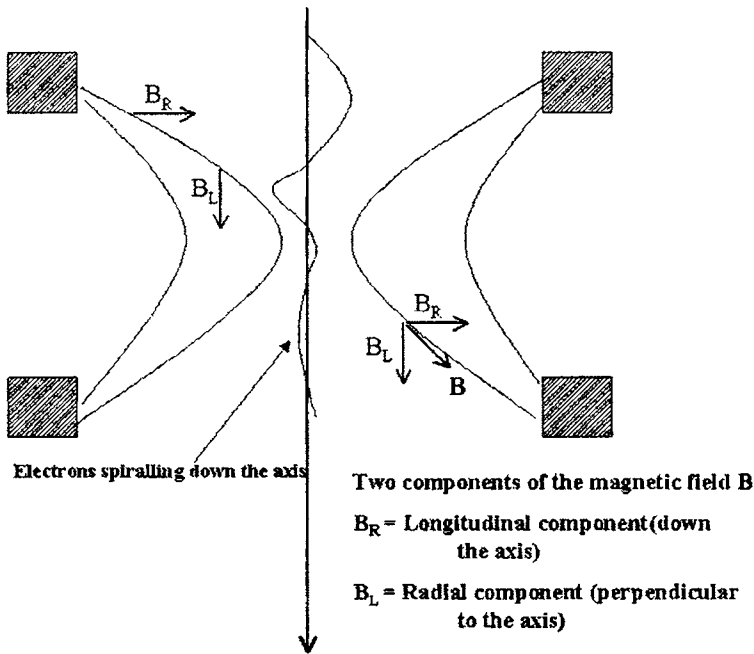


Figure 2.3 The focusing of electrons in SEM

Tungsten is used because it has the highest melting point and lowest vapour pressure of all metals, thereby allowing it to be heated for electron emission. A voltage is applied to the loop, causing it to heat up. The anode, which is positive with respect to the filament, forms powerful attractive forces for electrons. This causes electrons to accelerate toward the anode. The anode is arranged, as an orifice through which electrons would pass down to the column where the sample is held.

The electron beam, which typically has an energy ranging from a few hundred eV to 100 keV, is attracted through the anode and made to pass through a condenser lens, and are focused to very fine point on the sample by the

objective lens (figure 2.3). The electron beam hits the sample, producing secondary electrons from the sample. These electrons are collected by a secondary detector or a backscatter detector, converted to a voltage, and amplified. The amplified voltage is applied to the grid of the CRT that causes the intensity of the spot of light to change. The image consists of thousands of spots of varying intensity on the face of a CRT that correspond to the topography of the sample.

The spatial resolution of the SEM depends on the size of the electron spot, which in turn depends on the electron energy and the magnetic electron-optical system which produces the scanning beam. To ensure that the information recorded in the image arises only from the sample surface, the column must always be at vacuum. Or else, there are chances for contamination of the sample and the electron beam, instead of being directed onto the sample, would induce ionization in any background gas that would effect the measurement being made on the sample. In the present thesis, JEOL JSM 5600 was used for SEM analysis.

### **(b) Atomic force microscope (AFM)**

The atomic force microscope (AFM) is a very high-resolution type of scanning probe microscope, with resolution of fractions of a nanometer, more than 1000 times better than the optical diffraction limit. It can, therefore, probe into understanding the fine details of a sample surface [25]. In atomic force microscopy, a tip, integrated to the end of a spring cantilever, is brought within the interatomic separations of a surface, such that the atoms of the tip and the surface are influenced by interatomic potentials. As the tip is rastered across the surface, it bounces up and down with the contours of the surface.

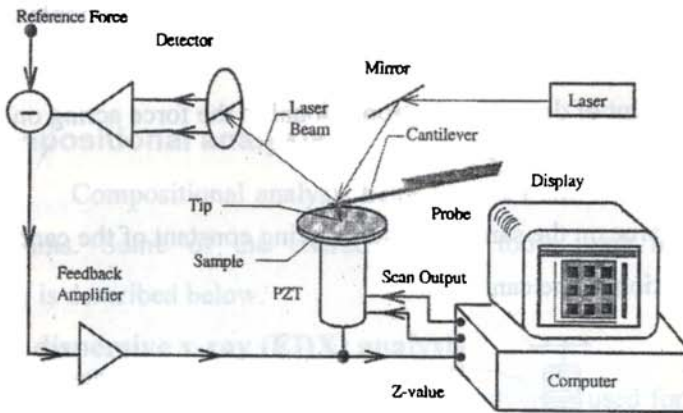


Figure 2.4 The essential elements of an AFM

By measuring the displacement of the tip (*i.e.* the deflection of the cantilever), one can theoretically map out the surface topography with atomic resolution. The AFM is essentially identical in concept to the scanning profilometer, except that the deflection-sensitivity and resolution are improved by several orders of magnitude. The AFM can operate well in ambient air or in a liquid environment making it an important tool in studying biological systems, polymers and a host of insulator and semiconductor materials.

An AFM images a surface in a manner analogous to the gramophone stylus sensing the grooves of gramophone disk. The essential elements of an AFM are shown in the figure 2.4. The tip is attached to a cantilever type spring as shown in the figure 2.5. As the tip and sample interact, forces act on the tip and cause the cantilever (spring) to deflect. The cantilever position is monitored by a position detector. The output of the detector is connected to a feedback controller that regulates the force between the sample and the tip by moving the sample up or down. The sample is moved by a PZT scanning actuator. The

cantilever must be soft enough to deflect a measurable amount without damaging the surface features of the sample.

The amount of deflection is proportional to the force acting on the tip

$$F_{spring} = -k \cdot \Delta Z \quad (2.14)$$

where  $F$  is the force on the sample,  $k$  is the spring constant of the cantilever, and,  $\Delta Z$  is the deflection of the cantilever.

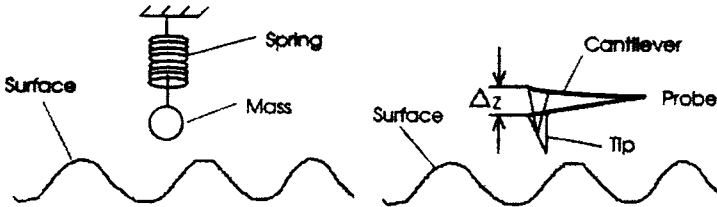


Figure 2.5 Attachment of the tip to the cantilever in an AFM

Two important modes of an AFM are contact mode and the tapping mode. In the contact mode, the static tip deflection is used as the feedback signal. In the tapping mode, the cantilever is externally oscillated at or close to its resonance frequency. The oscillation amplitude, phase and resonance frequency are modified by tip-sample interaction forces; these changes in oscillation with respect to the external reference oscillation provide information about the sample's characteristics.

The AFM provides us with a true three-dimensional surface profile compared to the two-dimensional SEM image, with atomic resolution in ultra high vacuum environments. But an AFM can only image a maximum height of the order of micrometres and a maximum scanning area of around 150 by 150 micrometres whereas SEM can image an area on the order of millimetres by

millimetres with a depth of field of the order of millimetres. In the present work, AFM from Veeco was used morphological study

#### **2.4.4. Compositional analysis**

Compositional analysis helps to check the stoichiometry of the deposited films. Some of the characterization tools used in the present investigation is described below.

##### **(a) Energy dispersive x-ray (EDX) analysis**

Energy dispersive x-ray (EDX) analysis is used for determining the elemental composition of a specimen. It often works as an integrated feature of a SEM, and cannot operate on its own without the latter [24, 25].

During EDX analysis, the specimen is bombarded with an electron beam inside the scanning electron microscope. The bombarding electrons (primary electrons) collide with the specimen, knocking some of them off in the process. The vacancy in the specimen atoms created by the ejection of an inner shell electron is eventually occupied by a higher-energy electron from an outer shell. During this transition, the transferring electron gives up its excess energy in the form of x-rays. The amount of energy released by the transferring electron depends on which shell it is transferring from, as well as which shell it is transferring to. Furthermore, the atom of every element releases x-rays, unique in energy during the transferring process, characteristic of that element. Thus, by measuring the energy of the x-rays emitted by a specimen during electron beam bombardment, the identity of the atom from which the x-ray was emitted can be established. The output of an EDX analysis is an EDX spectrum, which is a plot of how frequently an x-ray is received for each energy level. An EDX spectrum normally displays peaks corresponding to the energy levels for which the most

x-rays had been received. Each of these peaks is unique to an atom, and therefore corresponds to a single element. The higher a peak in a spectrum, the more concentrated the element is in the specimen.

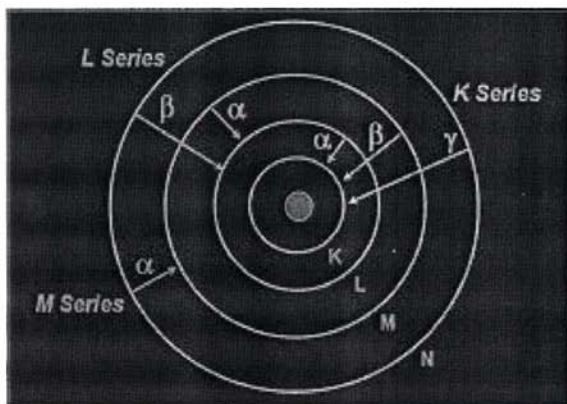


Figure 2.6 Electronic transitions giving rise to x-ray emission

An EDX plot not only identifies the element corresponding to each of its peaks, but the type of x-ray to which it corresponds as well. For example, a peak corresponding to the amount of energy possessed by x-rays emitted by an electron in the L-shell going down to the K-shell is identified as a  $K_{\alpha}$  peak. The peak corresponding to X-rays emitted by M-shell electrons going to the K-shell is identified as a  $K_{\beta}$  peak as shown in figure 2.6.

### (b) X-ray fluorescence (XRF) analysis

X-ray fluorescence (XRF) is another technique used for elemental analysis. Here, a material emits characteristic "secondary" (or fluorescent) x-rays when excited by high-energy x-rays or gamma rays. When materials are exposed

to short-wavelength x-rays or to gamma rays with energy greater than its ionization potential, ionization of their component atoms may take place. X-rays and gamma rays can be energetic enough to expel even the tightly-held electrons from the inner orbitals of the atom. Such a removal of an electron renders the electronic structure of the atom unstable, and electrons in higher orbitals fall into the lower orbital to fill the hole left behind. During this transition, energy is released in the form of a photon, the energy of which is equal to the energy difference of the two orbitals involved. Thus, the material emits radiation, which has energy characteristic of the atoms present. The term fluorescence is applied to the phenomena since absorption of higher-energy radiation results in the re-emission of lower-energy radiation. The intensity of each characteristic radiation is directly related to the amount of the corresponding element in the material.

Rigaku x-ray fluorimeter was used in the present study.

## **2.4.5. Optical studies**

### **(a) Determination of band gap energy**

#### **i) Transmission spectroscopy**

Intrinsic optical absorption of a single photon across the band gap is the dominant optical absorption process in a semiconductor. When the energy of the incident photon ( $h\nu$ ) is larger than the band gap energy the excitation of electrons from the valence band to the empty states of the conduction band occurs. The light passing through the material is then absorbed and the number of electron hole pairs generated depends on the number of incident photons  $S_0(\nu)$  (per unit area, unit time and unit energy). The photon flux  $S(x,\nu)$  decreases exponentially inside the crystal according to the relation [22],

$$S(x, \nu) = S_0(\nu)\exp(-\alpha x) \quad (2.15)$$

where, the absorption coefficient  $\alpha$ , ( $\alpha(\nu) = 4\pi k\nu/c$ ) is determined by the absorption process in semiconductors and  $k$  is the extinction coefficient.

For the parabolic band structure, the relation between the absorption coefficient ( $\alpha$ ) and the band gap of the material is given by [26],

$$\alpha = \frac{A}{h\nu} (h\nu - E_g)^r \quad (2.16)$$

where,  $r = 1/2$  for allowed direct transitions,  $r = 2$  for allowed indirect transitions,  $r = 3$  for forbidden indirect transitions and  $r = 3/2$  for forbidden direct transitions.  $A$  is the parameter which depends on the transition probability. The absorption coefficient can be deduced from the absorption or transmission spectra using the relation,

$$I = I_0 e^{-\alpha t} \quad (2.17)$$

where,  $I$  is the transmitted intensity and  $I_0$  is the incident intensity of the light and  $t$  is the thickness of the film. In the case of direct transition,  $(\alpha h\nu)^2$  will show a linear dependence on the photon energy ( $h\nu$ ). A plot of  $(\alpha h\nu)^2$  against  $h\nu$  will be a straight line and the intercept on energy axis at  $(\alpha h\nu)^2$  equal to zero will give the band gap energy.

The transmissions of the thin films were recorded using Jasco V570 spectrophotometer in the present studies.

## ii) Diffuse reflectance spectroscopy (DRS)

Diffuse reflection is the reflection of light from an uneven or granular surface such that an incident ray is seemingly reflected at a number of angles. Diffuse reflected rays from a sample do not obey the Snell's law as do the

ordinary mirror-like specular reflections. The measurement of radiation diffusely reflected from a surface constitutes the area of spectroscopy known as diffuse reflectance spectroscopy (DRS). Specular reflection is due to the reflection at the surface of single crystallites while diffuse reflection arises from the radiation penetrating into the interior of the solid and re-emerging to the surface after being scattered numerous times. Thus, the DRS spectra can exhibit both absorbance and reflectance features due to contributions from transmission, internal and specular reflectance components as well as scattering phenomena in the collected radiation.

Based on the optical properties of the sample, several models have been proposed to describe the diffuse reflectance phenomena. The Kubelka-Munk (KM) model put forward in 1931 [27] is widely used and accepted in DRS. The KM theory is based on a continuum model where reflectance properties are described by differential equations for infinitesimally small layers. When the depth of the sample is infinite, the theory is solved to arrive at the remission function or the so-called KM function,

$$f(r_{\infty}) = \frac{(1 - r_{\infty})^2}{2r_{\infty}} = \frac{k}{s} \quad (2.18)$$

where,  $r_{\infty} = R_{\infty}(\text{sample})/R_{\infty}(\text{standard})$ ,  $R_{\infty}$  denotes the diffuse reflectance. Here the standard used is  $\text{BaSO}_4$ .  $R_{\infty}(\text{standard})$  is taken as unity. The intensity of the diffusely reflected light therefore depends on the scattering coefficient  $s$  and the absorption coefficient  $k$ . The band gap is estimated from the plot of  $\{(k/s).h\nu\}^2$  vs.  $h\nu$  ( $h\nu$  is the photon energy) by extrapolating the graph to the  $x$  axis.

DRS was carried out using JASCO V 500 spectrophotometer in the present studies.

### **(b) Photoluminescence (PL)**

Photoluminescence (PL) is the emission of light when a substance is irradiated with a shorter-wavelength light. Photoluminescence spectroscopy is a contactless, nondestructive method of probing the electronic structure of materials. Here, light is directed onto a sample, where it is absorbed and imparts excess energy into the material in a process called photo-excitation. One way this excess energy can be dissipated by the sample is through the emission of light, or luminescence. The intensity and spectral content of this luminous output is a direct measure of various important material properties. In PL, the incident photons are absorbed by the luminescent impurity centers, which are either excited into a higher energy state or lose an electron to the conduction band, depending on the system under study. The excess energy above that needed for the transition is lost as heat to the lattice almost immediately. The light which is emitted when the excited electron make transitions back to its ground state or the ionized electron recombines is monitored by a photometer or by a combination of a monochromator and PMT or photodiode to generate the spectrum. In the latter case, the wavelength selected by the monochromator is swept across the visible spectrum and intensity at each wavelength is recorded as a point on the spectrum. Note that more than one transition may be present in the sample. In this case, the ratio of actual transitions may be a function of temperature, incident wavelength, and incident light intensity. A second PL spectrum is the absorption spectrum which is often called photoluminescent excitation (PLE) spectrum. In this case, a single

emission wavelength is selected, for instance the peak emission from the luminescent impurity, and the intensity of that emission is recorded as a function of the input wavelength. In this manner, each transition which gives rise to a peak on the emission spectrum may have its own unique absorption spectrum.

Quantum mechanically, photo-excitation causes electrons within the material to move into permissible excited states. When these electrons return to their equilibrium states, the excess energy is released radiatively or non-radiatively. The radiative emission on photo-excitation is what one refers to as photoluminescence. The energy of the emitted light relates to the difference in energy levels between the two electron states involved in the transition between the excited state and the equilibrium state. The quantity of the emitted light is related to the relative contribution of the radiative process.

Radiative transitions in semiconductors also involve localized defect levels. The photoluminescence energy associated with these levels can be used to identify specific defects, and the amount of photoluminescence can be used to determine their concentration.

PL is divided into two major types: Intrinsic and extrinsic depending on the nature of electronic transition producing it.

### **i) Intrinsic luminescence**

There are three kinds of intrinsic: 1) band-to-band luminescence  
2) exciton luminescence 3) cross-luminescence.

#### **1) Band –to –band luminescence:**

Luminescence owing to band-to-band transition, ie. to the recombination of an electron in the conduction band with a hole in the valance band, can be

seen in pure crystal at relatively high temperature. This has been observed in Si, Ge and IIIb-Vb compounds such as GaAs.

### **2) Exciton luminescence:**

An exciton is a composite particle of an excited electron and a hole interacting with one another. It moves in a crystal conveying energy and produces luminescence owing to the recombination of the electron and the hole. There are two kinds of excitons: Wannier exciton and Frenkel exciton.

The Wannier exciton model express an exciton composed of an electron in the conduction band and a hole in the valence band bound together by coulomb interaction. The expanse of the wave function of the electron and hole in Wannier exciton is much larger than the lattice constant. The excitons in IIIb-Vb and IIb-VIb compounds are examples for Wannier exciton. The Frenkel exciton model is used in cases where expanse of electron and hole wave function is smaller than lattice constant. The excitons in organic molecular crystals are examples of Frenkel exciton.

### **3) Cross luminescence**

Cross luminescence is produced by the recombination of an electron in the valance band with a hole created in the outer most core band. This is observed in number of alkali and alkaline-earth halides and double halides. This takes place only when the energy difference between the top of valance band and that of conduction band is smaller than the band gap energy. This type of luminescence was first observed in BaF<sub>2</sub>.

### **ii) Extrinsic luminescence**

Luminescence caused by intentionally incorporated impurities, mostly metallic impurities or defects is classified as extrinsic luminescence.

Most of the observed type of luminescence of practical application belongs to this category. Intentionally incorporated impurities are activators and materials made luminescent in this way are called phosphors. Extrinsic luminescence in ionic crystals and semiconductors is classified into two types: unlocalized and localized. In the unlocalized type, the electrons and holes of the host lattice participate in the luminescence process, while in localized type the luminescence excitation and emission process are confined in a localized luminescence center.

### **1) Unlocalised type**

In semiconductors donors and acceptors act as luminescence activators. There are two types of luminescence transitions i.e. the transition of a free carrier to a bound carrier and the transition of a bound electron at a donor to a bound hole at an acceptor. These kinds of luminescence lines and bands are usually observed in compound semiconductors such as IIIb-Vb and IIB-VIb compounds.

### **2) Localised type**

Various kinds of metallic impurities intentionally incorporated in ionic crystals and semiconductors create efficient localized luminescence centres. Localized type centres are classified into allowed and forbidden transition type in terms of electric dipole transitions. The electric dipole transition can take place between energy levels only with different parities i.e.  $\Delta l = \pm 1$ . When atoms and ions are incorporated in crystals, the forbidden character of the dipole transition is altered by the perturbation of the crystal electric field, so that the forbidden transition becomes allowed to some degree. Many phosphors that are important from a practical viewpoint are synthesized by incorporating following activators.

**a) Allowed transition type:**

- (i)  $s \leftrightarrow p$  transition - F centre  $\leftrightarrow$  ( an electron trapped at an anion vacancy)
- (ii)  $s^2 \leftrightarrow sp$  transition  $Tl^+$ ,  $Sn^{2+}$ ,  $Pb^{2+}$ ,  $Sb^{3+}$ ,  $Bi^{3+}$
- (iii)  $f \leftrightarrow d$  transition  $Eu^{2+}$ ,  $Ce^{3+}$

**b) Forbidden transition type:**

- (i)  $d \leftrightarrow d$  transition  $Ti^{3+}$ ,  $Cr^{3+}$ ,  $Cr^{2+}$ ,  $Mn^{4+}$ ,  $Mn^{2+}$ ,  $Fe^{3+}$ ,  $Fe^{2+}$
- (ii)  $f \leftrightarrow f$  transition -  $Pr^{3+}$ ,  $Nd^{3+}$ ,  $Sm^{3+}$ ,  $Eu^{3+}$ ,  $Tb^{3+}$ ,  $Tm^{3+}$ ,  $Dy^{3+}$  ( and other trivalent rare earth ions)

Iron group ions show luminescence owing to the  $3d^n \leftrightarrow 3d^n$  ( $n = 2 - 8$ ) transition in the visible to infrared region. Among them,  $Cr^{3+}$  and  $Mn^{4+}$  ions with the  $3d^3$  configuration and the  $Mn^{2+}$  ion with the  $3d^5$  configuration are important for phosphor application. The luminescence spectra of  $Mn^{2+}$  are always bands, which vary from blue to red [29].

Two types of luminescence spectra can be distinguished: excitation and emission. The excitation spectrum gives the intensity variations of the exciting radiation over a range for a fixed emission wavelength. It gives information on the position of excited states just as the absorption spectrum does, except that the former reveals only the absorption bands that result in the emission of light. The observed differences between the absorption and excitation spectra can yield useful information. An emission spectrum provides information on the spectral distribution of the light emitted by a sample for a given excitation wavelength. The time resolved PL measurements are a powerful tool for the determination of the radiative efficiency that specifies the fraction of excited states which de-excite by emitting photons. [23, 29].

The emission and excitation spectra for the powder and thin film samples are recorded using Fluoromax - 3 spectrofluorometer consisting of 150W xenon arc lamp, monochromator and a PMT detector. A continuous source of light shines on to an excitation monochromator, which selects a band of wavelengths. This monochromatic excitation light is directed onto a sample, which emits luminescence. The luminescence is directed into a second emission monochromator which selects a band of wavelengths and shines them onto a PMT (R928P PMT) ranging from 180 - 850 nm. The reference detector monitoring the xenon lamp - a UV enhanced Si photodiode - requires no external bias and has good response from 190-980 nm. The signal from the detector is reported to a system controller and host computer where the data can be manipulated and presented using special software.

### **2.4.6 Electro Optic Characterization**

The three main quantities of an ACTFEL device that describes the optical emission are (1) Luminance, (2) efficiency and (3) Color. Generally in SI units, luminance is expressed in  $\text{Cd/m}^2$  and efficiency in  $\text{lm/W}$ . The color is normally expressed as two colour coordinates, (x, y). These are the features of an ACTFEL device that industry people are interested in.

#### **(a) Luminance-Voltage characterization**

##### **(L-V characteristics)**

The universal measurement performed on ACTFEL device is luminance-voltage (L-V) measurement. Here we apply waveforms of steadily increasing amplitudes to a device and will measure the luminance at each

successive amplitude. Usually luminance is measured with a photometer, photomultiplier tube (PMT), CCD or a photodiode.

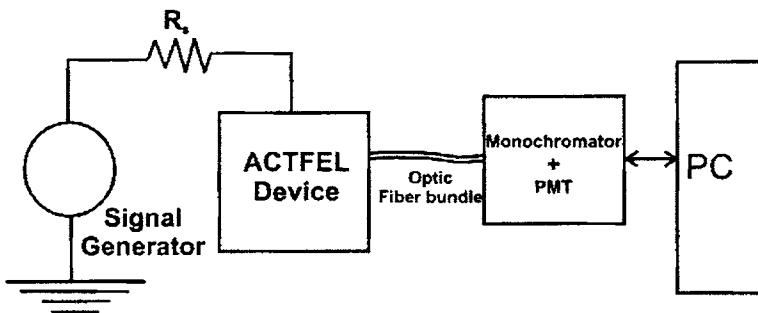


Figure 2.7 Experimental set up for Luminance measurements

This measurement reports the luminous intensity output in a direction normal to the emitting surface. The data is collected at successive higher voltage amplitudes until a predetermined stopping voltage. Once the data is collected, the L-V curve is plotted by taking voltage along x-axis and luminance along y axis. Typical L-V curve is shown in the figure 2.7.

As shown in the figure, at higher applied voltages the L-V curve saturates and may eventually decrease again. This could be due to two factors. (1) as higher fraction of luminescent centers are impact excited, there is a less probability for an additional injected electrons will cause an impact excitation event. (2) Increased device heating leads to non-radiative decay paths which compete with the desired radiative path and cooling of the electron distribution because of increased lattice scattering. Usually luminance value at a certain voltage above threshold, typically 40 V above threshold (L40), is reported, since different phosphor behave differently. The 40V above threshold is chosen

because maximum luminance efficiency is observed in 30-40 V above threshold regime. Moreover, different wave forms as well as drive frequency results in different luminance value, while reporting luminance of a phosphor, drive frequency and waveform with pulse width, rise time and fall time of the pulse and phosphor layer thickness is presented together with luminance value.

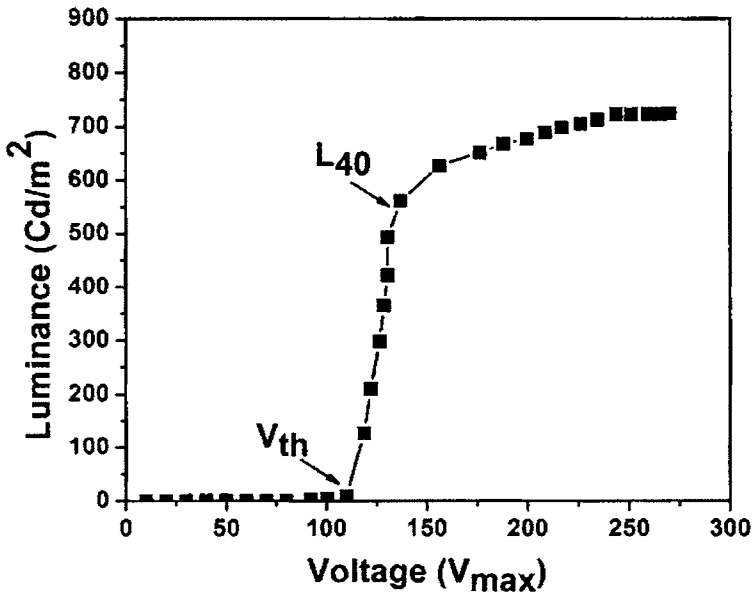


Figure 2.7 Typical L-V curve of an ACTFEL device for a drive frequency 1 KHz

Since different photometers respond differently to different wavelengths, in order to get absolute luminance, the spectrum analyzing instrument should be calibrated with a source of known luminance. This calibration lamp must be NIST traceable for re-calibration after certain hours of use. In the present study we had used non-calibrated PMT for recording the spectra.

### **(b) Efficiency-Voltage characterization**

Efficiency of an ACTFEL device corresponds to how much of the input electrical energy is converted to light output. The idea is a dim but efficient phosphor may be carefully designed to increase its brightness, but an inefficient phosphor may not be useful to produce cool head-mounted displays with long battery lives. The luminance efficiency is given by

$$\eta = \pi(L/P) \quad (2.19)$$

Where  $L$  is the luminance output at a particular voltage in  $\text{Cd/m}^2$  and  $P$  is the power dissipated in Watts for that particular applied voltage. The  $\pi$  factor accounts for the emission of light from the assumed diffuse surface of the ACTFEL device in all directions, not just the normal direction actually measured. Efficiency values are reported as in a same fashion as luminance values. Usually efficiency at 40 V above threshold ( $\eta_{40}$ ) is reported.

### **(c) Color and chromaticity coordinates**

The color of the ACTFEL device is also an important parameter that should also be quantified. While spectra provide information about fundamental physical operation of the device, chromaticity coordinates specify the precise color of the emission. Cone cells or cones are photoreceptor cells in the retina of the eye which function best in relatively bright light. Humans normally have three kinds of cones. The first responds most to light of long wavelengths, peaking in the yellow region, designated as  $L$  for long. The second type responds most to light of medium-wavelength, peaking at green ( $M$  for medium). The third type responds most to short-wavelength light, of a violet color ( $S$  for short). These three have peak wavelengths near 564 – 580 nm 534 –

545 nm, and 420 – 440 nm, respectively. The difference in the signals received from the three types of cone allows the brain to perceive all possible colors, through the opponent process of color vision.

A spectrum is a plot of emission intensity against the wavelength of the detected light. Spectra are separated by the source of the input energy used to stimulate the light output. If the source of excitation is light, the emission spectrum is called photoluminescent spectra while electric excitation gives electroluminescent spectra. An EL spectrum is taken in an identical manner as the PL emission spectrum except that the device is excited in the normal manner by voltage pulses. The EL spectrum is often identical to the PL spectrum, although often some differences are apparent. For instance, a transition may appear in a PL spectrum but not in an EL spectrum if the photons are energetic enough to cause the transition but the injected electrons are not. Furthermore, the intensity of the PL response usually is indicative of the EL response. PL characterization of phosphor powders is therefore undertaken before the costly and time-consuming process of creating an ACTFEL device incorporating the phosphor in an effort to optimize dopant concentrations or evaluate whether a phosphor is even worth pursuing for ACTFEL applications. Care must be exercised, though: the most bright and efficient ACTFEL phosphor known, ZnS:Mn, exhibits very poor PL emission. Energy transfer from the lattice to the  $Mn^{2+}$  is poor while the  $Mn^{2+}$  ion is excited directly by hot electron impingement during ACTFEL device operation.

There could be multiple emissions from a phosphor, in a wide range of wavelength region. There for the over all color of the emission should be computed from an emission spectrum. The most commonly used standard was

created in 1931 and is called Commission Internationale del'Eclairage, known as CIE coordinates, which maps all the visible color space to a two-dimensional map as x and y coordinates. These values are given by

$$x = X/X+Y+Z \quad (2.20)$$

$$y = Y/X+Y+Z \quad (2.21)$$

$$z = Z/X+Y+Z \quad (2.22)$$

where X, Y and Z are called CIE tristimulus values. These values are found by integrating the product of the measured spectrum  $P(\lambda)$  and special CIE spectral stimulus functions  $x_\lambda(\lambda)$ ,  $y_\lambda(\lambda)$  and  $z_\lambda(\lambda)$  over the visible spectrum. This is computed as

$$X = \int_{\lambda=380nm}^{780} x_\lambda(\lambda)P(\lambda)\Delta\lambda \quad (2.23)$$

$$Y = \int_{\lambda=380nm}^{780} y_\lambda(\lambda)P(\lambda)\Delta\lambda \quad ((2.24)$$

$$Z = \int_{\lambda=380nm}^{780} z_\lambda(\lambda)P(\lambda)\Delta\lambda \quad (2.25)$$

Where  $\Delta\lambda$  is the spacing or steps of the acquire points. Normally it will be 1 nm or 10 nm. These stimulus functions are experimentally determined through trials in which many people are asked to match colors by adjusting the intensities of primary colors (see figure 2.8). Thus the stimulus functions represent the reaction of a standard observer.

The 1931 CIE chromaticity diagram is shown in figure 2.9. Points on the locus of horse-shoed shaped plot correspond to monochromatic light sources. The coordinates of white are CIE  $x,y = 0.333, 0.333$ . For any other color, ie a

point C, the dominant wavelength is found approximately by drawing a line from white (W) to perimeter of locus through C.

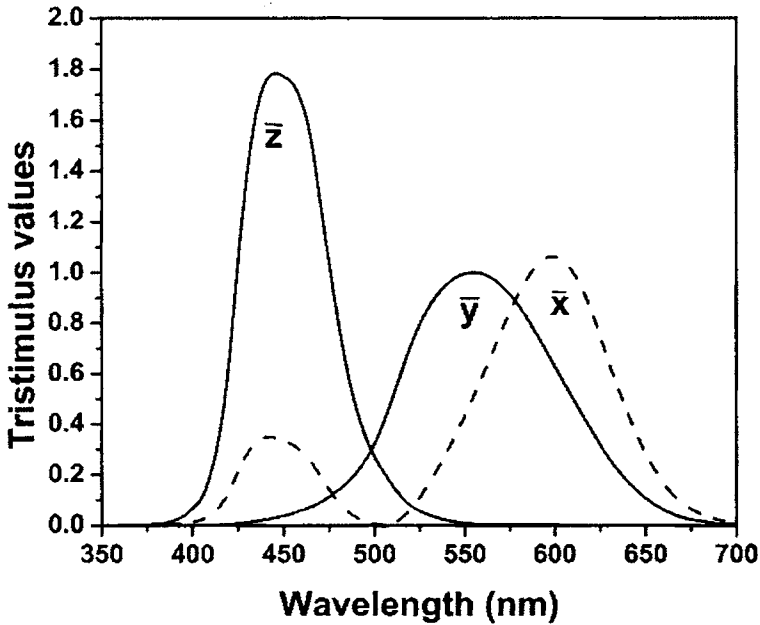


Figure 2.8 The CIE color matching functions

The dominant wavelength corresponds to that point at which the line meets the perimeter. It should be noted that CIE chromaticity diagrams are not intended to portray actual colors. Indeed, this is not even possible considering that any real display system is incapable of accurately displaying the entire gamut of color contained in the diagram.

The utility of this technique is that two light sources with identical CIE coordinates are known to appear the same color to a standard observer, even though spectra may be very different. Moreover if we have a multi color multi phosphor display system and if we plot CIE coordinates of individual phosphor

on the diagram and the polygon connecting the coordinates defines all the colors which can be created using these phosphors. For example, for a phosphor system emitting in red and green region, find the coordinates of the individual phosphors and plot on CIE diagram.

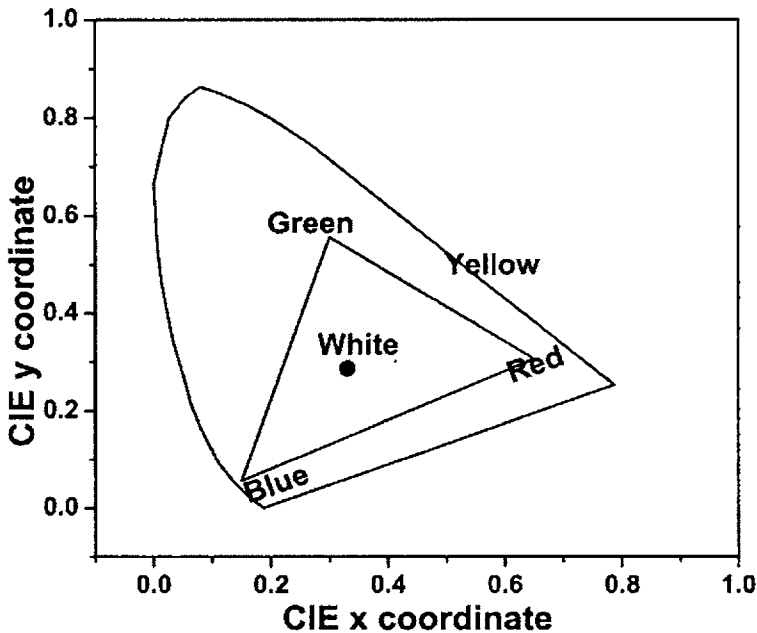


Figure 2.9 The CIE coordinate diagram

Connect two points via a straight line, and then the system can reproduce any color along the line. For the three phosphors the diagram is a triangle and any color in the area of triangle can be reproduced by the system. In the figure a triangle has been plotted which is called phosphor triangle of a color CRT. The area of phosphor triangle defines the colors that can be reproduced by a CRT.

However the 1931 CIE formulation does have some draw backs. The color matching functions represent a standard observer. Obviously some variation in human vision exists from one to another. Also the distance between two points in the CIE diagrams does not represent the perceived difference between two colors. This limitation is addressed in another color space diagram called CIELUV.

### 2.4.7 Electrical Characterization

Much useful information about ACTFEL devices can be obtained by studying the electrical behaviour. The experimental set up- so called Sawyer Tower circuit is shown in the figure 2.10. Here the device is connected in series with a sense element (usually a capacitor),  $C_s$  and a series resistance  $R_s$ . A waveform generator provides a voltage signal to the device while an oscilloscope (Tektronix TDS 2014) monitors voltage across device and sense capacitor  $C_s$ . The role of  $R_s$  is to limit the current through the device and protect it from high current short circuits.

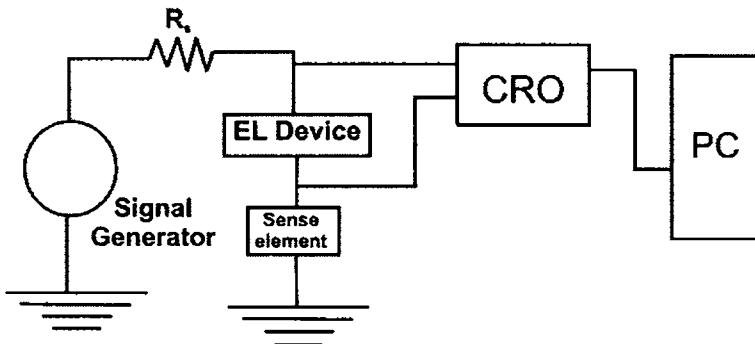


Figure 2.10 The Sawyer-Tower circuit for electrical characterization

The voltage measured across  $C_s$  will give information about total charge that is transferred across the device. Normally  $C_s$  is chosen to be very large so that most of the applied voltage is dropped across the device itself.

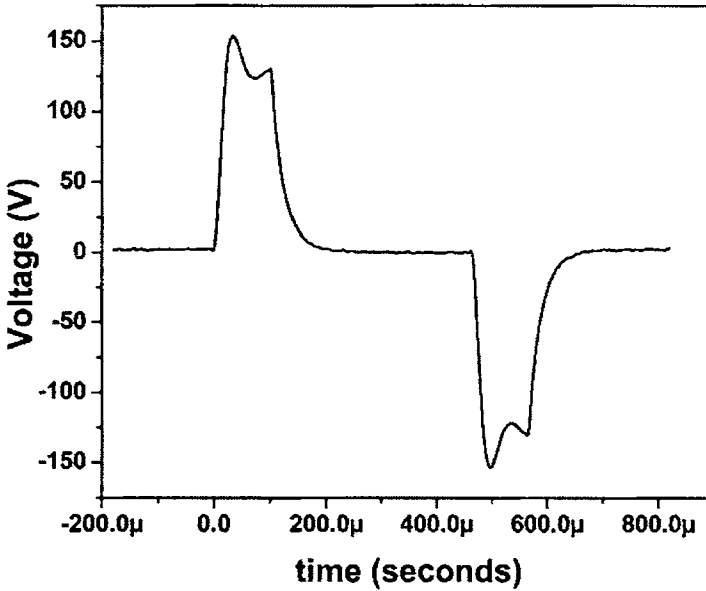


Figure 2.11 Wave form used in the present study

Most researchers employ a sine wave or bipolar trapezoidal waveform to characterize ACTFEL device. In this study we have used bipolar trapezoidal waveform (Digilog Instruments Pvt, Bangalore). The shape of the wave form is as shown in the figure 2.11.

The rise time ( $\tau_r$ ) is  $30\mu\text{s}$ , stay ( $\tau_s$ ) and trail ( $\tau_t$ ) time is  $70\mu\text{s}$  which was quite large when compared to standard values ( $\tau_r = 5\mu\text{s}$ ,  $\tau_s = 30\mu\text{s}$  and  $\tau_t = 5\mu\text{s}$ ).

## External Charge-Voltage characterization

The measurement external charge versus voltage is a standard electrical characterization technique. The charge on the external terminals of the ACTFEL device is plotted against applied voltage to the device forming a hysteretic loop. This external charge is measured using the sense capacitor using the relation  $q_{\text{ext}} = V_s * C_s$ . This charge is normalized to the area of the device. A Q-V plot is always hysteretic when dissipative charge conduction in an ACTFEL device is occurring and hence it is a straight line with slope equal to  $C_t$  when an ACTFEL device is driven below threshold. Therefore the threshold voltage of an ACTFEL device is the voltage at which the Q-V curve initially becomes hysteretic.

A Q-V plot of a typical ZnS:Mn device is shown in figure 2.12 to illustrate some of the information that is available from a Q-V plot [31]. The voltage labeled  $V_{to}$  in figure is termed the negative turn-on voltage whereas the analogous voltage during the positive portion of the waveform is known as the positive turn-on voltage  $V_{to}$ . A distinction is made between these two voltages because they are not in general of equal magnitude although they are normally very close to the same magnitude. The turn on voltage differs from the threshold voltage due to the polarization charge  $Q_{\text{pol}}^e$  in figure 2.12. Polarization charge is a measure of the charge imbalance across the phosphor layer of an ACTFEL device following the conclusion of an applied voltage pulse.

The  $e$  superscript indicates that polarization charge as measured in a Q-V plot is a purely external quantity that must be transformed by  $E_q$  to give a measure of the internal phosphor polarization. The polarization charge existing after the conclusion of a pulse always aids the following pulse of opposite

polarity because both result in electric fields of the same polarity. In fact the threshold voltage  $V_{th}$  may be defined as

$$V_{th} = \lim_{Q_{pol} \rightarrow 0} V_{to}(Q_{pol}) \quad (2.26)$$

One of the factors that can significantly reduce polarization charge, is the amount of leakage charge denoted  $Q_{leak}^e$  in figure. The leakage charge is a measure of the amount of charge movement that takes place due to polarization fields during the inter-pulse intervals segments EF and JA in figure 2.12. The leakage charge as measured by a Q-V is also a purely external quantity as denoted by the  $e$  superscript and must also be transformed via  $E_q$  to get a measure of actual charge movement through the phosphor layer.

The remaining charge terms in figure 2.12 are the charge terms that relates to the on time of the ACTFEL device. First the conduction charge labeled  $Q_{cond}$  in figure 2.12 is the amount of charge conducted through the phosphor layer of the device from device turn-on until the falling edge of the pulse segments BD and GI in the figure 2.12. The conduction charge as measured by the Q-V directly corresponds to the internal phosphor conduction charge so no  $e$  superscript is necessary. Next the term  $Q_{relax}$  is termed the relaxation charge and this is a measure of the charge that flows during the portion of the waveform where the applied voltage is constant at its maximum value segments CD and HI in figure 2.12. This charge is termed relaxation charge because the flow of this charge gives rise to a field opposite to the applied phosphor field and since the applied voltage is no longer slewing the magnitude of the phosphor field tends to decrease or relax during this portion of the waveform. Finally the charge labeled  $Q_{max}^e$  in figure is termed the maximum charge and corresponds to the maximum

voltage measured across the sense capacitor for a given applied voltage. Note that  $Q_{\max}$  is taken with respect to a charge zero reference point the external charge axis.

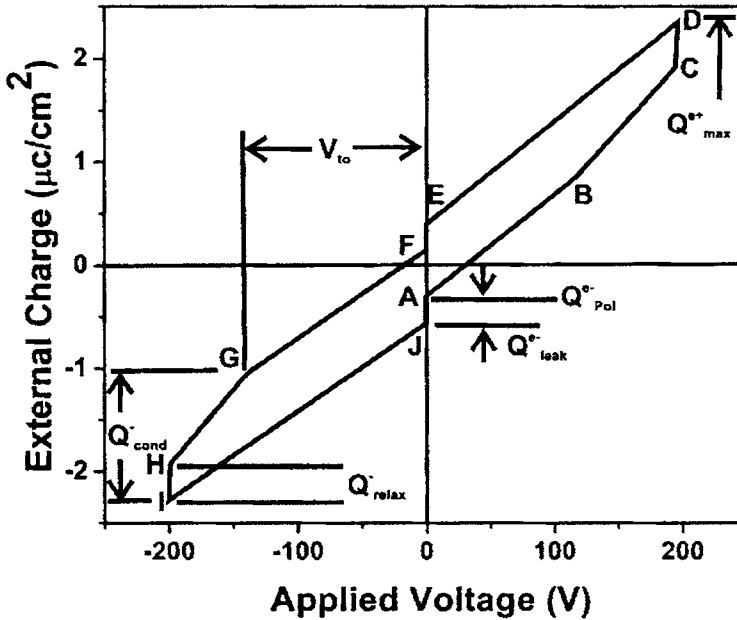


Figure 2.12 Typical Q-V diagram of an ACTFEL device

Thus  $Q_{\max}$  differs from all of the other Q-V charges since all of the other charges represent differences in the voltage across the sense capacitor at two distinct points of the applied voltage waveform. As seen in a later section  $Q_{\max}$  is a useful quantity for performing transferred charge measurements. It should also be noted that each of the charges discussed above are labeled for only one polarity of the driving waveform in figure but they exist for both polarities hence the and superscripts. The Q-V curve is used to assess several important physical parameters about ACTFEL devices. First below the turn-on voltage of the

ACTFEL device it behaves as a simple capacitor with the capacitance given by the series combination of the insulator and phosphor capacitances. Since the slope of a Q-V plot is a capacitance the Q-V slope below turn-on region (AB and FG segments) yields the total device capacitance  $C_t$ . Next if the phosphor layer is assumed to be shorted during the post turn-on portion of the driving waveform (segments BC and GH in figure 2.12) the slope of the Q-V curve in this region corresponds to the insulator capacitance of the ACTFEL device  $C_i$ . This should be approached with some caution, however because if there is space charge generation during this time the slope of the Q-V can become much greater than the physical insulator capacitance. On the other hand, sometimes the phosphor layer may be incompletely shunted and the slope of the Q-V may be much less than the physical insulator capacitance. Finally the area enclosed within a Q-V curve is equal to the input electrical power density delivered to the ACTFEL device per pulse.

## References

1. J. George, *Preparation of Thin Films*, p.1, Marcel Dekker Inc., New York (1992)
2. T. Sei, Y. Nomura and T. Tsuchiya, *J. Non-Cryst. Solids*, **218**, 135 (1997)
3. Z. Ji, L. Kun, S. Yongliang and Y. Zhizhen, *J. Cryst. Growth*, **255**, 353 (2003)
4. Z. Yan, M. Koike and H. Takei, *J. Cryst. Growth*, **165**, 183 (1996)
5. S. H. Yang, *J. Electrochem. Soc.*, **150**, H250 (2003)
6. Z. Lou and J. Hao, *Appl. Phys. A*, **80**, 151 (2005)
7. J. Hao, Z. Lou, I. Renaud and M. Cocivera, *Thin Solid Films*, **467**, 182 (2004)

8. T. Miyata, T. Nakatani and T. Minami, *Thin Solid Films*, **373**, 145 (2000)
9. N. Honda, T. Suzuki, T. Yunogami, H. Suematsu, W. Jiang and K. Yatsui, *Jpn. J. Appl. Phys.*, **44**, 695 (2005)
10. T. Minami, Y. Kuroi and S. Dakata, *J. Vac. Sci. Technol. A*, **14**, 1736 (1996)
11. L. I. Maissel and R. Glang, *Handbook of Thin Film Technology*, p.22, McGraw-Hill, New York (1970)
12. L. Holland, *Vacuum Deposition of Thin films*, p.104, John Wiley & Sons Inc., New York, 1956
13. W. D. Gill and E. Kay, *Rev. Sci. Instrum.* **36**, 277 (1965)
14. I. G. Kesaer and V. V. Pashkoba, *Sov. Phys. Tech. Phys.* **4**, 254 (1959)
15. S. Hayakawa and K. Wasa, *J. Phys. Soc. Jpn.* **20**, 1692 (1965)
16. R. McMahan, J. Affinito, and R. R. Parsons, *J. Vac. Sci. Technol.* **20**, 376 (1982)
17. V. S. Smentkowski, *Progress in Surface Science*, **64**, 1 (2000)
18. R. Venkatesan and S. M. Green; *The industrial physicist*, 22 (1996)
19. D. B. Chrisey and G. K. Hubler, *Pulsed Laser Deposition of Thin Films*, p.229, John Wiley and sons Inc., New York, 1994
20. T. Minami, T. Nakatani and T. Miyata, *J. Vac. Sci. Technol. A*, **18**, 1234 (2000)
21. T. Minami, T. Shirai, T. Nakatani and T. Miyata, *Jpn. J. Appl. Phys.*, **39**, L524 (2000)
22. Veeco Dektak 6M Manual (2004)
23. B.D. Cullity and S.R. Stock, *Elements of X ray diffraction*, Third edition, Prentice Hall, New Jersey (2001)

24. Charles Kittel, *Introduction to Solid State Physics*, Seventh edition, Wiley Eastern Limited, New Delhi (1996)
25. D. K. Schroder *Semiconductor material and device characterization*, second edition, p.651, John Wiley & Sons Inc., New York (1998)
26. P. E. J. Flewit and R. K. Wild, *Physical methods for material characterization*, Second edition, p.501, IOP publishing, London (2003)
27. P. Kubelka and F. Munk, *Zh. Tekh. Fiz.*, **12**, 593 (1931)
28. P. Kubelka, *J. Opt. Soc .Am.*, **38**, 448 (1948)
29. D. R. Vij (Ed.) *Luminescence of solids*, p.46, Plenum Press, New York (1998)
30. P. A. Keller, *Information Display*, **12**, 36 ( 1996)
31. P. D. Keir and J. F. Wager, *Ann. Rev. Mater. Sci.*, **27**, 223 (1999)

## **CHAPTER 3**

---

# **Synthesis and Characterization of Oxide Phosphors**

---

*This chapter is divided in to two parts. Part A deals with synthesis and characterization of bulk  $Zn_2GeO_4:Mn^{2+}$  phosphor and the effect of Mg addition on structural and optical properties are discussed. On the basis of analysis the presence of a sub-band gap is observed and possible mechanism of luminescence in the phosphor is identified.*

*Part B discusses about synthesis and characterization of bulk  $Mg_2GeO_4:Mn$  phosphor and the effect of Zn codoping on structural and optical properties. Zn codoping is found to increase photoluminescent (PL) emission intensity. •*

## **PART A**

---

# **Synthesis and characterization of $\text{Zn}_2\text{GeO}_4: \text{Mn}^{2+}$ phosphor**

---

### **3A.1. Introduction**

Thin film electroluminescent devices are mostly based on sulphide phosphors (ZnS, SrS etc) [1-4]. Recently, oxide phosphors [5, 6] are considered as potential substitutes owing to their extreme stability in vacuum, moisture insensitivity and non-degradation under electron bombardment. Several oxide phosphor hosts like ZnGa<sub>2</sub>O<sub>4</sub>, Zn<sub>2</sub>GeO<sub>4</sub>, Zn<sub>2</sub>SiO<sub>4</sub>, Y<sub>2</sub>O<sub>3</sub> etc have been extensively studied [7-13]. Among them, Zn<sub>2</sub>GeO<sub>4</sub> doped with Mn is an excellent green emitting phosphor. Rhombohedral Zn<sub>2</sub>GeO<sub>4</sub> is similar to Zn<sub>2</sub>SiO<sub>4</sub>, but have lower crystallization temperature. Thin films of Zn<sub>2</sub>GeO<sub>4</sub>:Mn<sup>2+</sup> grown using RF magnetron sputtering and pulsed laser deposition techniques also show good luminescent characteristics [13-15]. The green emission in Zn<sub>2</sub>GeO<sub>4</sub>:Mn<sup>2+</sup> is due to the transitions in 3d<sup>5</sup> electrons of Mn<sup>2+</sup> that substitute tetrahedral Zn<sup>2+</sup> sites [13]. Several methods can be adopted to enhance the luminescent properties of these phosphors. Co-doping is one such efficient approach. In Zn<sub>2</sub>GeO<sub>4</sub>, co-dopants that substitute Ge<sup>4+</sup> and Zn<sup>2+</sup> can provide positive results. Among the various ions (Mg<sup>2+</sup>, Cd<sup>2+</sup>, Ba<sup>2+</sup> etc.) that can replace Zn<sup>2+</sup> in Zn<sub>2</sub>GeO<sub>4</sub>, Mg<sup>2+</sup> is a better choice since its ionic radius is more comparable with Zn<sup>2+</sup> than other ions. In the present work, the effect of Mg<sup>2+</sup> incorporation on structural and luminescent properties of Zn<sub>2</sub>GeO<sub>4</sub>:Mn is studied in detail.

### **3A.2. Experiment**

The samples were prepared by conventional high temperature solid-state reaction of constituent oxides namely ZnO (Alfa Aesar 99.99%), MgO (Alfa Aesar 99.99%) GeO<sub>2</sub>. (Alfa Aesar 99.999%) Manganese was added in the form of manganous acetate [Mn(CH<sub>3</sub>COO)<sub>2</sub>]. The powders were mixed

stoichiometrically in ethanol medium and calcined in air at 1200°C for 12 hrs in a tube furnace to obtain  $Zn_{1.96-1.96x}Mg_{1.96x}GeO_4:Mn_{0.04}$  (x was varied from 0 to 0.5). All samples were doped with 2 at.% of Mn which was the optimized concentration of Mn in  $Zn_{2-2x}GeO_4:Mn_{2x}$  phosphor which has maximum PL emission intensity. The relative luminescence quantum efficiency (QE) of phosphor was measured using a standard lamp phosphor,  $BaMgAl_{10}O_{17}$  (BAM), of known quantum efficiency (90%). For the calculations, integrated PL intensity of BAM and phosphors were measured at identical conditions such as sample weight, instrument settings, temperature (RT) and excitation wavelength (300nm).

The quantum efficiency of unknown sample is calculated using the equation,

$$QE (Sample) = \frac{QE_{BAM} \times \int I_{Sample}}{\int I_{BAM}} \quad (3.1)$$

Where,  $\int I_{Sample}$  and  $\int I_{BAM}$  are the integrated emission intensities of the unknown sample and the BAM phosphor, respectively.

### 3A.3. Results and Discussion

The optimum concentration of Mn for which maximum luminescent intensity observed was found by preparing 3 samples with 1 at. %, 2 at. % and 3 at. % Mn doped  $Zn_2GeO_4$ . The PL emission spectrum of the bulk phosphors is shown in figure 3.1. From the figure it is clear that the sample with 2 at. % doped Mn showed maximum luminescent intensity. The emission wavelength was same for all the three samples. The reduction in luminescent intensity above

2 at.% Mn doped sample can be attributed to luminescent quenching due to increased concentration of the activator which is often observed in phosphors.

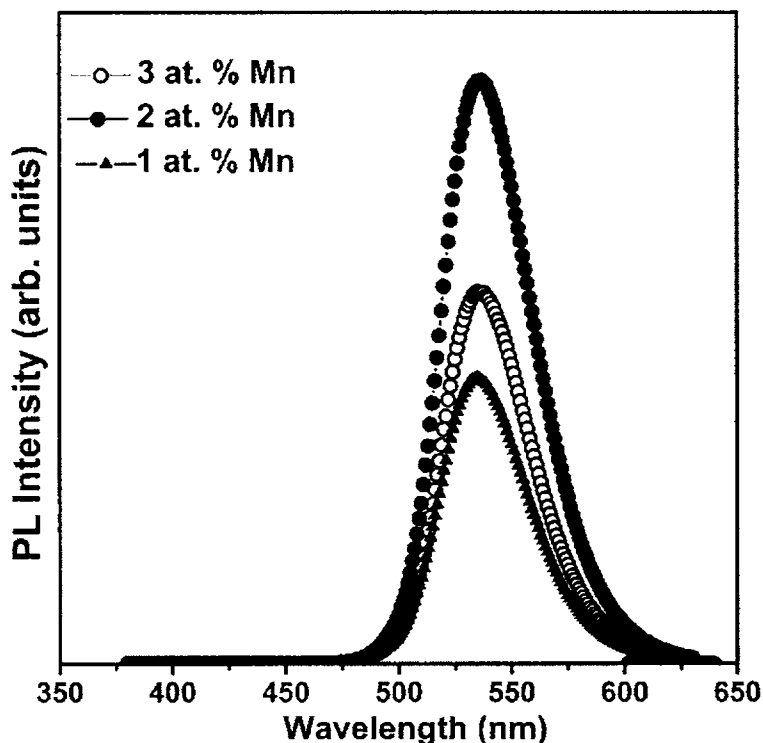


Figure 3.1 PL emission spectra of  $Zn_2GeO_4:Mn$  phosphor at various Mn concentrations ( $\lambda_{exc} = 332 \text{ nm}$ )

### 3A.3.1 X-ray diffraction studies

Figure 3.2 shows the XRD patterns of  $Zn_{1.96-1.96x}Mg_{1.96x}GeO_4:Mn_{0.04}$  ( $0 \leq x \leq 0.5$ ). The standard spectrum of undoped  $Zn_2GeO_4$  is plotted for reference [14]. The XRD pattern clearly implies that Mg is randomly substituting Zn in  $Zn_{1.96}GeO_4:Mn_{0.04}$  for concentrations up to  $x = 0.25$  forming a single phase,

preserving the hexagonal symmetry of the host lattice. No traces of constituent oxides were found in the diffraction patterns. The peaks other than that of  $\text{Zn}_2\text{GeO}_4$  are identified to be of orthorhombic  $\text{Mg}_2\text{GeO}_4$  [15]. But above  $x = 0.25$ , phase segregation commences limiting the solid solubility of Mg in  $\text{Zn}_{1.96}\text{GeO}_4:\text{Mn}_{0.04}$ . In wurtzite  $\text{Zn}_{1-x}\text{Mg}_x\text{O}$ , Mg is found to be soluble up to  $x = 0.33$  [16-18]. As the crystal structures of  $\text{Zn}_2\text{GeO}_4$  (rhombohedral) and  $\text{Mg}_2\text{GeO}_4$  (orthorhombic) are different, substitution of Zn with Mg will not occur for all concentrations and results in phase separation. Alloying is observed up to  $x = 0.25$  and the lattice constants of  $\text{Zn}_{1.96-1.96x}\text{Mg}_{1.96x}\text{GeO}_4:\text{Mn}_{0.04}$  are expected to change as  $\text{Zn}^{2+}$  and  $\text{Mg}^{2+}$  have different ionic radii (0.60pm and 0.57pm respectively) for four coordination [19].

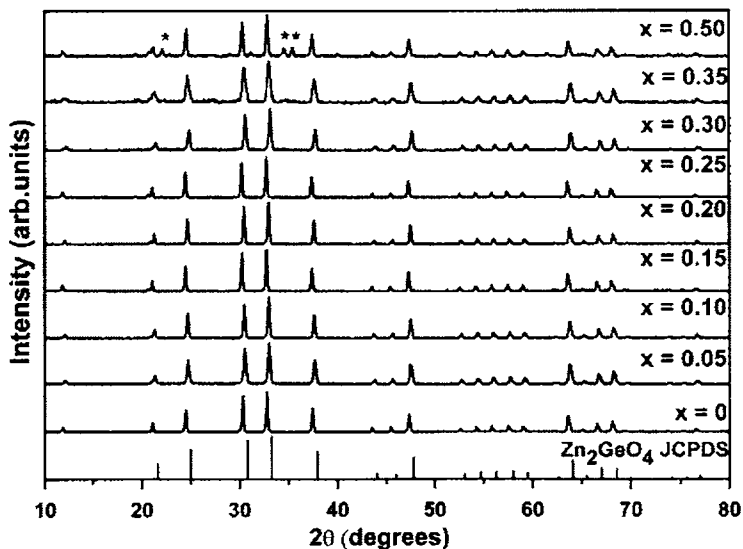


Figure 3.2 XRD patterns of  $\text{Zn}_{1.96-1.96x}\text{Mg}_{1.96x}\text{GeO}_4:\text{Mn}_{0.04}$ ,  $0 \leq x \leq 0.5$ . \* represents peaks of  $\text{Mg}_2\text{GeO}_4$

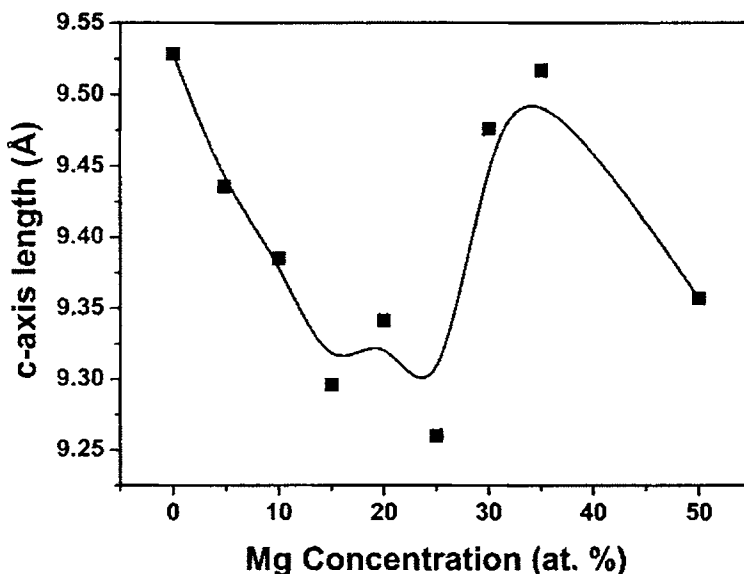


Figure 3.3 Variation of c-axis length with Mg concentration

The c-axis length and cell volume was calculated from the observed XRD data [20], the variation of which with Mg concentration is shown in figures 3.3 and 3.4 respectively. The c-axis length of  $Zn_2GeO_4$  is  $9.53\text{Å}$  and that of  $Mg_2GeO_4$  is  $4.91\text{Å}$ . The c-axis length show a contraction with increased Mg substitution up to  $x = 0.25$ . But for  $x = 0.30, 0.35$  and  $0.5$ , c-axis length increases. This is because as Mg concentration increases, simple substitution of Mg terminates and starts to segregate into different phases. However cell volume increases continuously up to  $x = 0.25$  and decreases for  $x = 0.30, 0.35$  and  $0.5$  which is due to an elongation in the 'a' parameter up to  $x = 0.25$ . The difference in cell volume is assumed to be due to the difference in ionic radii of  $Zn^{2+}$  and  $Mg^{2+}$  which also gives rise to difference in c-axis length.

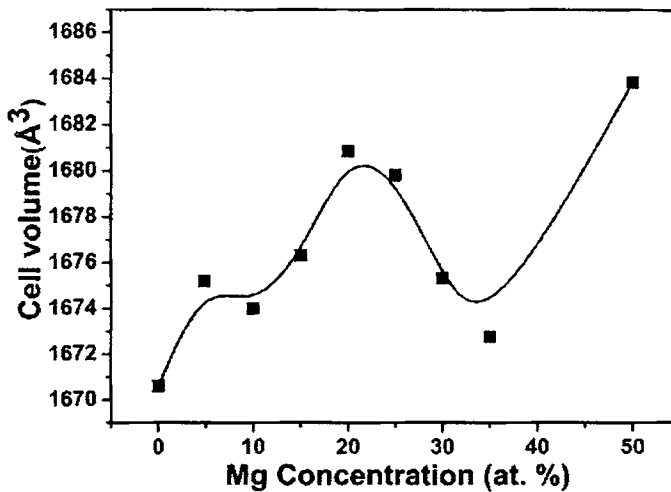


Figure 3.4 Variation of cell volume with Mg concentration.

The variation of FWHM of (410) XRD peak with Mg concentration is plotted in figure 3.5. There is gradual variation in the FWHM value up to  $x = 0.25$  which indicates Mg alloying in the  $Zn_2GeO_4$  lattice. However it shows a sudden increase at  $x = 0.30$  and  $0.35$  for which phase segregation takes place and for  $x = 0.5$  it again decreases. The substitution of Mg at Zn sites is expected to broaden XRD peak and interestingly maximum broadening is observed for  $x = 0.35$  at which phase segregates.

The c-axis length, cell volume and FWHM show almost similar behaviour with Mg substitution. A sudden change at  $x = 0.30$  and  $0.35$  is observed for all parameters which is due to the in-built strain caused by Mg substitution in the lattice and due to this strain phase segregates and above  $x = 0.35$   $Zn_2GeO_4$  and  $Mg_2GeO_4$  is separately formed and therefore beyond  $x = 0.35$  these parameters randomly approaches its previous value for which solid solution exists.

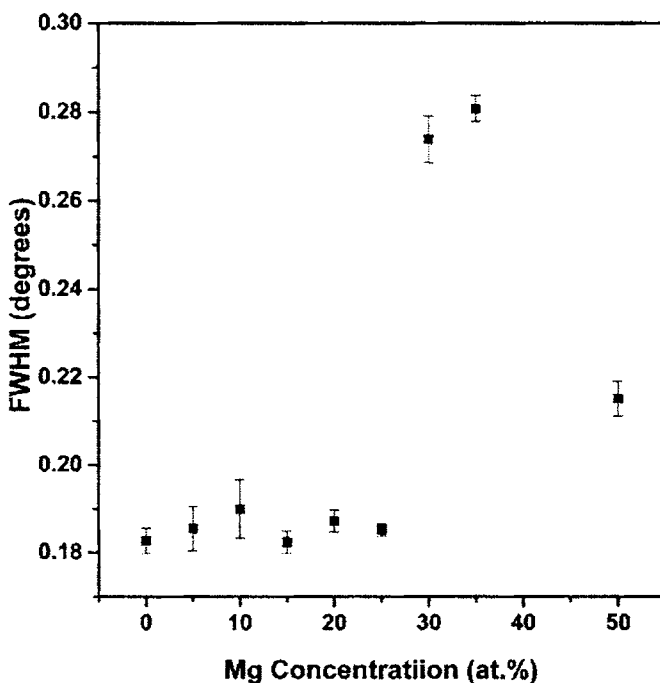


Figure 3.5 Variation of FWHM with Mg concentration

Therefore it can be concluded from the XRD studies that phase segregation occurs due to the inbuilt strain in the lattice due to Mg substitution and Mg is replacing Zn substitutionally.

### 3A.3.2 Optical characterization

#### (a) Diffused reflectance spectra analysis

Figure 3.6(a) shows the DRS spectra of  $Zn_{1.96-1.96x}GeO_4:Mn_{0.04}$  for the various Mg concentrations and the variation of band gap with Mg concentration. As the Mg doping percentage increases, the absorption edge blue-shifts.

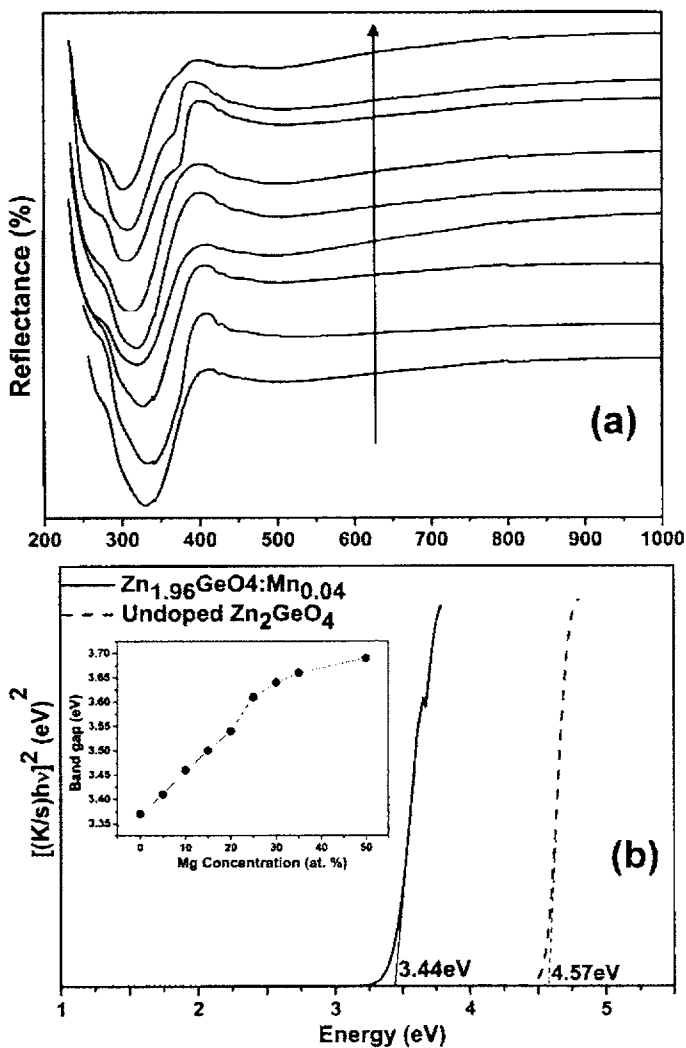


Figure 3.6 (a) The DRS spectra of  $\text{Zn}_{1.96-1.96x}\text{GeO}_4:\text{Mn}_{0.04}$ , Mg (arrow indicates x variation from 0 to 0.5 in steps of 0.05, final one being x = 0.5) (b) Band gap of pure  $\text{Zn}_2\text{GeO}_4$  and  $\text{Zn}_{1.96}\text{GeO}_4:\text{Mn}_{0.04}$ , Inset shows the variation in band gap with Mg concentration.

The band gap of pure Zn<sub>2</sub>GeO<sub>4</sub>, Zn<sub>1.96</sub>GeO<sub>4</sub>:Mn<sub>0.04</sub> and Zn<sub>1.96-1.96x</sub>Mg<sub>1.96x</sub>GeO<sub>4</sub>:Mn<sub>0.04</sub> samples were calculated from the  $((k/s).hv)^2$  vs  $hv$  plots, where  $k$  and  $s$  denotes the absorption and scattering coefficients respectively. The band gap of pure Zn<sub>2</sub>GeO<sub>4</sub> is found to be 4.57 eV and that of Mn doped Zn<sub>2</sub>GeO<sub>4</sub> is 3.44 eV (fig 3.6(b)). The reduced band gap for Zn<sub>1.96</sub>GeO<sub>4</sub>:Mn<sub>0.04</sub> sample is due to the formation of a sub-band gap states (discussed later). In the normal case Mg<sup>2+</sup> replaces Zn<sup>2+</sup> in Zn<sub>1.96</sub>GeO<sub>4</sub>:Mn<sub>0.04</sub> and there is a limit to this simple substitution since Zn<sub>2</sub>GeO<sub>4</sub> (rhombohedral) and Mg<sub>2</sub>GeO<sub>4</sub> (orthorhombic) crystallizes in to different crystal structures. Therefore the substitution of Mg<sup>2+</sup> at Zn<sup>2+</sup> sites creates strain in the lattice due to the reduced size of Mg<sup>2+</sup> which results in the blue shift of the absorption edge.

### **(b) Photoluminescence studies**

Figure 3.7 shows PL emission spectra of Zn<sub>1.96-1.96x</sub>Mg<sub>1.96x</sub>GeO<sub>4</sub>:Mn<sub>0.04</sub> (0 ≤ x ≤ 0.5). PL emission intensity is higher for x = 0.05, 0.10, 0.15, 0.20 when compared to x = 0 sample and intensity lowers beyond x = 0.25 compared to the undoped sample, the maximum being observed for the sample doped with 5 at. % Mg (x = 0.05).

The green luminescence at 535nm is observed from <sup>4</sup>T<sub>1</sub> → <sup>6</sup>A<sub>1</sub> transitions of 3d<sup>5</sup> electrons of Mn<sup>2+</sup> which substitutes the tetrahedrally coordinated Zn<sup>2+</sup> ions in rhombohedral Zn<sub>2</sub>GeO<sub>4</sub>, as the host provides only tetrahedral sites for substitution [14]. When Mg is co-doped in Zn<sub>1.96</sub>GeO<sub>4</sub>:Mn<sub>0.04</sub>, luminescent intensity varies due to the change in effective crystal field of tetrahedrally coordinated Mn<sup>2+</sup> ions. When Mg<sup>2+</sup> is incorporated in the lattice it creates excited state energy levels (consisting of 3s and 3p) near the excited state of Mn<sup>2+</sup> (comprising of <sup>4</sup>T<sub>1</sub>(<sup>4</sup>G), <sup>4</sup>T<sub>2</sub>(<sup>4</sup>G), <sup>4</sup>A<sub>1</sub>(<sup>4</sup>G), <sup>4</sup>T<sub>1</sub>(<sup>4</sup>P), shown in fig 3.10). Therefore

transition from the Mg levels to ground state of  $Mn^{2+}$  becomes more permissible, since the transition is more spin allowed compared to  $3d^5$  transitions of  $Mn^{2+}$  [21].

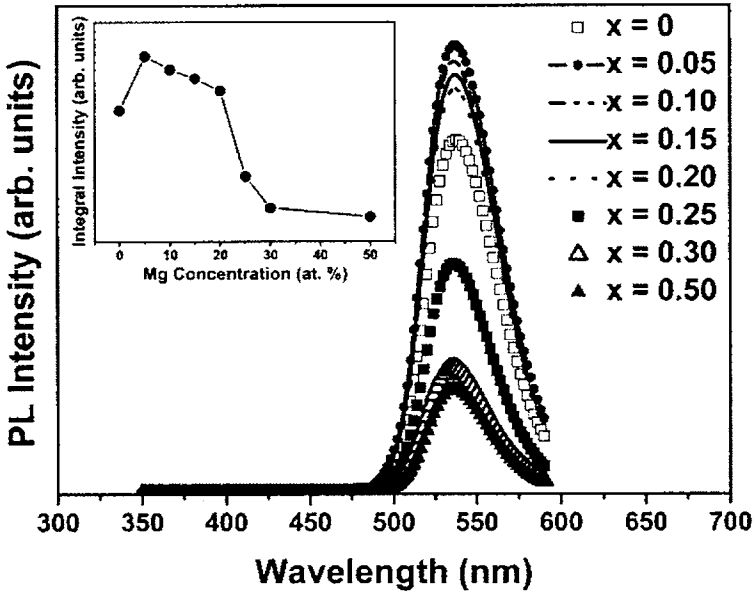


Figure 3.7 PL emission spectra of  $Zn_{1.96-1.96x}Mg_{1.96x}GeO_4:Mn_{0.04}$  ( $0 \leq x \leq 0.5$ ),  $\lambda_{exc} = 300nm$

However when concentration of Mg is increased, luminescent intensity decreases because effective transfer of charge via excited states of Mg will not take place due to inbuilt strain in the lattice. The quantum efficiency of the phosphor ( $Zn_{1.862}Mg_{0.098}GeO_4:Mn_{0.04}$ ) that showed maximum luminescent intensity is 41%, relative to BAM phosphor.

Figure 3.8 shows excitation and emission spectra of undoped  $Zn_2GeO_4$ . Undoped  $Zn_2GeO_4$  shows absorption at 266nm with a shoulder at 251nm for emission at 507nm. Pure  $Zn_2GeO_4$  shows a broad emission from 300 to 650

peaking at 507nm when excited with 266nm. But when  $Mn^{2+}$  is added the emission becomes narrow and shifts to 535nm and excitation maximum shifts to 335nm in addition to 266 nm (band edge) and 285 nm (direct excitation of  $Mn^{2+}$ ) absorption indicating the presence of a sub-band gap. The green luminescence from the undoped sample is a signature of intrinsic defect levels in the lattice during its synthesis.

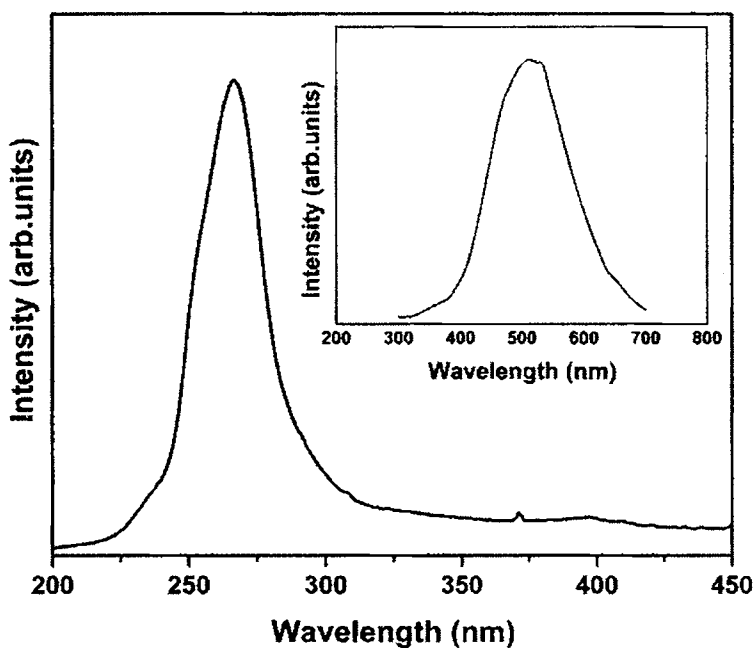


Figure 3.8 PLE spectra of Pure  $Zn_2GeO_4$  monitored at 507nm. Inset shows the emission spectra when excited at 266nm

Figure 3.9 shows PL excitation spectra of  $Zn_{1.96}GeO_4:Mn_{0.04}$  and inset shows variation of PLE peak wavelength with respect to the Mg addition in  $Zn_{1.96}GeO_4:Mn_{0.04}$ . PLE shifts to lower wavelength as Mg concentration is increased which is consistent with the results obtained from DRS spectra. The

spectra shows a shoulder at 285nm, while peak wavelength is at 335nm for  $x=0$  sample. The shoulder at 285nm and peak at 425nm is evidently direct excitation of tetrahedrally coordinated  $Mn^{2+}$  ions [22].

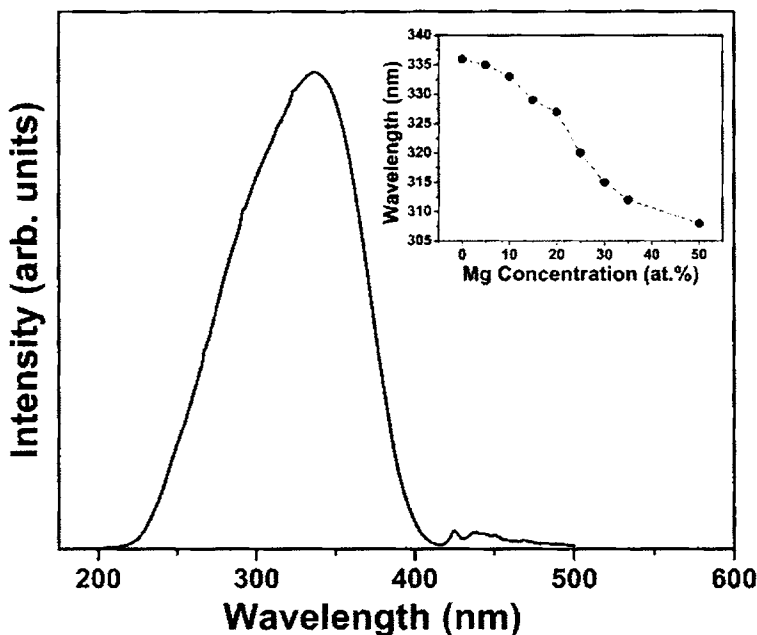


Figure 3.9 PLE spectra of  $Zn_{1.96}GeO_4:Mn_{0.04}$ . Inset shows variation of PL excitation with Mg concentration in  $Zn_{1.96-1.96x}Mg_{1.96x}GeO_4:Mn_{0.04}$

The bottom of the conduction band of  $Zn_2GeO_4$  is comprised of Ge 4p orbitals with a small contribution from Zn 4s and 4p orbitals and the upper part of the valence band is composed of O 2p levels [23]. The mechanism for the emission at 535nm is identified as band to band absorption and non-radiative transfer to a center, from which resonant transfer to activator takes place. This center lies nearly 1eV below the conduction band and is likely to be an oxygen defect which is also observed in the DRS spectra (fig 3.6). This can be formed

via migration of octahedrally coordinated Ge<sup>4+</sup> ions to tetrahedral position forming Ge<sup>3+</sup> ions [24]. Since the vapour pressure of Zn is high and high temperature solid state reaction is employed for the phosphor synthesis, Zn evaporation will take place leaving behind a vacancy and thereby occupying Zn vacancy sites by Ge<sup>3+</sup> ions migrated from the octahedral sites. This is also confirmed from EDX data. In all the samples, the cation ratio (Zn/Ge) ratio was found to be less (1.3 for x = 0) than the actual value (1.96 for x= 0). In ZnO, a donor level 0.8eV below the conduction band is observed which gives rise to green luminescence and is created due to oxygen vacancy [25]. When Mn is added to the Zn<sub>2</sub>GeO<sub>4</sub> host, it creates excited state energy levels near this center in such a manner that the charge transfer to Mn will take place through absorption via this center along with band to band absorption (266nm). Another possibility is Zn vacancy which could form an acceptor level above the valence band. This is also observed in ZnO, where an acceptor level nearly 0.8eV above valence band is formed due to Zn vacancy [25]. But resonant transfer from a low lying level to excited state levels of Mn<sup>2+</sup> is not possible. Other possibility is defect generated due to germanium. But that defect level will not be perturbed by adding Mg replacing Zn into tetrahedral position. Since the ionic radii of Mg<sup>2+</sup> and Ge<sup>4+</sup> is not comparable hardly a chance exists for Mg to replace Ge in Zn<sub>2</sub>GeO<sub>4</sub>. Therefore this trap level could be due to oxygen deficiency. The energy levels and the mechanism of PL emission in Zn<sub>2</sub>GeO<sub>4</sub>: Mn is schematically represented in figure 3.10.

When Mg is added to the system, it creates energy levels near the excited state levels of Mn<sup>2+</sup> and also it perturbs the V<sub>o</sub> level thereby shifting the

absorption edge. Therefore the DRS spectra and PLE spectra shows a blue shift when Mg is alloyed to  $\text{Zn}_2\text{GeO}_4:\text{Mn}$  host matrix.

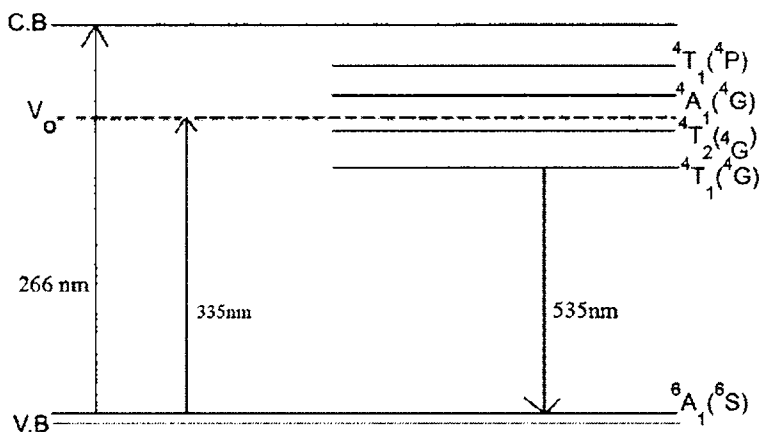


Figure 3.10 Energy level scheme describing the excitation and emission mechanism of  $\text{Zn}_2\text{GeO}_4:\text{Mn}^{2+}$  phosphor

### 3A.3.3 Electron Spin resonance (ESR) studies

The electron paramagnetic/spin resonance is a well-known technique for investigations of defects in crystalline and non-crystalline materials. The parameters resulting from the analysis of the observed spectra can provide the local site symmetry around the paramagnetic centers and the structure of the host material. Besides, ESR permits a chemical identification of the investigated center and frequently permits identification of associated defects along with a determination of their charge states and an estimate of their concentrations [26]. Figure 3.11 shows ESR spectra of  $\text{Zn}_{1.96-1.96x}\text{Mg}_{1.96x}\text{GeO}_4:\text{Mn}_{0.04}$  for  $0 \leq x \leq 0.5$ .

The spectra shows a strong and broad signal in the range of 3000 - 4000 gauss and can be assigned to  $V_0$  ( $g \approx 2.0$ ), which was also observed in other hosts [2,16]. Also in the lower magnetic field range (850-2000 G) a broad peak with six hyper fine lines is observed.

In  $ZnS:Mn$  it is observed that at lower Mn concentration, the six line hyper fine structure of the fine structure transition  $|1/2\rangle$  to  $|-1/2\rangle$  of  $Mn^{2+}$  ion will appear in the spectra while at higher concentrations, due to clustering, it will form a broad single spectrum [26]. The hyperfine structure originates from the interaction between  $^{55}Mn$  nucleus of spin  $I = 5/2$  and the electron cloud.

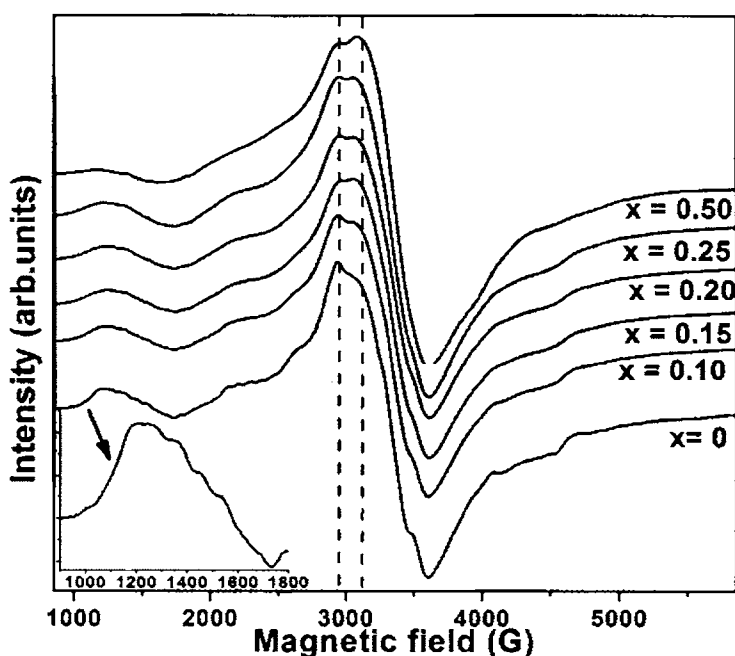


Figure 3.11 ESR spectra of  $Zn_{1.96-1.96x}Mg_{1.96x}GeO_4:Mn_{0.04}$  for  $0 \leq x \leq 0.5$ . Inset shows enlarged view of the spectra in lower magnetic fields.

More over crystal field has much influence on the nature of spectra. It was reported that the EPR signals of the ions with unpaired electrons may shift to low magnetic field ( $g$  value increases) at the site with stronger crystal field [27, 28]. Here also we get a signal with six hyperfine lines in the low magnetic

field regime (inset of figure 3.11). Three different sites of  $\text{Eu}^{2+}$  were proposed in  $\text{Ba}_3\text{MgSi}_2\text{O}_8:\text{Eu}$ , Mn phosphor as they observed signals at three different magnetic field regimes [27]. But here  $\text{Mn}^{2+}$  is supposed to replace  $\text{Zn}^{2+}$  as there is charge imbalance and variation in ionic radii with  $\text{Ge}^{3+}$  ions. Besides, if at high temperature,  $\text{Mn}^{2+}$  has been oxidized to  $\text{Mn}^{4+}$  and replaced  $\text{Ge}^{3+}$  (which is possible due to similar ionic radii for both ions in six coordination), the luminance would be in the red region. But no red luminescence could be observed in the PL spectra. So the possibility of  $\text{Mn}^{2+}$  and  $\text{Mn}^{4+}$  replacing  $\text{Ge}^{4+}$  ion is ruled out.

The deviation from  $g_e$  can also be from the contribution of orbital magnetic moment and can be written as

$$g - g_e = \frac{\xi}{E_{d1} - E_{d2}} \quad (3.1)$$

where  $\xi$  is the spin-orbit coupling constant and  $E_{d1}$  and  $E_{d2}$  represents energy gap between d orbitals [29]. In some cases, the contribution of the orbital magnetic moments is mixed into the  $g$  value, which is related to the energy gap between the ground state and the lowest excitation state. The narrower the gap is, the more orbital magnetic moment is contributed, which results in larger  $g$  value.

The peak around 3300 G ( $g \approx 2$ ) can be attributed to singly ionized oxygen vacancy ( $\text{V}_o$ ). This peak due to singly ionized oxygen vacancy ( $\text{V}_o$ ) is also observed in undoped pure  $\text{Zn}_2\text{GeO}_4$  due to its native defects [30]. In  $\text{ZnS}:\text{Mn}$  the broadening of resonant signal (highly resolved six lines) is observed and it is attributed to the clustered Mn ions due to higher concentration which strongly influence one another through their magnetic moments [26]. So the corresponding broadening is also observed in the spectra. However a strong signal at  $g \approx 2$  due to singly ionized  $\text{Zn}^+$  vacancy is observed by Tian *et al.* in

zeolite [31]. But hardly a chance exists for possibility of existence of Zn<sup>+</sup> ion in the lattice as it is highly unstable. As Mg is incorporated in to the Zn<sub>2</sub>GeO<sub>4</sub> system, a variation in the ESR spectra is observed which is expected as now system is getting too complicated and above x = 0.25 no solid solution exists and phase segregates.

## **Conclusion**

In summary, Mg alloyed Zn<sub>1.96</sub>GeO<sub>4</sub>:Mn<sub>0.04</sub> phosphor was prepared by solid state reaction. The structural analysis reveals the formation of solid solution up to x = 0.25 in Zn<sub>1.96-1.96x</sub>Mg<sub>x</sub>GeO<sub>4</sub>:Mn<sub>0.04</sub>. Beyond x = 0.25, phase segregation occurs. The absorption edge as observed from DRS and PLE spectra of Mn and Mg doped samples indicates the presence of a sub-band gap and was found to be blue shifted with increase in Mg substitution. The PL emission spectra exhibits increase in luminescent intensity with Mg concentration at x = 0.05 in Zn<sub>1.96-1.96x</sub>Mg<sub>1.96x</sub>GeO<sub>4</sub>:Mn<sub>0.04</sub> phosphor. The phosphor can be used as an active layer in ACTFEL devices.

## **PART B**

---

# **Synthesis and characterization of Mg<sub>2</sub>GeO<sub>4</sub>: Mn<sup>2+</sup> phosphor**

---

### **3B.1 Introduction**

One of the necessary criteria to be a phosphor host is the wide band gap. The band gap should be greater than 3eV so that visible radiation emitted by the activator/impurity is not absorbed by the host. But there is a limit to band gap for electroluminescent display phosphors, above which no electroluminescence is observed, since in most cases luminescence arises due to resonant energy transfer from the host to activator. Efficient host materials for ACTFEL phosphors are generally limited to those materials with bandgap energies in the range of 3.5- 4.5 eV. Manganese is an excellent activator for yellow (in ZnS) [2], green ( $ZnGa_2O_4$ ,  $Zn_2GeO_4$ ) and red ( $ZnMgS$ ) [32],  $Mg_2GeO_4$  [33]) emissions. Eu and Cr doped  $Mg_2GeO_4$  also shows red emission, serves as a phosphor for plasma display panels [32, 33]. In orthorhombic  $Mg_2GeO_4$  ( $a = 10.29 \text{ \AA}$ ,  $b = 6.023 \text{ \AA}$ ,  $c = 4.905 \text{ \AA}$ )  $Mg^{2+}$  ions occupy tetrahedral sites while  $Ge^{3+}$  ions occupy octahedral sites in crystal lattice. The wide optical band gap of  $Mg_2GeO_4$  makes it as a suitable candidate for wide band gap oxide phosphor. However efficient high field electroluminescence from  $Mg_2GeO_4$  host material is not observed due to its high band gap and inefficient transfer of energy from the host to activator. Also  $Mg_2GeO_4:Mn$  phosphor has not been widely studied for luminescent applications. Co-doping has been proved as an excellent technique for engineering the band gap [17, 21, 36]. Among the various ions that can replace Mg, Zn is better choice due to its similarity in ionic radii and valency. More over the band gap of ZnO has been engineered by alloying it with Mg for many optoelectronic applications [17]. Alloying up to  $x = 0.33$  is observed in  $Zn_{1-x}Mg_xO$  thin films [36]. Due to abundance and non-toxicity, compared to other ions like Cd, Zn is more appropriate co-dopant for

engineering the band gap of  $\text{Mg}_2\text{GeO}_4$ . In the present work, the effect of zinc alloying on the crystal structure, band gap and photoluminescence of  $\text{Mg}_2\text{GeO}_4:\text{Mn}$  is studied.

## 3B.2 Experiment

The samples were synthesised by conventional high temperature solid-state reaction of constituent oxides namely  $\text{MgO}$ ,  $\text{ZnO}$ ,  $\text{GeO}_2$ . Manganese was added in the form of manganous acetate  $[\text{Mn}(\text{CH}_3\text{COO})_2]$ . The stoichiometric powders were mixed in ethanol medium and calcined in air at  $1200^\circ\text{C}$  for 12 hrs in a tubular furnace to obtain  $\text{Mg}_{1.96-1.96x}\text{Zn}_{1.96x}\text{GeO}_4:\text{Mn}_{0.04}$  ( $x$  was varied from 0 to 0.5). The concentration of Mn was fixed at 2 at. % in all the samples. The concentration of Zn was varied from 0 to 50 at.% of Mg.

## 3B.3 Results and Discussion

### 3B.3.1 X-ray diffraction studies

Figure 3.12 shows XRD patterns of pure  $\text{Mg}_2\text{GeO}_4:\text{Mn}$ , pure  $\text{Zn}_2\text{GeO}_4:\text{Mn}$  and  $\text{Mg}_{1.96-1.96x}\text{Zn}_{1.96x}\text{GeO}_4:\text{Mn}_{0.04}$  at different concentrations ( $x = 0.1, 0.15, 0.20, 0.25, 0.5$ ) of zinc. The pattern clearly shows the formation of solid solution up to  $x = 0.10$ . But above  $x = 0.10$ , additional peaks are observed indicating phase segregation. These additional peaks are identified as that of  $\text{Zn}_2\text{GeO}_4$ . No traces of constituent oxides like  $\text{ZnO}$  and  $\text{MgO}$ , were found in the XRD pattern as the pattern matches well with the JCPDS data of  $\text{Zn}_2\text{GeO}_4$  [14] and  $\text{Mg}_2\text{GeO}_4$  [15]. Normally magnesium germanate crystallizes in orthorhombic structure and zinc germanate crystallizes in rhombohedral structure, thereby limiting simple incorporation of Zn in to  $\text{Mg}_2\text{GeO}_4$  lattice. Also the ionic radii of Zn and Mg differ; substituting Mg with Zn will not be

possible for all concentrations and at a particular concentration phase will start to segregate. The phase segregation occurs due to inbuilt strain due to the difference in ionic radii and strain reaches a maximum at particular Zn concentration. However in  $Zn_{1.96-1.96x}Mg_{1.96x}GeO_4$  Mg forms solid solution up to  $x= 0.3$  clearly indicating that rhombohedral  $Zn_2GeO_4$  have more stability than  $Mg_2GeO_4$  naturally favouring the formation of  $Zn_2GeO_4$ .

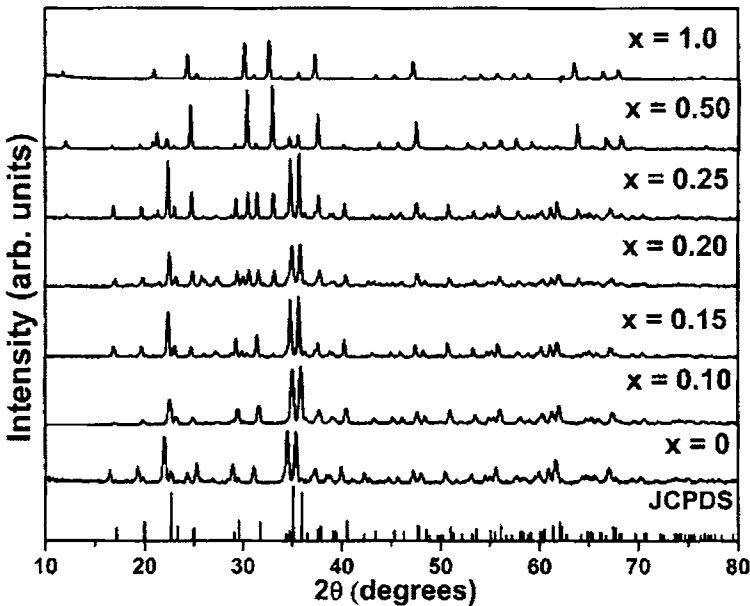


Figure 3.12 XRD patterns of  $Mg_{1.96-1.96x}Zn_{1.96x}GeO_4:Mn_{0.04}$  ( $0 \leq x \leq 1$ ) JCPDS of  $Mg_2GeO_4$  is shown as reference

Therefore as more and more Zn adds to the  $Mg_2GeO_4:Mn$  system, formation of  $Zn_2GeO_4:Mn$  is favoured and when  $x = 0.5$ ,  $Zn_2GeO_4$  phase got enhanced thereby forming  $Zn_{1.96-1.96x}Mg_{1.96x}GeO_4:Mn$ . The cell volume [20] is

found to increase with  $x$  which is expected as the cell volume of  $Zn_2GeO_4$  is larger than that of  $Mg_2GeO_4$  (fig.3.13).

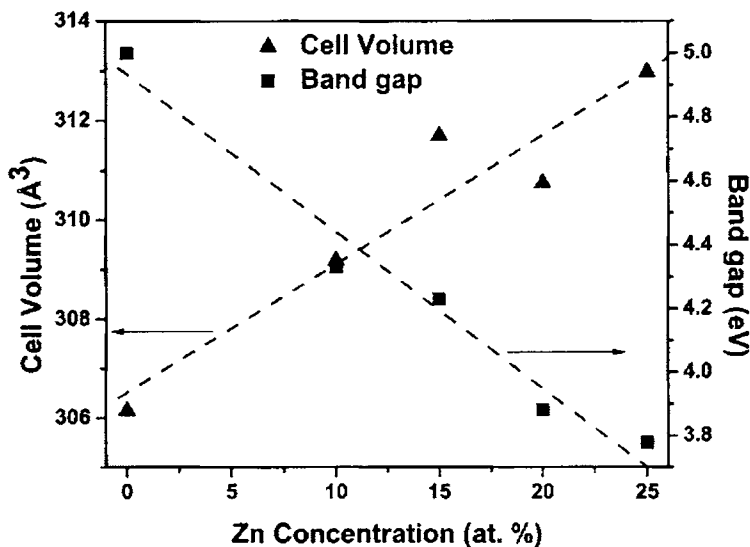


Figure 3.13 Variation of Cell volume and band gap with Zn concentration. Straight (dashed) line shows apparent linear fit to data.

The band gap of  $Mg_2GeO_4:Mn^{2+}$  and  $Zn_2GeO_4:Mn^{2+}$ , calculated from the spectra are 5 eV and 3.45 eV respectively. In both cases strong sub-band absorption is observed. This sub band state lie nearly 1 eV below the conduction band is formed due to intrinsic oxygen vacancies during the compound formation. The schematic energy level scheme is shown in the figure 3.14.

### 3B.3.2 Diffused reflectance spectra (DRS) analysis

The variation of band gap of  $Mg_2GeO_4:Mn$  with Zn concentration ( $x$ ) is shown in figure 3.15. As  $x$  increases band gap is found to be red-shifted. Figure clearly indicates mixed phase for doped samples ( $x = 0.15, 0.2, 0.25$  and  $0.5$ ).

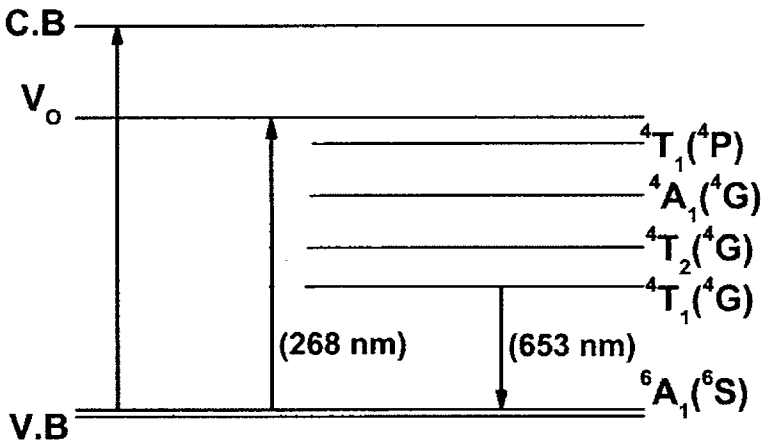


Figure 3.14 Energy level scheme describing the excitation and emission mechanism of  $Mg_2GeO_4:Mn$  phosphor

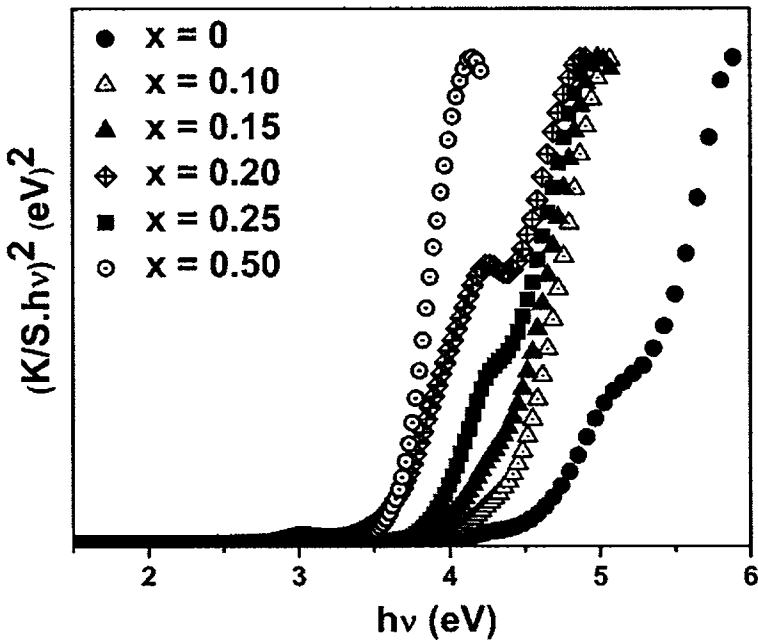


Figure 3.15 The band gap of  $Mg_{1.96-1.96x}Zn_{1.96x}GeO_4:Mn_{0.04}$ , ( $0 \leq x \leq 0.5$ )

So from the DRS spectra it is concluded that formation of solid solution is favoured for the zinc addition up to  $x=0.10$  and beyond that phase segregation occurs due to inbuilt strain in the lattice. The shift in band gap can be attributed to difference in ionic radii of  $Zn^{2+}$  and  $Mg^{2+}$  ions. Moreover when Zn is co-addition in to  $Mg_2GeO_4$  system,  $Zn^{2+}$  will create states below the sub band levels created due to oxygen vacancy. So as more and more Zn gets added in to the  $Mg_2GeO_4$  matrix, the band gap reduces.

### 3B.3.3 Photoluminescence studies

Figure 3.16 shows PL emission spectra of  $Mg_{1.96-1.96x}Zn_{1.96x}GeO_4:Mn_{0.04}$  ( $0 \leq x \leq 0.25$ ) samples.

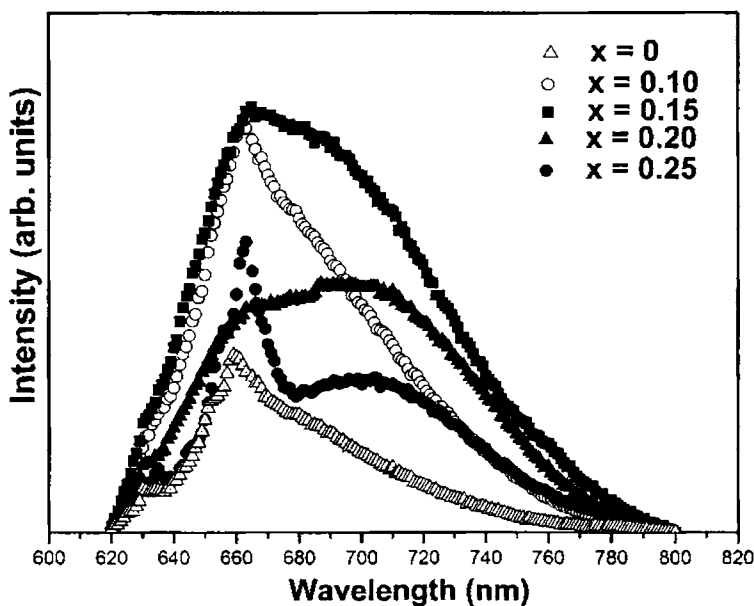


Figure 3.16 PL emission spectra (red) of  $Mg_{1.96-1.96x}Zn_{1.96x}GeO_4$  ( $0 \leq x \leq 0.25$ ),  $\lambda_{exc} = 300$  nm

All samples show emission in the red region and has intensity greater than Zn free sample. But the peak emission wavelength changes as x varies. In  $Mg_2GeO_4:Mn$  the emission is observed from tetrahedrally coordinated  $Mn^{2+}$  at Mg sites [33]. The  $3d^5$  electrons of  $Mn^{2+}$  is highly influenced by crystal field environment. The crystal field environment determines the colour or the emission wavelength of the activator. Moreover the energy transfer mechanism is not so efficient as in the case of  $Zn_2GeO_4:Mn$ . In  $Zn_2GeO_4$  the mechanism of PL is identified as resonant energy transfer from a sub-band gap level, due to intrinsic defects, to  $Mn^{2+}$  levels [24]. In  $Mg_2GeO_4$  also a sub-band gap level is observed as the  $Mn^{2+}$  emission is triggered from a level which is nearly 1 eV below the conduction band. But this level is not in the vicinity of excited levels of  $Mn^{2+}$  for efficient resonant energy transfer to take place. But as more Zn is added to the system, transfer will take place to  $Mn^{2+}$  levels through  $Zn^{2+}$  levels formed near  $Mn^{2+}$  levels. This is also observed in DRS measurements as reduction in band gap is observed as more Zn adds to the system.

However no red emission can be detected from  $x = 0.5$  sample indicating the complete replacement of  $Mn^{2+}$  at  $Zn^{2+}$  sites in  $Zn_2GeO_4$ . Therefore similar to the formation of  $Zn_2GeO_4$ , which is more favourable,  $Mn^{2+}$  is more likely to replace  $Zn^{2+}$  rather than  $Mg^{2+}$ . Green emission (fig 3.17) is also detected from the samples at and above  $x = 0.15$  clearly showing the limit of solid solubility of Zn in  $Mg_2GeO_4:Mn$ . But in  $Zn_2GeO_4:Mn^{2+}$ , Mg is found to be soluble up to  $x = 0.3$ . This is due to greater stability of rhombohedral  $Zn_2GeO_4$  structure compared to orthorhombic  $Mg_2GeO_4$ . The green emission at 535 nm can be attributed to  ${}^4T_1 \rightarrow {}^6A_1$  transition of  $Mn^{2+}$  in  $Zn_2GeO_4$  and gets enhanced when Zn concentration increases. The photoluminescence excitation (PLE)

spectra for red emission (653nm) are shown in the figure 3.18. A broad excitation peaking at 268 nm is obtained for  $\text{Mg}_2\text{GeO}_4:\text{Mn}$  which is found to be red-shifted as more  $\text{Zn}^{2+}$  replaces  $\text{Mg}^{2+}$ .

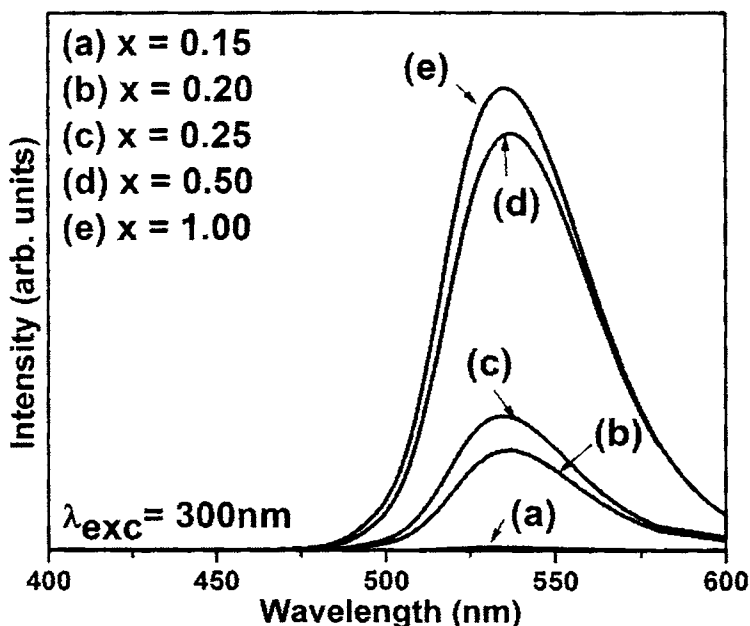


Figure 3.17 Room temperature Photoluminescent emission spectra (green) of  $\text{Mg}_{1.96-x}\text{GeO}_4:\text{Mn}_{0.04}$  ( $0 \leq x \leq 0.5$ ),  $\lambda_{\text{exc}} = 300 \text{ nm}$

In  $\text{Zn}_2\text{GeO}_4:\text{Mn}$  PLE at 332 nm is obtained for emission at 535nm showing the formation of sub-band gap. Since increased Zn concentration results in phase segregation, the excitation for red emission shifts to higher wavelength region indicating the presence of  $\text{Zn}_2\text{GeO}_4$ . The PLE spectra for  $\lambda_{\text{em}} = 535 \text{ nm}$ , show a peak at 300nm, for  $x = 0.50$  sample, indicating the formation of  $\text{Zn}_{1.96-x}\text{Mg}_{1.96x}\text{GeO}_4$ , Mg being substituted for Zn, thereby emphasizing the fact that formation of  $\text{Zn}_2\text{GeO}_4$  is more favored rather than  $\text{Mg}_2\text{GeO}_4$ .

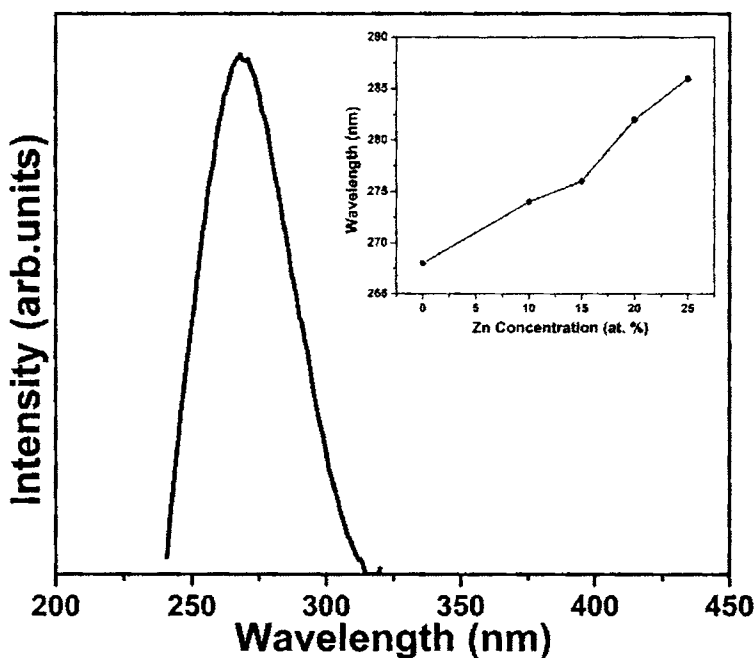


Figure 3.18 PLE spectra of  $Mg_{1.96}GeO_4:Mn_{0.04}$  and inset shows its variation with Zn concentration,  $\lambda_{em} = 653$  nm

### 3B.3.4 Electron spin resonance (ESR) studies

Figure 3.19 shows the variation ESR spectra for various concentrations of Zn in  $Mg_2GeO_4:Mn$  phosphor. It is clear from the spectra (see figure 3.20 ) that both hosts offer entirely different crystal field to the  $Mn^{2+}$  ions or we can say that the environment as observed by  $Mn^{2+}$  in both cases is entirely different. But as more Zn adds to  $Mg_2GeO_4:Mn$  system, the spectra shows variation and at  $x = 0.25$  the spectrum is almost similar to  $Zn_2GeO_4:Mn$  there by emphasizing the fact that the formation of  $Zn_2GeO_4$  is more favoured. For  $x = 0$  a strong signal at  $g = 2$  is observed which can be attributed to singly ionized oxygen vacancy and also small isolated signals related to Mn is also observed.

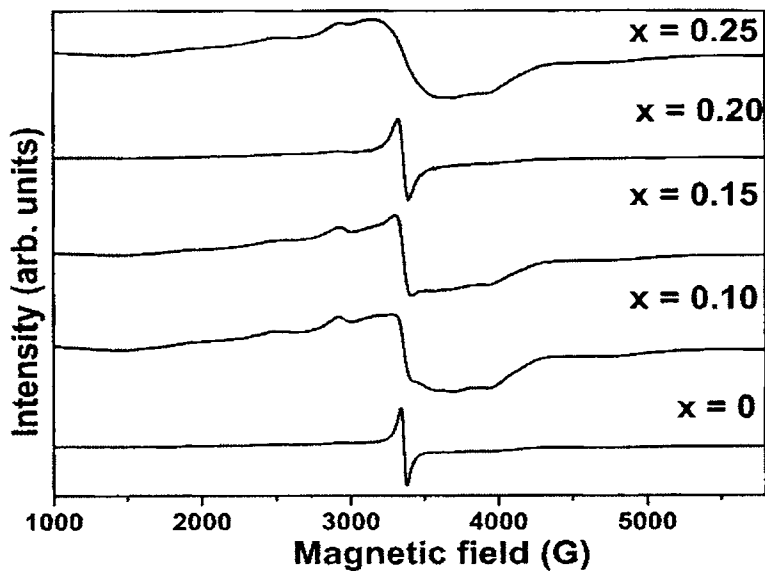


Figure 3.19 ESR spectra of  $\text{Mg}_{1.96-1.96x}\text{Zn}_{1.96x}\text{GeO}_4:\text{Mn}_{0.04}$  for  $0 \leq x \leq 0.25$

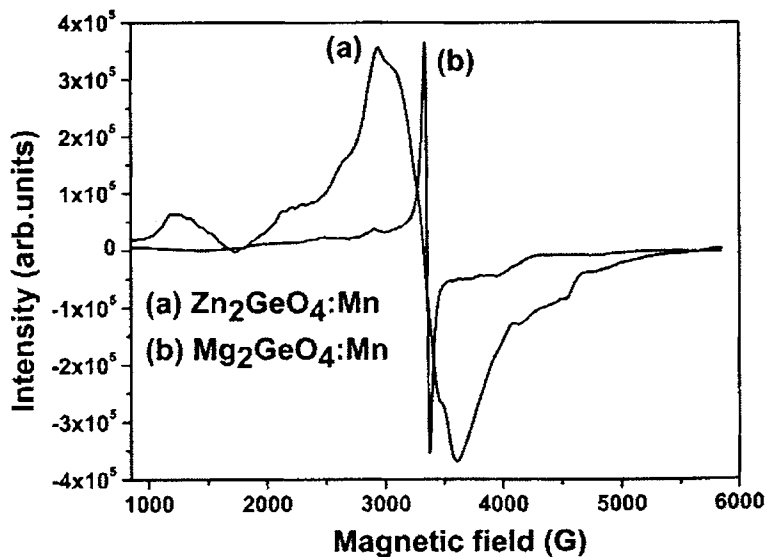


Figure 3.20 ESR spectra of  $\text{Zn}_2\text{GeO}_4:\text{Mn}$  and  $\text{Mg}_2\text{GeO}_4:\text{Mn}$

## Conclusion

Manganese doped  $Mg_2GeO_4$  is synthesized by solid state reaction. The phosphor shows emission in red region. The effect of Zn alloying on structural and optical properties have been explored in detail. XRD patterns show solid solution formation up to 10 at% Zn addition and beyond that phase segregation occurs. When Zn is added in to  $Mg_2GeO_4:Mn$ , PL emission intensity increases compared to Zn free sample and PL peak excitation wavelength red-shifted with Zn addition. Both green and red emission is observed for Zn concentrations above 10 at% indicating the presence of  $Mn^{2+}$  ions replacing Mg in  $Mg_2GeO_4$  and Zn in  $Zn_2GeO_4$ . The phosphor can be used as an active layer in alternating current thin film electroluminescent (ACTFEL) devices.

## References

1. C. B. Thomas and W. N. Cranton, *Appl. Phys. Lett.*, **63**, 3119 (1993)
2. M. K. Jayaraj and C. P. G. Vallabhan, *J. Electrochem. Soc.*, **138**, 1512, (1991)
3. K. Ohmi, K. Yamabe, H. Fukada, T. Fujiwara, S. Tanaka and H. Kobayashi, *Appl. Phys. Lett.*, **73**, 1889(1998)
4. B. A. Baukol, J. C. Hitt, P. D. Keir and J. F. Wager, *Appl. Phys. Lett.*, **76**, 185 (2000)
5. T. Minami, *Solid state electron.*, **47**, 2237(2003)
6. A. H. Kitai, *Thin Solid Films*, **445**, 367(2003)
7. S. Itoh, H. Toki, Y. Sato, K. Morimoto and T. Kishino, *J. Electrochem. Soc.*, **138**, 1509 (1991)

8. T. Minami, Y. Kuroi, T. Miyata, H. Yamada and S. Takata, *J. Lumin.*, **72**, 997(1997)
9. I. K. Jeong, H. L. Park and S. I. Mho, *Solid State Commun.* **108**, 823 (1998)
10. K. Mini Krishna, G. Anoop and M. K. Jayaraj, *J. Electrochem. Soc.*, **154**, J310 (2007)
11. K. H. Hsu, M. R. Yang and K.S Chen, *J. Mater. Sci.:Mater. Electron.*, **9**, 283(1998)
12. T. Minami, Y. Kuroi and S. Takata, *J. Vac. Sci. Technol. A*, **14**, 1736(1996)
13. L. C. Williams, D. Norton, J. Budai and P. H. Holloway, *J. Electrochem. Soc.*, **151**, H188 (2004)
14. JCPDS card no: 11-0687
15. JCPDS card no: 36-1479
16. T. H. Yeom, Y. H. Lee, T. S. Hahn, M. H. Oh and S. H. Choh, *J. Appl. Phys.*, **79**, 1004(1996)
17. A. Ohtomo, M. Kawasaki, T. Koida, K. Masabuchi, H. Koinama, Y. Sakurai, Y. Yoshida, T. Yasuda and Y. Segawa, *Appl. Phys. Lett.*, **72**, 2466(1998)
18. A. Ohtomo, M. Kawasaki, I. Ohkubo, H. Koinuma T. Yasuda and Y. Segawa, *Appl. Phys. Lett.*, **75**, 980 (1999)
19. R. D. Shannon, *Acta Cryst. A* **32**, 751 (1976)
20. B.D. Cullity, S.R Stock, *Elements of X-Ray diffraction*, 3<sup>rd</sup> ed., Prentice Hall, New York (2001) pp 303.
21. K. S. Soha, B. Cho, H. Chang and H. D. Park, *J. Electrochem. Soc.*, **146**, 2353 (1999)
22. L. Shea, R. K. Dutta and J. J. Brown, Jr, *J. Electrochem. Soc.*, **141**, 1950 (1994)

23. J. Sato, H. Kobayashi, K. Ikarashi, N. Saito, H. Nishiyama, and Y. Inoue, *J. Phys. Chem.*, **108**, 4369 (2004)
24. V. Bondar, S. Popovich, T. Felter and J. F Wager, *Mater. Res. Soc. Symp. Proc.*, **667**, G761 (2001)
25. U. Ozgur, Y. I. Alivov, C. Liu, A. Teke, M. A. Reshchikov, S. Dogan, V. Avrutin, S. J. Cho and H. Markoc, *J. Appl. Phys.*, **98**, 041301(2005)
26. T. H. Yeom, Y. H. Lee, T. S. Hahn, M. H. Oh and S. H. Choh, *J. Appl. Phys.*, **79**, 1006 (1996)
27. J. S. Kim, P. E. Jeon, J. C. Choi, H. L. Park, S. I. Mho and G. C. Kim, *Appl. Phys. Lett.*, **84**, 2931 (2004)
28. S. H. Lee, J. H. Park, S. M. Son, and J. S. Kim and H. L. Park, *Appl. Phys. Lett.*, **89**, 221916 (2006)
29. J. Telsler, *J. Braz. Chem. Soc.*, **17**, 1501 (2006)
30. Z. Liu, X. Jing and L. Wang, *J. Electrochem. Soc.*, **154**, H500 (2007)
31. Y. Tian, G. D. Li and J. S. Chen, *J. Am. Chem. Soc.*, **125**, 6622 (2003)
32. M. K. Jayaraj, A. Antony and P. Deneshan, *Thin Solid Films*, **389**, 284 (2001)
33. M. Iwasaki, D. N. Kim, K. Tanaka, T. Murata and K. Morinaga, *Sci. Technol. Adv. Mat.*, **4**, 137 (2003)
34. H. M. Yang, J. X. Shi, H. B. Liang and M. L. Gong, *Mater. Sci. Engg. B*, **127**, 276 (2006)
35. S. G. Demos, B. Y. Han, V. Petričević, and R. R. Alfano, *J. Opt. Soc. Am. B*, **13**, 2396 (1996)
36. T. Makino, Y. Segawa, M. Kawasaki, A. Ohtomo, R. Shiroki, K. Tamura, T. Yasuda and H. Koinuma, *Appl. Phys. Lett.*, **78**, 1237(2001)

## **CHAPTER 4**

---

# **Growth and Characterization of Oxide Phosphor Thin films**

---

*The present chapter deals with growth and characterization of oxide phosphor thin films and the chapter is divided in to three parts. Part A deals with structural and optical characterizations of rf magnetron sputtered  $\text{ZnGa}_2\text{O}_4:\text{Mn}$  thin films. Thin films were deposited on glass/quartz at various substrate temperatures. The effect of a dopant source on structural and luminescent properties of  $\text{ZnGa}_2\text{O}_4:\text{Mn}$  thin films is discussed.*

*Part B discusses growth and characterization of  $\text{Zn}_2\text{GeO}_4:\text{Mn}$  thin films using rf magnetron sputtering. The effect of a ZnO buffer layer on structural and luminescent properties is discussed. It is observed that the presence of ZnO buffer layer enhances both crystalline quality and luminescent quality of  $\text{Zn}_2\text{GeO}_4:\text{Mn}$  films.*

*Part C deals with the growth and characterization of pulsed laser deposited  $\text{Y}_2\text{O}_3:\text{Eu}^{3+}$  thin films. The effect of oxygen partial pressure and substrate temperature on structural and luminescent properties on deposited films is discussed. All the deposited films exhibit red luminescence with peak emission at 611 nm.*

## **PART A**

---

# **Growth and characterization of RF magnetron sputtered $\text{ZnGa}_2\text{O}_4:\text{Mn}^{2+}$ thin films**

---



## **4A.1. Introduction**

The future flat panel display (FPD) technologies demand highly efficient phosphor materials for better performance. Over a decade, oxide phosphors has been a subject of interest for their use in flat panel displays (FPD). Due to high thermal stability and long durability, oxide phosphors over-rule the commercially available and established sulphides, used in alternating current thin film electroluminescent (ACTFEL) displays [1,2]. Several binary and ternary oxide phosphors like Y<sub>2</sub>O<sub>3</sub> [3], Ga<sub>2</sub>O<sub>3</sub> [4, 5], ZnGa<sub>2</sub>O<sub>4</sub> [6-10], Zn<sub>2</sub>GeO<sub>4</sub> [11-17], Mg<sub>2</sub>GeO<sub>4</sub> [18] etc have been extensively studied in bulk powder as well as in thin film form. Moreover high luminance green and red thick dielectric electroluminescent (TDEL) devices has been realized using doped ternary oxides like Zn<sub>2</sub>SiO<sub>4</sub> [1], ZnGa<sub>2</sub>O<sub>4</sub> [7-10] and Zn<sub>2</sub>Si<sub>(1-x)</sub>Ge<sub>x</sub>O<sub>4</sub>[19]. Among these ternary oxides, ZnGa<sub>2</sub>O<sub>4</sub> is a low voltage cathodoluminescent (LVCL) phosphor that gives excellent green emission on Mn doping [20]. When excited by a 254 nm UV light, ZnGa<sub>2</sub>O<sub>4</sub> exhibits blue emission due to its self activated luminescence [21]. It has Fd3m space group symmetry and crystallizes in the normal spinel structure with Zn<sup>2+</sup> ions occupying tetrahedral sites and Ga<sup>3+</sup> ions occupying octahedral sites. Zinc gallium oxide has a wide optical band gap of about 4.4 eV allowing tunability in the visible to UV range making it an ideal material for optoelectronic devices including FPDs, optical limiter for UV light and high temperature stable gas sensors [22]. Thin films of these compounds have been prepared using several techniques like rf magnetron sputtering [23-27], PLD [28-31], CVD [4] etc. Also white luminescence has been observed from ZnGa<sub>2</sub>O<sub>4</sub>:Dy<sup>3+</sup> bulk phosphor as well as thin films [32, 33]. Manganese has been used as an activator for obtaining high luminance green emission in these

compounds. In  $\text{ZnGa}_2\text{O}_4$ , Mn occupies tetrahedral  $\text{Zn}^{2+}$  sites exhibiting green luminescence at 507 nm due to transition via  ${}^4\text{T}_1$ - ${}^6\text{A}_1$  states of  $\text{Mn}^{2+}$ [34, 35]. Manganese can be introduced into host material via several compounds like  $\text{MnO}$ ,  $\text{MnCO}_3$ ,  $\text{MnNO}_3$ ,  $\text{MnSO}_4$ ,  $(\text{CH}_3\text{COO})_2\text{Mn}$  etc. The dopant source does not affect the structure and luminescence of powder samples, but thin films of these samples were found to be sensitive to dopant source. Systematic studies on the optical and structural properties of rf magnetron sputtered  $\text{ZnGa}_2\text{O}_4:\text{Mn}$  thin films prepared using two targets, one doped with  $(\text{CH}_3\text{COO})_2\text{Mn}$  and other with  $\text{MnO}$ , are carried out so that to control the optical and structural properties for desired application. For TDEL devices, high temperature post-deposition annealing above  $1000^\circ\text{C}$  is essential for getting good EL signal which eliminates the use of low temperature and economical substrates like glass. Significant lowering of the crystallization temperature and subsequent luminescent emission finds potential application in fabrication of ACTFEL devices using  $\text{ZnGa}_2\text{O}_4:\text{Mn}^{2+}$  phosphor thin films on low temperature substrates like glass.

## 4A.2. Experiment

Thin films of  $\text{ZnGa}_2\text{O}_4:\text{Mn}^{2+}$  were deposited on quartz substrates using rf magnetron sputtering technique. Stoichiometric powder target of  $\text{Zn}_{0.98}\text{Ga}_2\text{O}_4:\text{Mn}_{0.02}$  was synthesized by solid state reaction of  $\text{ZnO}$ ,  $\text{Ga}_2\text{O}_3$  fired at  $1350^\circ\text{C}$  for 12 hrs and subsequent reduction in  $\text{H}_2$  atmosphere for 3hrs at  $900^\circ\text{C}$  to reduce  $\text{Mn}^{3+}$  and  $\text{Mn}^{4+}$  to  $\text{Mn}^{2+}$ . Mn was doped in to the host material in two forms viz  $(\text{CH}_3\text{COO})_2\text{Mn}$  and  $\text{MnO}$  with a dopant concentration of 2 at. %. The deposition was carried out at room temperature at an rf power of 125W in an Argon ambient of 0.015 mbar varying substrate to target (S-T) distance. Thin films were also deposited at various substrate temperatures keeping the S-T

distance at 4.5 cm. The films have thickness in the range 1.3-1.6  $\mu\text{m}$  with a growth rate of 0.18 - 0.22 nm/s.

## **4A.3. Results and discussions**

### **4A.3.1.X-ray diffraction studies**

Figure 4.1 shows the XRD patterns of the films deposited (with  $(\text{CH}_3\text{COO})_2\text{Mn}$  as dopant source) at various substrate to target (S-T) distances at room temperature. The standard reflections of the host are also shown for reference [61]. All the films are polycrystalline in nature except that deposited at higher S-T distances (6.5 cm and 7.5 cm). As the S-T distance increases there is considerable variation in diffraction intensity from crystal planes of the films. At a S-T distance of 2.5 cm, the film has highest reflection intensity along (111) plane while at 3.5 cm highest diffraction intensity peak is (400) plane. At S-T distances 4.5 cm and 5.5 cm, the film has diffraction intensity maxima along the (311) direction. Beyond 5.5 cm, no traces of crystalline phases were found. Since the deposition time was kept a constant, the thickness of the films was different (in the range 1.3-1.6 $\mu\text{m}$ ). The orientation of the films mainly depends on two parameters viz background Ar pressure and S-T distance. Since background pressure is kept a constant in our work, variation in S-T distance has a profound influence on the film texturing.

An accepted model based on thermodynamic considerations, is that there is a relationship between energy supplied to the adatoms during the film growth and different growth rates on different planes. In spinels (111) and (100) are the planes with lowest surface energy [35]. At shorter S-T distances, particles impinge on the substrate with higher energy producing films with (111)

and (100) orientation. The presence of  $\text{Ar}^+$  ions and other ionic species from the target have some influence on the transfer of energy of the adatoms.

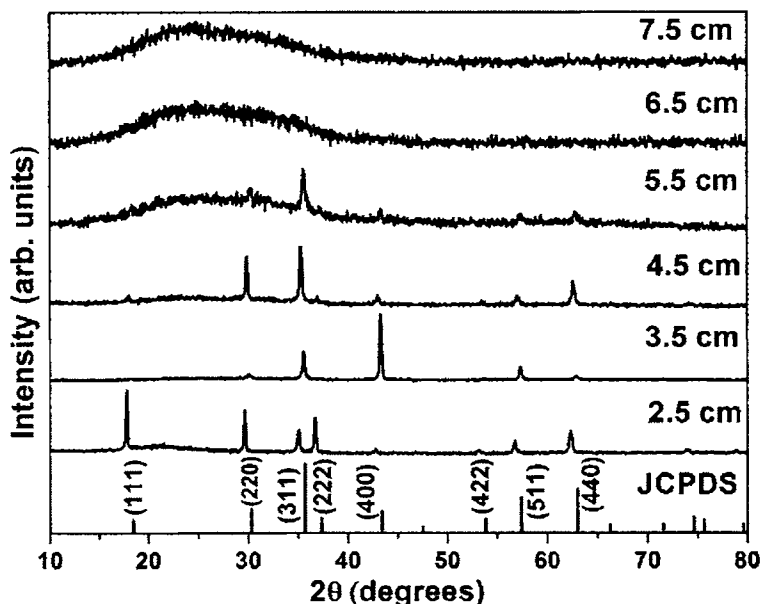


Figure 4.1 XRD patterns of  $\text{ZnGa}_2\text{O}_4:\text{Mn}$  thin films (doped with  $(\text{CH}_3\text{COO})_2\text{Mn}$ ) at different S-T distances grown at room temperature. JCPDS of  $\text{ZnGa}_2\text{O}_4$  is shown as reference.

The plasma interaction with the growing film and the energy of the adatom influence the growth of the film and hence texturing [36]. It is reported that the polycrystalline films with reflection intensity maximum along (311) plane shows excellent luminescent properties (discussed later). So in this study the S-T distance was kept at 4.5 cm. The surface energy of each plane plays an important role in texturing because surface area to volume ratio is large in thin films. If sufficient thermal energy is supplied, the films will thermodynamically grow with the densest direction.

Obviously the crystalline nature of the films at room temperature shows that the energy of the sputtered particles was high enough to orient along different direction with out any additional thermal energy and the films are polycrystalline at different S-T distances.

The x-ray diffraction (XRD) pattern of films deposited at various substrate temperatures with  $(\text{CH}_3\text{COO})_2\text{Mn}$  as the Mn source in the target are shown in figure 4.2.

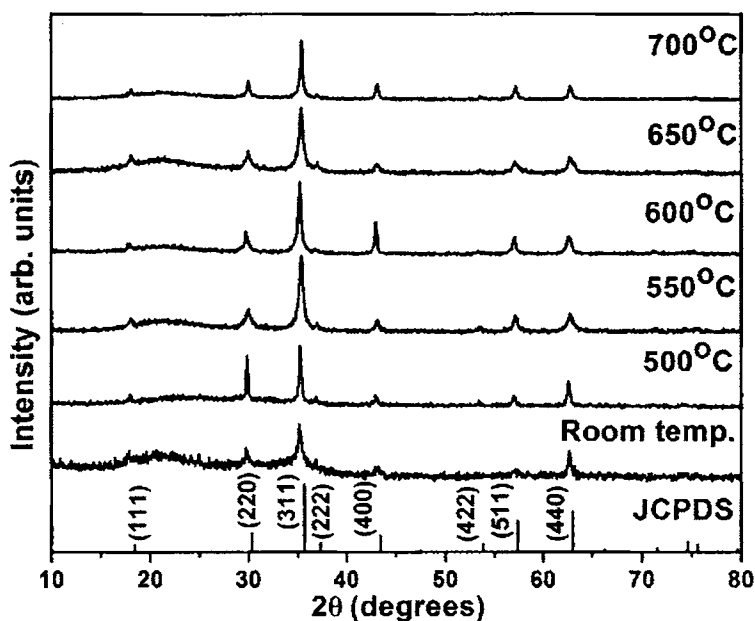


Figure 4.2 XRD patterns of  $\text{ZnGa}_2\text{O}_4:\text{Mn}$  thin films (Mn source being  $(\text{CH}_3\text{COO})_2\text{Mn}$ ) at various substrate temperatures.

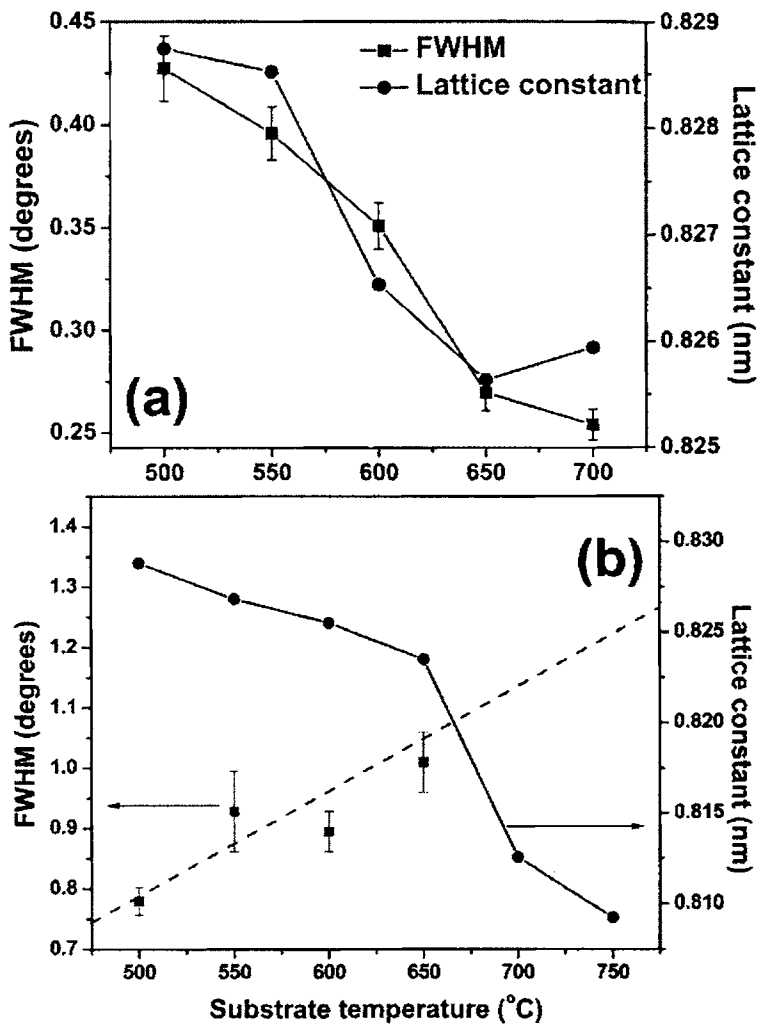


Figure 4.3 Variation of FWHM and lattice constant with substrate temperature of ZnGa<sub>2</sub>O<sub>4</sub>:Mn films deposited using (a) (CH<sub>3</sub>COO)<sub>2</sub>Mn as dopant source, (b) MnO as dopant source

The S-T distance was kept constant at 4.5 cm. All the films were polycrystalline with (311) reflection having maximum intensity. As the substrate temperature increases, the crystallinity improves which is evident from the increase in grain size. The full width at half maximum (FWHM) and lattice constant is found to decrease monotonously with substrate temperature and the variation is shown in figure 4.3a. The reduction in lattice constant gives rise to reduced cell volume. This could be due to re-evaporation of Zn at higher substrate temperatures giving rise to off-stoichiometric films with distorted structure.

Figure 4.4 shows the XRD patterns of the films deposited at various substrate temperatures, keeping the S-T distance at 4.5 cm, where the MnO was used for Mn doping in the target. Interestingly, the films exhibit entirely different structural and optical properties. The (311) peak is found to broaden with increase in substrate temperature. This broadening is expected due to the strain produced by uniform incorporation/substitution of Mn into the host lattice.

The films deposited using MnO as dopant compound, at room temperature, 500°C, 600°C and 650°C show highest reflection intensity along (311) orientation corresponding to spinel phase of ZnGa<sub>2</sub>O<sub>4</sub>. As the substrate temperature was increased to 700°C and 750°C, the films show orientation along (220) plane. In sputtering, the composition and properties of the deposited films is highly affected by 1) scattering angle differences of sputtered atoms, 2) sputtering yield of the target, 3) re-evaporation, 4) re-sputtering [31]. The factors 1, 2 and 4 mainly depend on the Ar pressure, RF power and the target composition. But in this study, the Ar pressure and RF power were kept constant through out. So it will not affect the film properties extensively. But the factor 3

is accelerated with substrate temperature. Therefore heating the substrate can give rise to Ga rich films, since the vapour pressure of Zn is high compared to Ga.

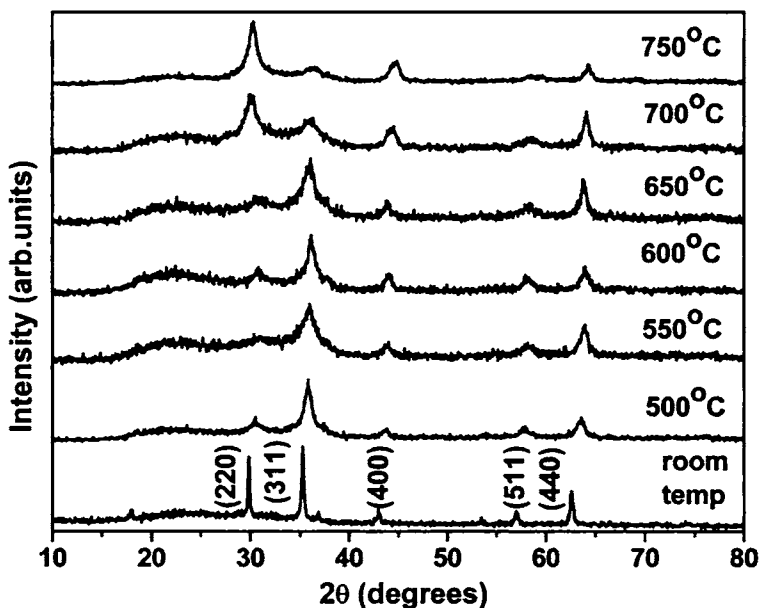


Figure 4.4 XRD patterns of ZnGa<sub>2</sub>O<sub>4</sub>:Mn thin films (doped with MnO) at various substrate temperatures.

That is Ga/Zn ratio increases with an increase in substrate temperature which will produce off-stoichiometric films with uniform Mn distribution that in turn results in inferior crystalline films orienting along different crystal planes. The variation of FWHM of the films prepared, using the target with MnO as dopant, with substrate temperature is shown in figure 4.3b. It is observed that the FWHM increases with substrate temperature exhibiting an almost linear variation. The increase in FWHM of the (311) peak explicitly shows the smaller

grain size and inferior crystallinity of the films. Similar observations were also reported by Minami *et al.* [4]. On the other hand, the lattice constant of the deposited films were found to be decreasing with substrate temperature implying the reduction of cell volume (fig 4.3b). This could be due to the increased Ga/Zn ratio as seen by XRF which will make distorted structure and results in cell volume reduction.

#### 4A.3.2. Atomic Force Microscopy

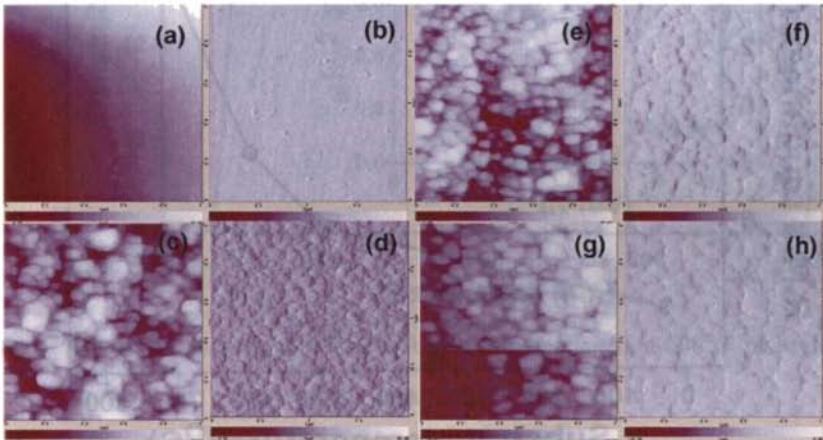


Figure 4.5 AFM images of  $\text{ZnGa}_2\text{O}_4:\text{Mn}$  film deposited (a) at room temperature, (c) at  $500^\circ\text{C}$ , (e) at  $600^\circ\text{C}$  and (g) at  $750^\circ\text{C}$  and (b), (d), (f) and (h) shows corresponding topographies of image of (a), (c), (e) and (f).

Figure 4.5 shows AFM images of  $\text{ZnGa}_2\text{O}_4:\text{Mn}$  films (doped with MnO) deposited at various substrate temperatures. The images reveal granular shaped microstructure except for that deposited at room temperature. It is observed that roughness of the films increases (figure 4.6) as temperature increases. The film deposited at room temperature shows highly smooth with rms roughness of 3

nm. This is as expected as temperature increases re-crystallization takes place there by forming granular shaped micro particles increased roughness. The roughness of the films has a direct impact on the photoluminescence emission spectra which is discussed later.

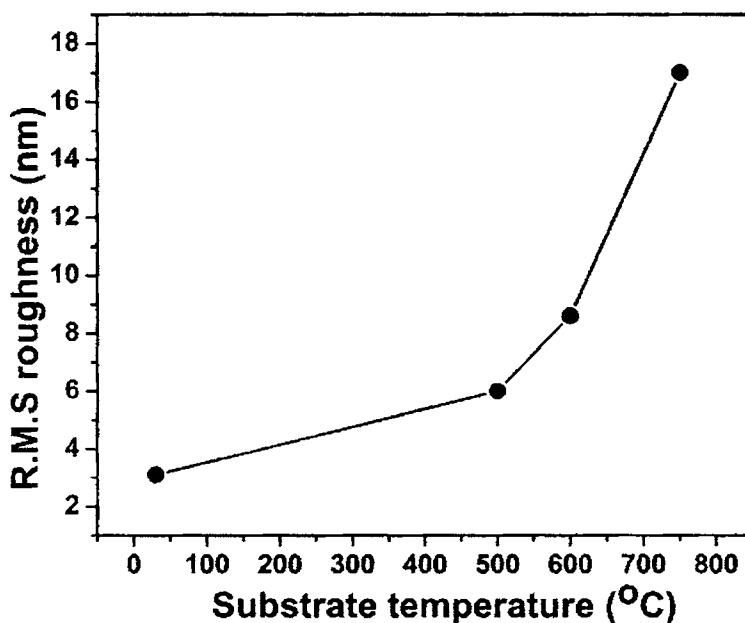


Figure 4.6 Variation in roughness of  $\text{ZnGa}_2\text{O}_4:\text{Mn}$  films (doped with MnO) with substrate temperature

### 4A.3.3. Optical Characterization

#### (a) Transmission spectra

The transmission spectrum of the film (MnO as dopant) grown on quartz substrate at 600°C is shown in figure 4.7. All the films, irrespective of the dopant source used, show almost 90% transmission in the visible region and the band

gap calculated from the  $(\alpha h\nu)^2$  vs  $h\nu$  plot (inset of fig. 5) lies in the range  $4.5 \pm 0.05$  eV which matches quite well with that of the bulk [32].

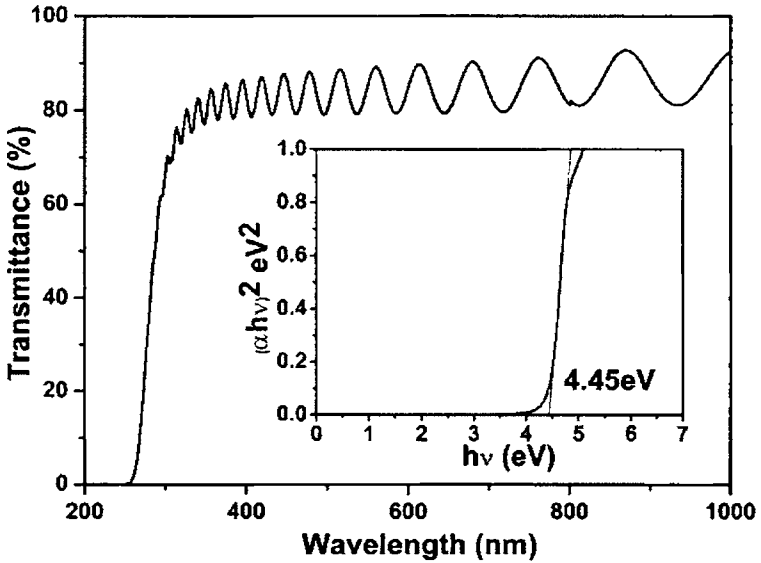


Figure 4.7 Transmission spectra of  $\text{ZnGa}_2\text{O}_4:\text{Mn}$  film deposited at  $600^\circ\text{C}$ . Inset shows  $(\alpha h\nu)^2$  versus  $h\nu$  plot.

## (b) Photoluminescence studies

Figure 4.8 shows the PL emission and excitation (inset) of the reduced target powder (doped with manganese acetate) used for sputtering. The dopant concentration used is 2 at. %. The effect of concentration has been earlier studied and it is observed that  $\text{ZnGa}_2\text{O}_4$  with 2 at. % Mn shows maximum luminescent intensity [37]. The peak emission wavelength, when excited with 300 nm uv light was 504 nm which is consistent with the results obtained by several other authors [20, 38, 39]. The emission as observed from the spectra is

an asymmetric spectrum with a shoulder at 515 nm. The emission at 504 nm is attributed to  ${}^4T_1 - {}^6A_1$  transitions in  $Mn^{2+}$  levels in which  $Mn^{2+}$  ions are located at tetrahedral site (replacing  $Zn^{2+}$ ) of the  $ZnGa_2O_4$  host.

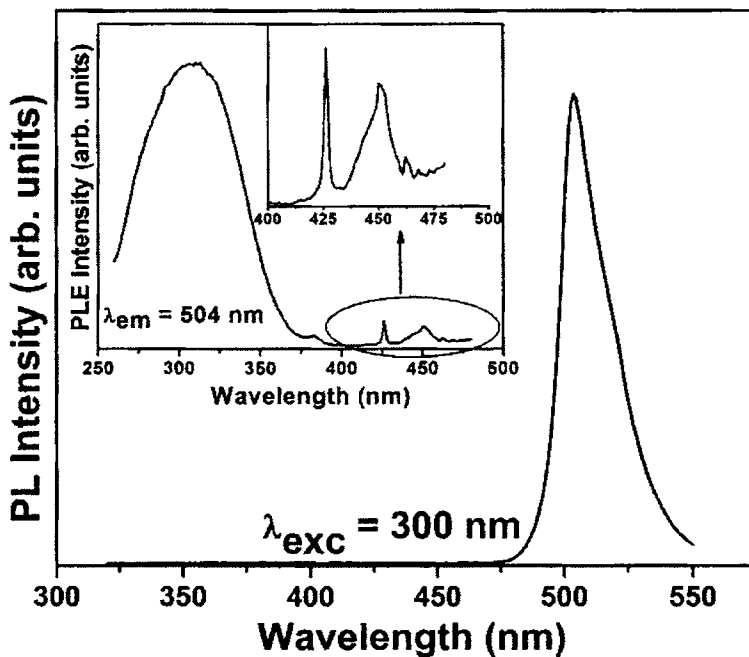


Figure 4.8 Room temperature PL emission spectra of  $ZnGa_2O_4:Mn$  (2 at. %) phosphor (doped with  $(CH_3COO)_2Mn$ ). Inset shows the corresponding excitation spectra

But Mn can also replace  $Ga^{3+}$  located at octahedral site which gives rise to shoulder at 515 nm [38]. The corresponding photoluminescent excitation spectra show a peak excitation wavelength at 300 nm which is the direct excitation of  $Mn^{2+}$  ions. The peaks at higher wavelengths (425 nm, 450 nm and 460 nm) can also be attributed to the direct excitations of  $Mn^{2+}$  ions in the

lattice. This also proves that  $\text{Mn}^{2+}$  has been incorporated in to the  $\text{ZnGa}_2\text{O}_4$  host and it replaces tetrahedral  $\text{Zn}^{2+}$  ions as well as  $\text{Ga}^{3+}$  ions.

The PL emission and excitation (inset) spectra of the target phosphor doped with MnO is shown in figure 4.9.

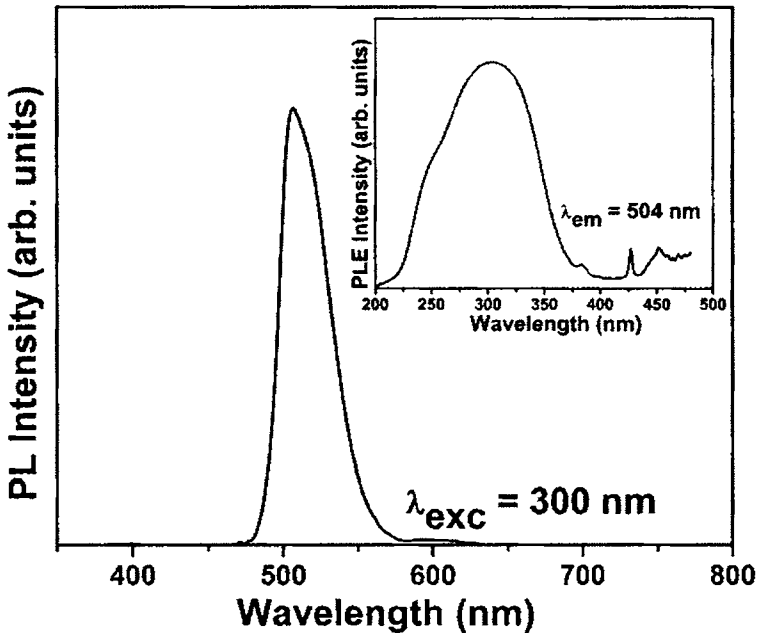


Figure 4.9 Room temperature PL emission spectra of  $\text{ZnGa}_2\text{O}_4:\text{Mn}$  (2 at. %) phosphor (doped with MnO). Inset shows the corresponding excitation spectra

The emission and excitation spectra have similar characteristics as that doped with manganese acetate. The luminescence emission band gives some information about the oxidation state of the dopant ions. Green emission at 507 nm can be attributed to the  ${}^4\text{T}_1 \rightarrow {}^6\text{A}_1$  transition in  $\text{Mn}^{2+}$  ions situated at tetrahedral site symmetry [38]. The as-prepared bulk powder phosphors, before

reduction, did not exhibit intense green emission. This is due to the fact that at high temperatures there is a strong chance for the oxidation of  $\text{Mn}^{2+}$  in to  $\text{Mn}^{3+}$  and in order to balance the charge it will migrate to octahedral site. This  $\text{Mn}^{3+}$  will absorb the green emission from the  $\text{Mn}^{2+}$  ions at tetrahedral position due to charge transfer between them [34]. The presence of  $\text{Mn}^{2+}$  at tetrahedral site is essential for an efficient luminescence from the phosphor. The green PL emission after reduction, in both phosphor targets confirms that Mn is incorporated in to the host lattice as  $\text{Mn}^{2+}$  at tetrahedral site.

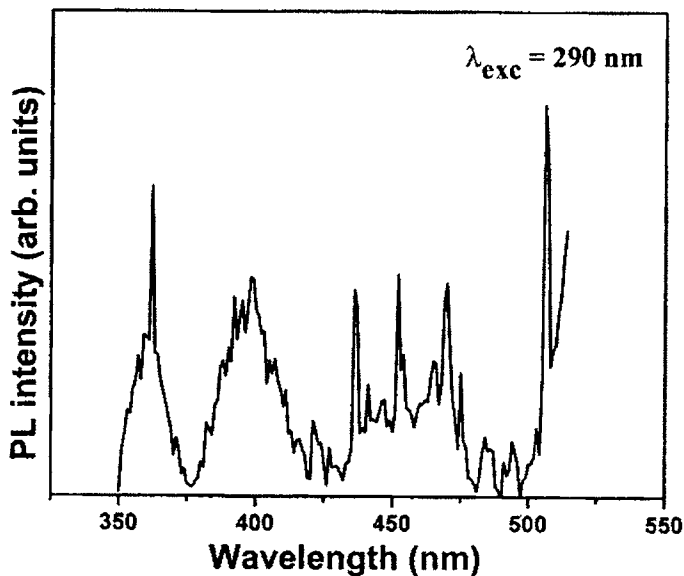


Figure 4.10 Room temperature PL emission spectra of  $\text{ZnGa}_2\text{O}_4:\text{Mn}$  thin films [( $\text{CH}_3\text{COO}$ )<sub>2</sub>Mn as dopant source].

The films deposited using the phosphor with ( $\text{CH}_3\text{COO}$ )<sub>2</sub>Mn as dopant source did not show any luminescence (figure 4.10 shows the high level of

noise) even though enough thermal energy was supplied during film growth via substrate heating. The spectrum doesn't show any characteristics of  $\text{ZnGa}_2\text{O}_4:\text{Mn}$  phosphor. In order to probe whether the luminescence was killed by the presence of  $\text{Mn}^{3+}$  ions, the films were post-annealed in  $\text{H}_2$  atmosphere at  $800^\circ\text{C}$  to reduce  $\text{Mn}^{3+}$  ions, if any in the samples. Still no luminescence could be observed from the films. This points towards improper/no incorporation of Mn into the host lattice resulting in absence of luminescence in the films deposited using  $(\text{CH}_3\text{COO})_2\text{Mn}$  as dopant source. The reduction in FWHM (Fig 4.3a) also implies that substrate heating contributed only towards improvement of crystallinity of the films.

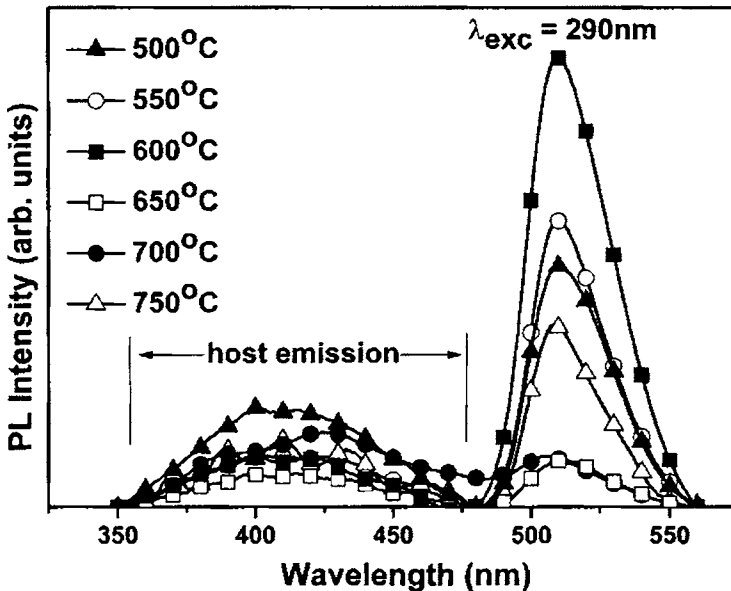


Figure 4.11 Room temperature PL emission spectra of  $\text{ZnGa}_2\text{O}_4:\text{Mn}$  thin films (MnO as dopant source) at various substrate temperatures.

The films deposited with MnO as the dopant source in the target gives green emission similar to the bulk phosphor. Figure 4.11 shows the room temperature PL emission spectra of ZnGa<sub>2</sub>O<sub>4</sub>:Mn thin films deposited at various substrate temperatures. All the films gave green emission band, with peak at 508nm attributed to the <sup>4</sup>T<sub>1</sub> → <sup>6</sup>A<sub>1</sub> transition of tetrahedrally coordinated Mn<sup>2+</sup> ions. The spectra also show a broad host emission band peaking at 421 nm due to the self-activated luminescence. In ZnGa<sub>2</sub>O<sub>4</sub>, Ga<sup>3+</sup> acts as sensitizer [21].

The mechanism of luminescence in ZnGa<sub>2</sub>O<sub>4</sub>:Mn<sup>2+</sup> is identified as non-radiative resonant energy transfer with electric dipole-dipole interaction between sensitizer (Ga<sup>3+</sup>) and activator (Mn<sup>2+</sup>) ions as there is significant overlap of the activator absorption and sensitizer emission [23]. The film deposited at room temperature, though polycrystalline in nature, didn't exhibit any luminescence. But the films deposited at and above 500°C exhibit green emission which is a clear indication of the diffusion of Mn<sup>2+</sup> ions at higher temperatures. As the substrate temperature increases, PL emission intensity increases, reaches a maximum for 600°C and then decreases at higher substrate temperatures.

The luminance properties of phosphors depend strongly on grain size, Zn/Ga ratio and crystal structure. Luminescence efficiency of high voltage phosphors decrease with reduced grain size due to photon absorption and scattering. For low voltage phosphors like ZnGa<sub>2</sub>O<sub>4</sub>, high luminescent efficiency is observed with reduced grain size due to larger surface area per unit volume [31]. Moreover, it has been reported that slightly Zn deficient films exhibit superior luminescent characteristics due to enhanced Mn<sup>2+</sup> substitution at Zn tetrahedral sites [23]. In the present work, FWHM is observed to increase with

substrate temperature (evident from figure 4.3b) and subsequent reduction in grain size enhances luminescence. In addition, Zn/Ga ratio of the films reduces with substrate temperature, vapor pressure of Zn being higher compared to Ga. Excess Ga sites also serve as activators in these films. Beyond 600°C, growth along other crystal planes is promoted reducing the PL intensity, in spite of reduced grain size. In the case of substrate temperatures above 650°C, the (311) spinel orientation is lost. It has been reported that the films with (311) orientation show superior luminescence characteristics than any other orientation [34]. Moreover, the films grown at higher substrate temperature are highly Zn deficient favoring the formation of monoclinic  $\beta$ -Ga<sub>2</sub>O<sub>3</sub> phase which will again reduce the PL intensity.

The PL emission intensity and peak emission wavelength of the host shows random variation with temperature. The luminescent intensity and peak emission wavelength of the host relates to Zn/Ga ratio and Ga-O ligand strength [39]. As temperature increases, host emission decreases up to 650°C and above 650°C it varies at random. This is due to the fact that above 650°C, there is a considerable variation in the crystal structure of the host and there is also considerable re-evaporation of Zn at temperatures above 650°C [39]. Due to the increase in density of Zn vacancies, at high temperatures, Ga<sup>3+</sup> migrates from octahedral sites to tetrahedral sites forming distorted octahedral structure in the spinel [21]. This will considerably alter the host emission wavelength, intensity and corresponding transfer of energy resulting in considerable variation of luminescence output.

### 4A.3.4 The CIE Coordinates

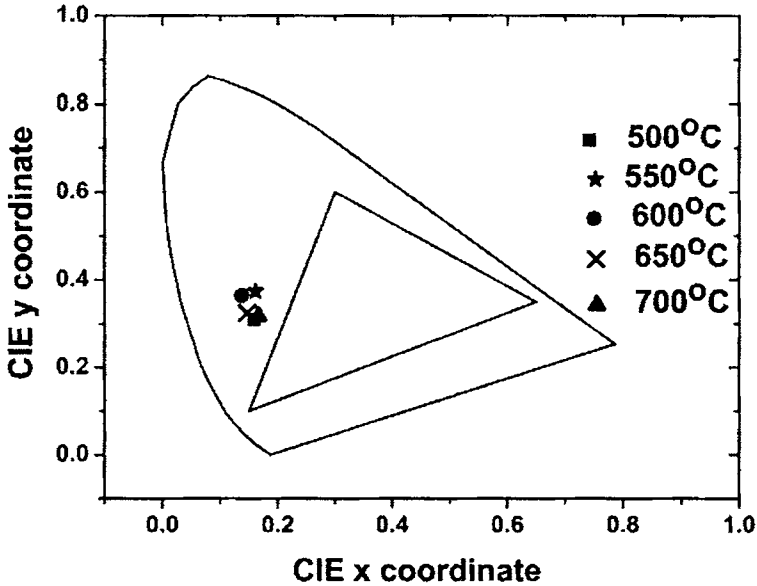


Figure 4.12 CIE coordinates of the PL emission spectra of  $\text{ZnGa}_2\text{O}_4:\text{Mn}$  thin films

The CIE coordinates of the PL emission spectra is shown in the figure 4.12. The coordinates lie in the bluish-green region of the coordinate diagram. The bluish color corresponds to contribution from the host.

## Conclusion

In summary Mn doped zinc gallate phosphor have been synthesized using different Mn precursors namely, manganese acetate and manganese oxide. The influence of these precursors on structural and optical properties of thin films prepared using targets ( $\text{Zn}_2\text{GaO}_4:\text{Mn}$ ), one doped with  $(\text{CH}_3\text{COO})_2\text{Mn}$  and other with MnO has been investigated. Even though the powder targets do not

show any variation in structural and optical characteristics, thin films prepared from these targets show different characteristics. FWHM of the x-ray diffraction peak (311) is found to decrease with substrate temperature when the dopant source was (CH<sub>3</sub>COO)<sub>2</sub>Mn but the films deposited using MnO as dopant source in the target, FWHM increases with substrate temperature. The use of MnO results in uniform substitution of Mn in the host lattice which in turn gives rise to broadening of FWHM. No luminescence was observed when acetate was used as dopant implying the fact that Mn is not incorporated in to the host lattice, in the film even though the target showed excellent green emission. In the sight of structural and optical characteristics it is concluded that manganese oxide is better choice of doping Mn rather than manganese acetate.

## **PART B**

---

### **Growth and Characterization of RF magnetron sputtered $\text{Zn}_2\text{GeO}_4:\text{Mn}^{2+}$ thin films**

---



## **4B.1. Introduction**

Zn<sub>2</sub>GeO<sub>4</sub> doped with Mn is known to emit green light up on UV excitation. Zn<sub>2</sub>GeO<sub>4</sub> has rhombohedral structure, similar to Zn<sub>2</sub>SiO<sub>4</sub>, with Zn ions at tetrahedral sites and Ge at octahedral sites and have a wide band gap of 4.68 eV [12, 13]. Undoped Zn<sub>2</sub>GeO<sub>4</sub> phosphor is a native defect phosphor and exhibits white luminescence under UV excitation [17]. Mn<sup>2+</sup> substitutes for Zn<sup>2+</sup> in the host and a green emission is obtained via a transition between <sup>4</sup>T<sub>1</sub>-<sup>6</sup>A<sub>1</sub> levels of Mn<sup>2+</sup>. Thin films of Zn<sub>2</sub>GeO<sub>4</sub> have been deposited using pulsed laser deposition (PLD) [11], RF magnetron sputtering [12-14] etc and they find application as CL phosphor and EL phosphor. Thick dielectric electroluminescent (TDEL) and alternating current thin film electroluminescent (ACTFEL) devices with Zn<sub>2</sub>GeO<sub>4</sub> as active layer has also been developed [14, 15]. This phosphor has also been investigated for integrated optics applications [17].

Unfortunately, one of the fundamental problems of oxide thin-film phosphors is their inferior luminous efficiency and brightness when compared to their powder form. The inferior luminescent properties are caused by internal reflection from the planar interface, the so-called “light-piping effect,” and inferior crystallinity [3, 40]. The luminescent output can be improved by either increasing the light-scattering centers by surface modification or by reducing defects after post-annealing at high temperatures [3, 41]. In most studies post deposition annealing (RTA, hydrothermal or furnace anneal) is carried out to improve the luminescent (PL, EL or CL) characteristics of the phosphor layer [11-15]. The high crystallization temperature of oxide phosphors also prevent them from being deposited on cheaper glass substrates. Thick dielectric

substrates like BaTiO<sub>3</sub> and high temperature post deposition annealing is usually employed to improve crystalline quality of the thin film. However Lewis *et al.* [12] has developed TFEL devices using Zn<sub>2</sub>GeO<sub>4</sub>:Mn as active layer on glass substrates through RTA treatments. The crystallization temperature of Zn<sub>2</sub>GeO<sub>4</sub>:Mn is found to be 650°C [13] and better crystalline films are obtained only after post-deposition annealing of the films. The inferior crystallinity of the as-deposited, polycrystalline thin-film phosphors are mostly due to a limitation of the amorphous like substrates used. Moreover, it is hard to reduce the defect density in phosphor films by a post-annealing process at high temperatures due to low softening temperature of the glass substrate. One of the possible methods to obtain polycrystalline thin-film phosphors with enhanced crystallinity is by growing phosphor layer over a highly crystallized buffer layer which is grown on the amorphous substrate. The ZnO thin film is chosen as the buffer layer because it is relatively easy to grow a high quality crystalline film.

In this work, the dependence of Zn<sub>2</sub>GeO<sub>4</sub>:Mn thin film growth on deposition parameters like RF power and substrate temperature and the influence of ZnO buffer layer on the structural and optical characteristics of Zn<sub>2</sub>GeO<sub>4</sub>:Mn thin films has been investigated.

## 4B.2. Experiment

Thin films of Zn<sub>2</sub>GeO<sub>4</sub>:Mn<sup>2+</sup> were deposited on quartz substrates by RF magnetron sputtering (2" gun). The target used was Zn<sub>2</sub>GeO<sub>4</sub>:Mn<sup>2+</sup> powder prepared by the solid state reaction of constituent oxides. The starting materials, namely ZnO (99.99%, Alfa Aesar), GeO<sub>2</sub> (99.99%, Alfa Aesar) and MnO (99.99%, Alfa Aesar), were mixed stoichiometrically in ethanol medium and

then fired at 1200°C for 12hrs. The doping concentration was fixed at 2 at. %. The deposition was carried out on to the substrate kept at 4.5cm away from the target in an Ar ambient of 0.015 mbar at various RF powers for one hour. The ZnO buffer layer (~ 100 nm) was deposited at a substrate to target distance of 4.5 cm in an Ar ambient of 0.015mbar at 400°C for 3 minutes. The RF power was kept at 100 W (28 W/cm<sup>2</sup>). The phosphor layer was then deposited on ZnO/Quartz at various substrate temperatures varying from room temperature to 700°C. The thickness of the samples was measured using Dektak 6M stylus profiler and the average growth rate of phosphor layer was found to be 0.2nm/s. The crystal structure of the films was analyzed using Rigaku x-ray diffractometer using Cu K<sub>α</sub> radiation (1.5414Å). The transmission spectra were recorded using JASCO V-570 spectrophotometer. Room temperature photoluminescence (PL) emission and excitation spectra (PLE) were recorded using Jobin Yvon Fluoromax-3 spectrometer equipped with a 150W xenon lamp. The surface morphology of the films were analyzed using scanning electron microscope (SEM).

## **4B.3. Results and discussions**

### **4B.3.1 X-ray diffraction studies**

The XRD patterns of  $Zn_2GeO_4:Mn^{2+}$  films deposited on quartz substrates for various RF powers are shown in figure 4.13. The substrate was heated to 650°C prior to deposition. The films deposited at the RF powers 100W and 125W did not show any crystallinity. But when the RF power was raised to 150W, polycrystalline films were grown. The peaks of x-ray diffraction pattern

matched well with the standard reflections of the rhombohedral  $\text{Zn}_2\text{GeO}_4$  host [62].

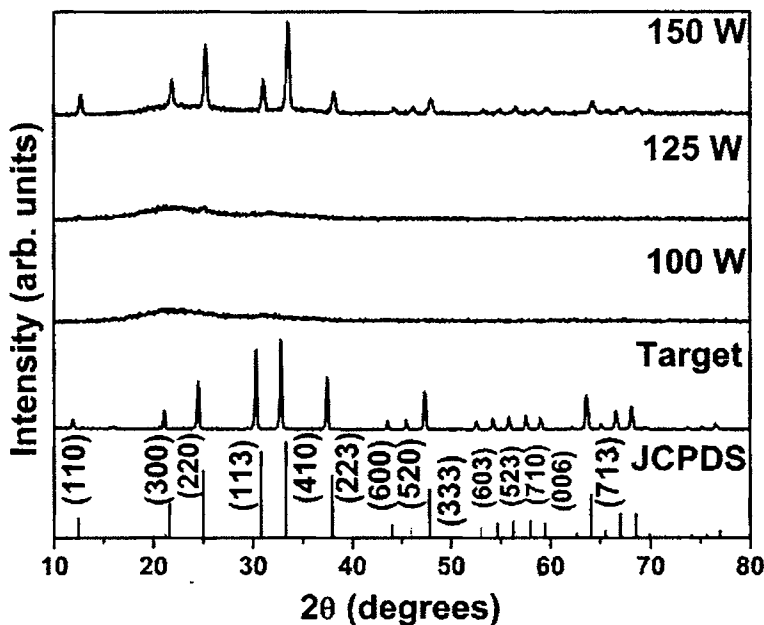


Figure.4.13. xrd patterns of  $\text{Zn}_2\text{GeO}_4\text{:Mn}$  thin films deposited at  $650^\circ\text{C}$  on quartz substrates at various RF powers. The JCPDS of  $\text{Zn}_2\text{GeO}_4$  host and xrd pattern of target ( $\text{Zn}_2\text{GeO}_4\text{:Mn}$ ) is given for reference.

In sputtering, the composition and properties of the deposited films is highly affected by 1) scattering angle differences of sputtered atoms, 2) sputtering yield of the target, 3) re-evaporation, 4) re-sputtering [25]. The factors 1, 2 and 4 mainly depend on the Ar pressure, RF power and the target composition and factor 3 depends on substrate temperature. Since background Ar pressure and target composition are constant through out this experiment, RF power and substrate temperature has profound influence on the crystalline

quality of the films. The presence of  $Ar^+$  ions and other ionic species from the target also have some influence on the transfer of energy of the adatoms. The surface energy of each plane plays an important role in texturing because the surface area to volume ratio is large in thin films. If sufficient thermal energy is supplied, the films will thermodynamically grow with the densest direction. Here, polycrystalline films could be grown only when the RF power was raised to 150 W at a substrate temperature 650°C. It should be inferred that under these conditions, the sputtered particles had the sufficient thermal energy to favour the film growth thermodynamically. Interestingly, crystallinity couldn't be observed for the films deposited at lower substrate temperatures (500°C, 600°C) or at lower RF powers (100 W, 125 W).

The XRD patterns of ZnO buffer layer grown at 400°C is shown in figure 4.14. The rf power used was 100 W. Inset shows variation in FWHM of (002) peak of ZnO with annealing temperature after deposition at 400°C. A minimum FWHM was observed for annealing temperatures 600°C and 650°C showing that better crystalline films are obtained at these temperatures.

Figure 4.15 shows the XRD patterns of  $Zn_2GeO_4:Mn$  thin films deposited on ZnO/quartz substrate at various substrate temperatures. The oriented growth of ZnO buffer layer along the (002) plane is observed in all cases. At 500°C and 550°C, the reflections from the  $Zn_2GeO_4:Mn$  layer were absent. As the temperature reached 600°C, reflection from (220) plane of  $Zn_2GeO_4$  is observed and a sudden increase in the reflection intensity takes place when the substrate temperature is 650°C. At 700°C polycrystalline film is formed. All these reveal that the crystalline ZnO surface presents a better platform for thin film growth rather than an amorphous substrate.

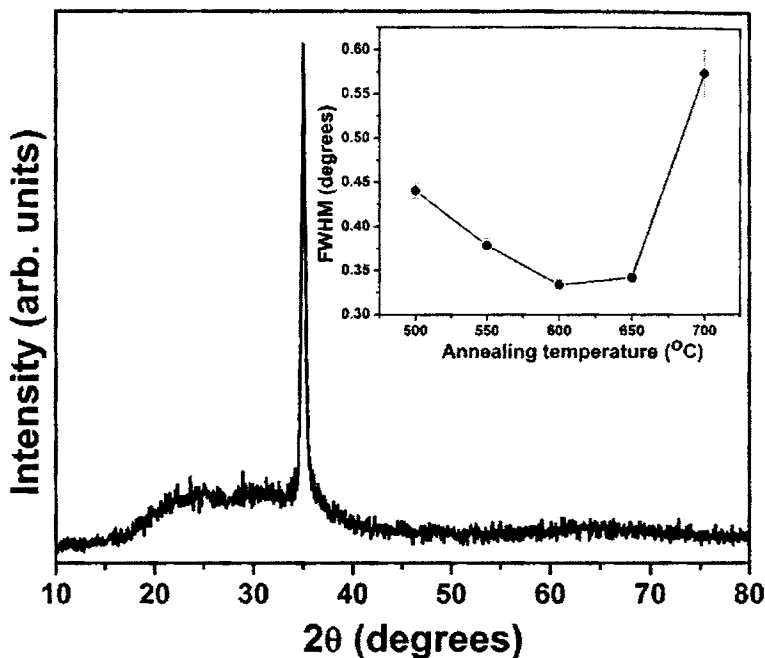


Fig.4.14. XRD patterns of ZnO thin film deposited at 400°C; RF Power = 100 W. Inset shows variation in FWHM for the film deposited at 400°C and then annealed at various temperatures.

When a film is grown on a crystalline surface, the resulting film may be influenced by the initial surface. If the underlying crystal structure of the film/substrate is compatible with that of the phosphor film, and if the temperature is sufficiently high to enable reorganization of the deposited atoms, one can enhance the structural properties of the latter. Or else, along with energy of sputtered material, additional thermal energy is needed to crystallize the film.

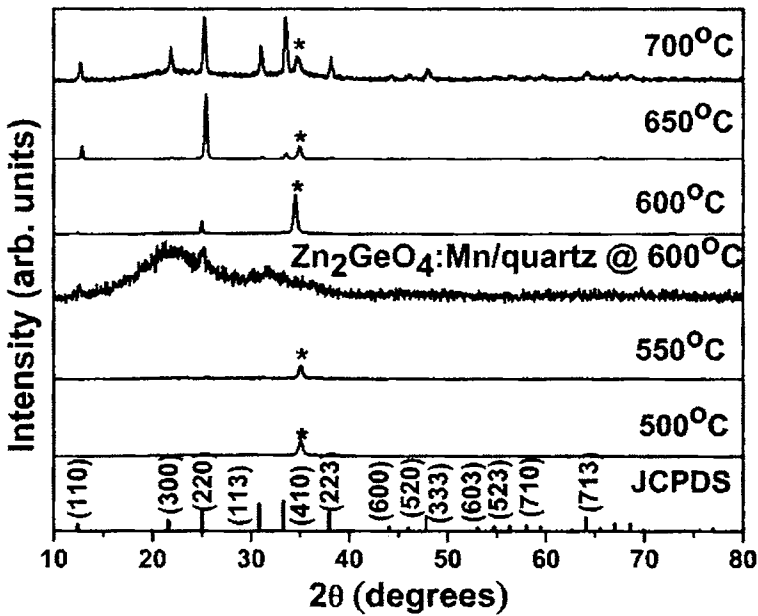


Figure.4.15. xrd patterns of  $Zn_2GeO_4:Mn$  thin films deposited on  $ZnO$ /quartz substrates at various substrate temperatures and on amorphous quartz substrate at  $600^\circ C$ .

\* represents (002) plane of  $ZnO$ .

Here, the presence of the  $ZnO$  buffer layer assists the formation of highly oriented  $Zn_2GeO_4:Mn^{2+}$  films even at a substrate temperature of  $600^\circ C$ . The growth of (220) plane at  $600^\circ C$  and  $650^\circ C$  could be due to unfavourable interfacial energy between (410) plane of  $Zn_2GeO_4$  and (002) plane of  $ZnO$  while at  $700^\circ C$ , the films are highly poly crystalline due to relaxation of  $ZnO$  buffer layer at higher temperature. At this point, it is worth mentioning that films deposited without the  $ZnO$  buffer have quite different structural properties. The full width at half maximum (FWHM) of the (220) peak of  $Zn_2GeO_4:Mn$  was found to be  $0.23^\circ$  and  $0.29^\circ$  with and without the buffer layer respectively. This

is suggestive of the fact that the presence of a highly crystallized buffer layer also enhances the crystallinity of the phosphor films and helps in film texturing.

### 4B.3.2 Band gap

The band gap of the films was determined using the Tauc plot  $[(\alpha h\nu)^2$  vs  $h\nu$  curve]. Figure 4.16 represents the Tauc plot of the  $\text{Zn}_2\text{GeO}_4:\text{Mn}$  films grown at  $650^\circ\text{C}$  with and without  $\text{ZnO}$  layer.

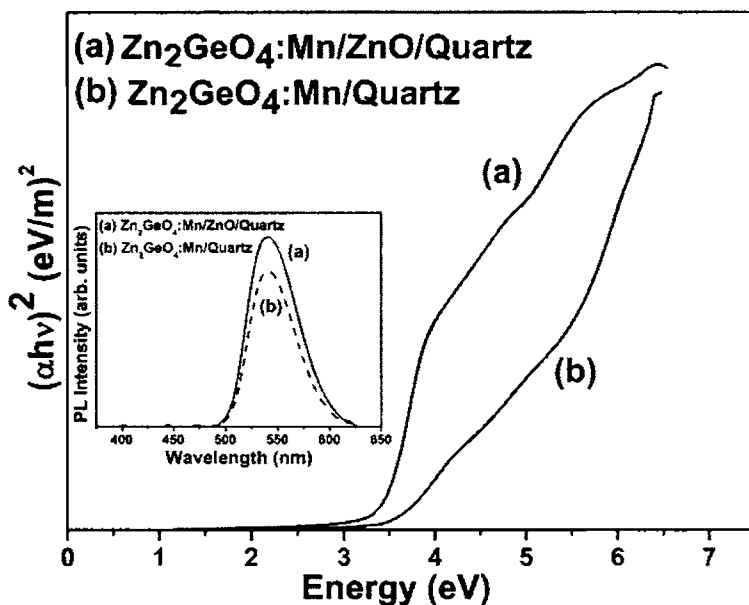


Fig.4.16.  $(\alpha h\nu)^2$  vs  $h\nu$  plot (Tauc plot) of  $\text{Zn}_2\text{GeO}_4:\text{Mn}$  thin film deposited on a)  $\text{ZnO}/\text{quartz}$  and b) amorphous quartz substrate. Inset shows corresponding PL emission from a)  $\text{Zn}_2\text{GeO}_4:\text{Mn}/\text{ZnO}/\text{quartz}$  and b)  $\text{Zn}_2\text{GeO}_4:\text{Mn}/\text{quartz}$  films.

The film without the  $\text{ZnO}$  buffer layer has quite discrete sub-band gap absorption at 3.5 eV in addition to the band to band absorption of the host at 180

4.57 eV. But for the film grown with ZnO buffer layer, the curve exhibits a linear behavior with a different slope at energies above the sharp sub-band gap absorption (at 3.5 eV) attributed to phonon-assisted absorptions. The sub-band absorption is due to the formation of oxygen vacancies, the presence of which is intrinsic in film deposition process. Moreover, the evaporation of Zn at high substrate temperature increases Zn defects in the film which in turn generate oxygen vacancies via  $Ge^{3+}$  migration to vacant tetrahedral Zn sites, to avoid charge imbalances (which is observed in bulk phosphor also). The increased defect density in the  $Zn_2GeO_4:Mn/ZnO$  films improves the spectral overlap between the sub band states and excited levels of  $Mn^{2+}$ . This enhances the resonant energy transfer from the host to the activator thereby increasing the intensity of the green luminescent emission.

### **4B.3.3 Scanning electron microscopy**

The microstructure of the deposited films was analyzed using scanning electron microscope (figure 4.17). Film deposited on bare quartz substrate at 650°C and that on ZnO/quartz substrate at 700°C shows similar surface morphology with octahedral shaped particles. Film deposited on ZnO/quartz substrate at 500°C and 600°C were smooth. But the film deposited at 650°C shows coffee bean shaped particles which is quite different morphology compared to all other films. For high voltage phosphors, generally luminance intensity falls with reduced grain size, due to photon scattering and absorption. Further more, roughness of the film surface also enhances luminance output. Here films deposited on bare quartz and on ZnO/quartz at 700°C are rough than that deposited on ZnO/quartz substrate at 650°C.

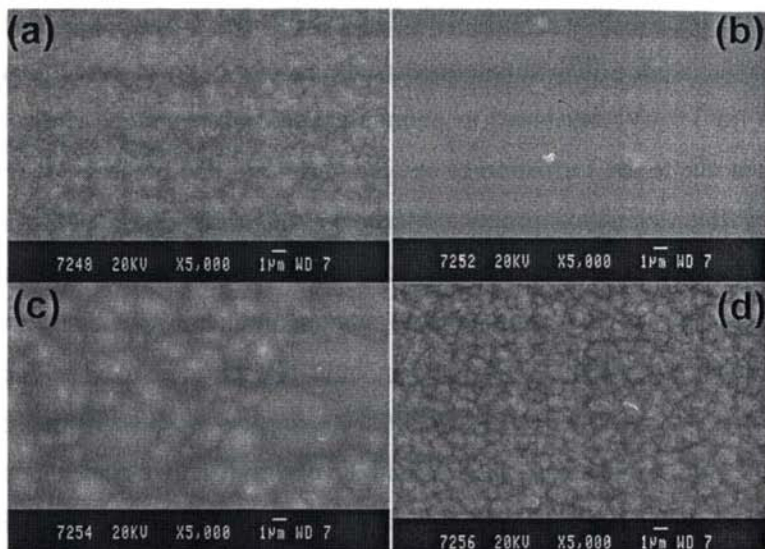


Figure.4.17. SEM images of Zn<sub>2</sub>GeO<sub>4</sub>:Mn thin films deposited (a) on bare quartz substrate at 650°C, on ZnO/quartz substrate at (b) 500°C, (c) 650°C and (d) 700°C

But grain size of film grown at 650°C is higher than the other films grown on quartz at 650°C and ZnO/quartz at 700°C. Enhanced luminance output was observed from the film grown on ZnO/quartz at 650°C (discussed below) which also resulted in enhanced crystalline quality of the film. At 700°C, the increased thermal energy causes surface boiling of the buffer layer significantly. Consequently the chemical loss from the buffer layer prevents grains from merging, and thus surface morphology of the film looks as if there is no buffer layer at all.

### **4B.3.4 Photoluminescence studies**

The PL emission intensity varies drastically with substrate temperature (figure 4.18) which also depicts the fact that PL intensity highly depends on crystallinity of the films. The maximum intensity is observed for that deposited at 650°C. The emission at 540 nm corresponds to transition from  ${}^4T_1 - {}^6A_1$  of  $Mn^{2+}$  levels with tetrahedral configuration.  $Mn^{2+}$  is supposed to replace tetrahedral Zn in  $Zn_2GeO_4$ . The crystal field has profound effect on the luminescence of  $Mn^{2+}$  in crystals. As crystalline  $Zn_2GeO_4$  is only formed at a substrate temperature of 650°C, the luminescence intensity peaks for the film deposited at this critical temperature. However at 700°C, the luminescent intensity decreases. Apart from crystallinity the composition of the films also influence the luminescent intensity of the films. Since the vapour pressure of Zn is high, at elevated substrate temperatures, there is severe chance for the re-evaporation of Zn and in most cases the films will be Zn deficient. This will certainly affect the crystal field of  $Mn^{2+}$  which influences the luminescent intensity. The mechanism of luminescence is identified as a resonant transfer from a sub-band state which lies nearly 1 eV below the conduction band to  $Mn^{2+}$  levels. Any perturbation of this level will seriously affect the luminescent intensity. As Zn vacancies are more at higher substrate temperature, this sub band state is perturbed more, there by reducing the resonant energy transfer and luminescence output.

The PLE spectra of the films are shown in the figure 4.19. The spectra show a blue shift with respect to increase in substrate temperature. In the bulk phosphor the excitation corresponding to 540 nm emission is 332 nm. For the films deposited at 600°C, PLE peak excitation wavelength is 332 nm. However

inferior crystalline nature of the film reduced the luminescence out put. As we increase the temperature, more Zn vacancies are formed and PLE is blue shifted to 308 nm and for films deposited at 700°C the PLE peak excitation wavelength is at 303 nm.

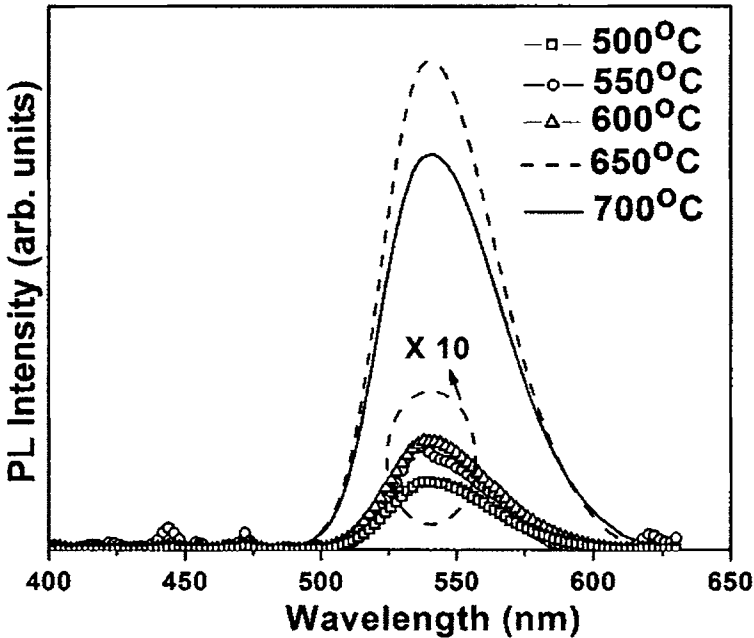


Figure.4.18. Room temperature PL emission spectra of  $\text{Zn}_2\text{GeO}_4:\text{Mn}$  thin films deposited on ZnO/quartz substrates at various substrate temperatures.

This excitation is consistent with the sub-band absorption observed from Tauc plot indicating that resonant transfer of energy occurs from sub-band states. This blue shift is direct consequence of reduced Zn/Ge ratio which will considerably increase the defect density of the host.

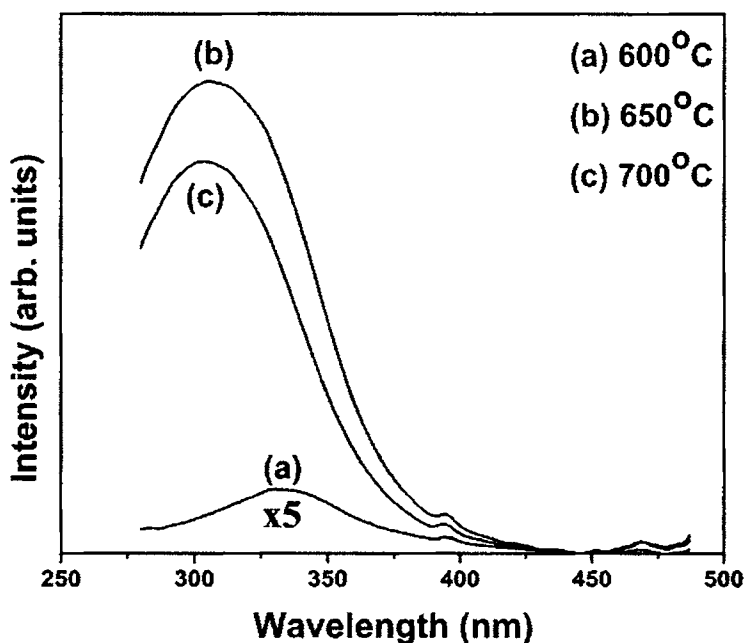


Figure.4.19. PLE spectra  $Zn_2GeO_4:Mn$  thin films deposited on ZnO/quartz substrates at various substrate temperatures.

## Conclusion

In summary,  $Zn_2GeO_4:Mn$  thin films were deposited on quartz substrates at various substrate temperatures with out any post deposition annealing. The effect of RF power, substrate temperature and ZnO buffer layer on structural and luminescent characteristics of the films was studied in detail. At 650°C and RF power of 150 W, polycrystalline films could be grown on quartz substrates. Texturing along (220) direction is observed for films grown on ZnO/Quartz. Sharp sub band absorption at 3.5 eV and band edge absorption at 4.57 eV is

observed for film grown on bare quartz substrate while only strong sub band absorption was observed for film grown on ZnO/Quartz substrate indicating higher defect density in latter films. Photoluminescent emission was found to be enhanced for the film deposited on ZnO/Quartz substrate, at 650°C, than that deposited on bare quartz substrate. PLE was found to blue shift with substrate temperature.

## **PART C**

---

### **Pulsed Laser Deposition of $\text{Y}_2\text{O}_3\text{:Eu}$ thin films**

---



## 4C.1. Introduction

Thin films of  $Y_2O_3$  has been of a great research interest over last few years due to its wide application potential such as metal insulator-semiconductor (MIS) diodes, metal-oxide semiconductor capacitors (MOS), Dynamic random access memory (DRAM) gate dielectric because it possess a wide band gap (5.8 eV), high dielectric constant [42-46] and high melting point (2410°C). It has also been used as a dielectric layer in thin film electroluminescent (TFEL) displays [47]. However in fluorescent lamps and cathodoluminescent displays, Eu doped  $Y_2O_3$  acts as a phosphor emitting red light. In energy saving lamps it is used as a powder with a grain size of several microns, combining high quantum efficiency, a proper emission wavelength, and a large absorptivity for the exciting radiation. Enhanced emission intensity and efficiency has been observed via co-doping  $Y_2O_3:Eu$  with Zn, Gd, Li, La [43-46, 48]. Blue green and red cathodoluminescence were also observed from doped  $Y_2O_3$  thin films prepared using sol-gel process making it a suitable material for electroluminescent and cathodoluminescent phosphor [49]. Thick dielectric electroluminescent devices were also fabricated on ceramic substrates using  $Y_2O_3:Mn$  as active layer [50]. In  $Y_2O_3:Eu^{3+}$ , the mechanisms that are governing the absorption which also gives rise to red emission are 1) direct excitation of the  $Eu^{3+}$  ion, 2) excitation via a charge-transfer state between the Eu ion and neighboring O ions or 3) excitation via the  $Y_2O_3$  host lattice [51]. In  $Y_2O_3:Eu$ , emission consists of large number of lines ranging from 580 – 700 nm and in general these lines can be assigned to  $^5D_0 - ^7F_J$ ,  $J=0,1,2,3$  transitions. Each of these transitions is partially resolved in to various  $m_J$  transitions. All of these emission lines corresponds to inner f-f transitions and are electric dipole

forbidden. From the emission spectrum, one can speak about local crystal environment of  $\text{Eu}^{3+}$  ion, especially from the relative intensity ratio of  ${}^5\text{D}_0 - {}^7\text{F}_1$  and  ${}^5\text{D}_0 - {}^7\text{F}_2$  emission lines. Because the intensities of these transitions highly depend on local crystal environment in different ways [52]. The  ${}^5\text{D}_0 - {}^7\text{F}_1$  transition is electric dipole forbidden and intensity of this line can be attributed to magnetic dipole operator and almost insensitive to local environment. But  ${}^5\text{D}_0 - {}^7\text{F}_2$  transition, by mixing with higher allowed transition, is electric dipole allowed and intensity of which being hypersensitive to local environment (ie, the local electric field and local symmetry) [53].

Pulsed laser deposition (PLD) has been widely used to deposit high quality thin films. Single crystal substrates like sapphire,  $\text{LaAlO}_3$  (for epitaxial growth), Si etc has been used to grow high quality crystalline thin films [40, 54-56]. More over thin films offer better adhesion to solid surface, higher lateral resolution, better thermal stability and reduced out-gassing compared to phosphors in bulk powder form. But lower brightness and efficiency of thin films, due to internal reflection, small interaction volume and absorption of light by substrate material, are rather its negatives. Further more the structural and optical characteristics of thin films grown, highly depends on the properties of substrate chosen. Therefore, usually single crystalline substrates are used for phosphor thin film deposition. On the other hand these single crystalline substrates are expensive which prevents commercialization of devices fabricated on them. So it is advisable to use cheaper amorphous substrates like glass or fused silica for deposition of thin film phosphors.

In the present work  $\text{Y}_2\text{O}_3:\text{Eu}^{3+}$  thin films have been deposited on amorphous fused silica substrates using pulsed laser deposition and the films has

been characterized structurally and optically.  $Y_2O_3$  thin films were deposited using rf magnetron sputtering at various rf powers. But sputtering rate was very low (average of 0.035 nm/sec) so that we could get a 100-150 nm thick film when sputtered in the range 150 -200 W rf power (maximum available power in the rf unit) at a substrate distance of 4 cm. Therefore in order to get thicker films sputtering has to be performed for quite long time which was not feasible. Laser ablation technique has been found to have higher growth rate and hence PLD was used to grow  $Y_2O_3:Eu$  thin films.

## **4C.2. Experiment**

Thin films of  $Y_2O_3:Eu^{3+}$  were deposited on quartz substrates using pulsed laser deposition (PLD). The target of  $Y_{1.96}O_3:Eu_{0.04}$  was synthesized by solid state reaction of  $Y_2O_3$  and  $Eu_2O_3$  fired at 1200°C for 12hrs and sintered at 1450°C for 48 hrs. The synthesized target was ablated using 4<sup>th</sup> harmonic Nd:YAG laser of wavelength 266 nm with a repetition frequency of 10 Hz and pulse duration 6 ns. Thin films were deposited at various substrate temperatures keeping the S-T distance at 4 cm and at an oxygen partial pressure of  $10^{-4}$  mbar. Films were also deposited at various oxygen partial pressures at a substrate temperature of 600°C and S-T distance of 4 cm. The laser fluence was kept constant through out at 2 J/cm<sup>2</sup>. The thickness of samples was measured using Dektak 6M stylus profiler. The films have thickness in the range 750-900 nm with a growth rate of 0.2-0.25 nm/s. The crystal structure of the films was analyzed using Rigaku x-ray diffractometer employing a Cu  $K_{\alpha}$  radiation (1.5414Å). The transmission spectra were recorded using JASCO V-570 UV-Vis-NIR spectrophotometer. Room temperature photoluminescence emission (PL) and excitation spectra (PLE) were recorded using Horiba Jobin Yvon Fluoromax-3 spectrometer

equipped with 150W xenon lamp. The morphology of the films was analyzed using a scanning electron microscope (SEM).

## 4C.3 Results and discussions

### 4C.3.1 X-ray diffraction studies

Figure 4.20 shows xrd patterns of  $Y_2O_3:Eu$  thin films deposited at various oxygen partial pressures ( $PO_2$ ) at a substrate temperature of  $600^\circ C$ . All the films were oriented along (222) plane which is the lowest surface energy plane. It is quite interesting that such high quality thin films are formed on amorphous substrates like quartz even though with substrate heating.

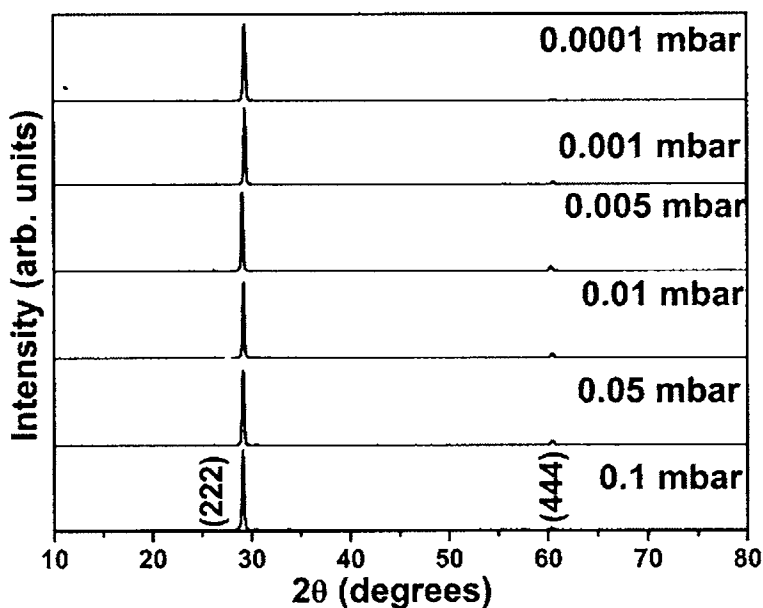


Figure.4.20. XRD patterns of  $Y_2O_3:Eu$  thin films deposited at various  $PO_2$ ;  $T_s = 600^\circ C$

The variation of Full width at half maxima (FWHM) and lattice constant with  $PO_2$  is shown in figure 4.21. FWHM decreases with increase in  $PO_2$ , reaching a minimum of  $0.17^\circ$  for film deposited at 0.05mbar  $PO_2$  and then increases with increase in partial pressure. However lattice constant increases with  $PO_2$  reaching maximum for 0.05mbar and then decreased.

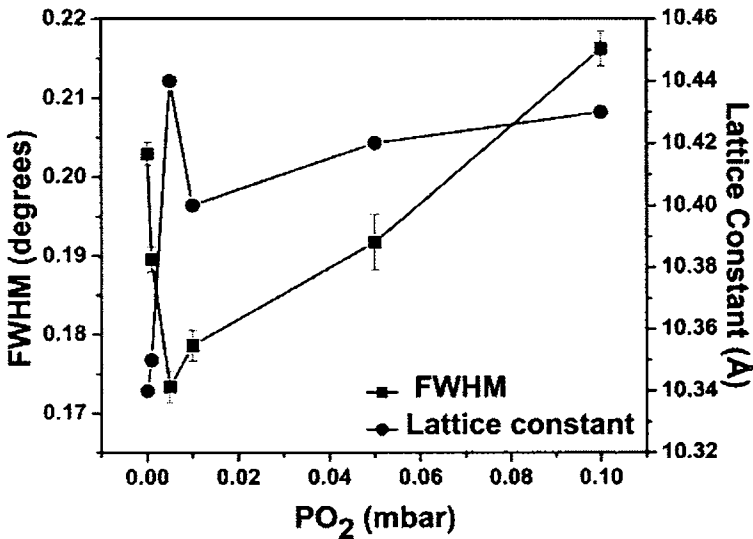


Figure.4.21. Variation of FWHM and lattice constant with  $PO_2$

Generally laser ablation of oxides in vacuum results in oxygen deficient films and in order to compensate the oxygen loss, deposition is carried out in oxygen ambient. Moreover, oxides that are highly sensitive to oxygen content, structural variations or deformations are also observed [57]. It is observed that similar to reduction in oxygen content, excess oxygen content will also create some defect levels in the lattice. In this case an optimum  $PO_2$  of 0.05 mbar is observed below and beyond which, crystallinity is decreased (FWHM increases). Interestingly at this pressure, lattice constant is observed to be

maximum, which is close to the bulk value or strain is found to be minimum at this optimum partial pressure of oxygen. Therefore similar to oxygen deficiency, excess oxygen content will also give rise to distortions in crystal structure. In bulk  $Y_2O_3$ , it is observed that the activator incorporation degree (AID) has direct influence on lattice parameter [58]. Nazarov *et al.* [58] observed that there is a linear dependence between activator incorporation degree and lattice parameter. Moreover particle size also contributes to the activator incorporation. Therefore from the figure 4.21 it is clear that observed maximum value of lattice constant is for film deposited at 0.05 mbar pressure that have minimum FWHM (maximum grain size).

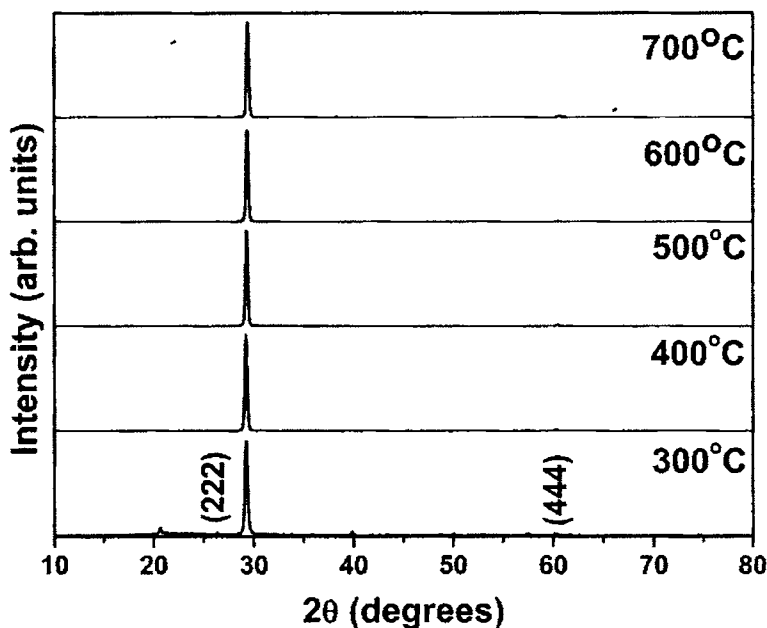


Figure.4.22. XRD patterns of  $Y_2O_3:Eu$  thin films deposited at various substrate temperatures;  $PO_2 = 10^{-4}$  mbar

This suggests a correlation between activator incorporation degree, oxygen partial pressure and particle size. At an optimum oxygen partial pressure; activator incorporation is high with an increased grain size. Figure 4.22 shows the xrd patterns of films deposited at  $10^{-4}$  mbar at various substrate temperatures. All the films were oriented along (222) plane showing that highly crystalline films could be grown even at a substrate temperature of  $300^\circ\text{C}$  on amorphous quartz substrates. As the temperature increases FWHM of the (222) peak reduces thereby increasing the crystalline quality of the deposited films. The superior crystalline quality at higher substrate temperatures could be due to the increased grain size which is often observed in high temperature thin film deposition.

### **4C.3.2 Scanning electron microscopy**

Figure 4.23 shows SEM pictures of film deposited at various deposition conditions. (a), (b) and (c) shows the films deposited at 0.0001mbar, 0.5 mbar and 0.1 mbar  $\text{PO}_2$ , at a substrate temperature of  $600^\circ\text{C}$ . Fig 4.23 (d) shows that deposited at 0.0001 mbar and  $300^\circ\text{C}$  substrate temperature. It is obvious that the film deposited at 0.05 mbar  $\text{PO}_2$  and  $600^\circ\text{C}$  shows highest crystallite size and surface looks rougher than in the other films. This is consistent with the FWHM analysis from xrd pattern as minimum FWHM is obtained for this film. Substrate temperature also has similar effect on surface morphology of as deposited thin films. As temperature increases film become more rough and crystalline. Figure 4.24 show the SEM of film deposited on quartz substrate at  $700^\circ\text{C}$  and 0.0001 mbar  $\text{PO}_2$ .

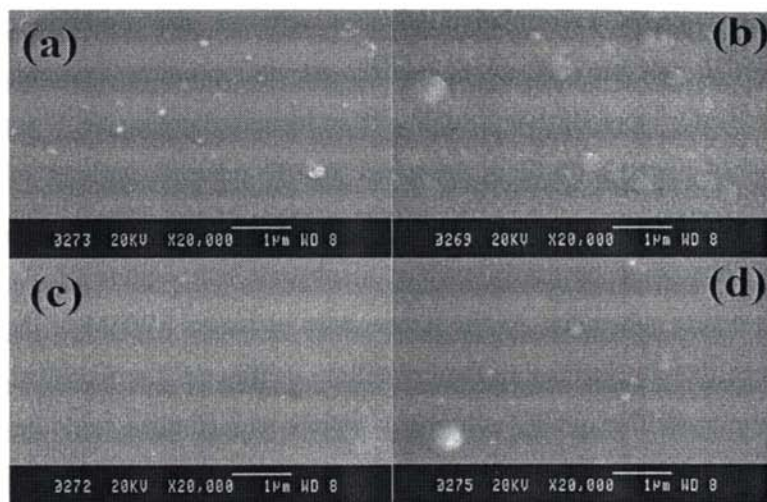


Figure 4.23. SEM micrographs of  $\text{Y}_2\text{O}_3:\text{Eu}$  thin films deposited at (a)  $600^\circ\text{C}$ ,  $10^{-4}$  mbar  $\text{PO}_2$ , (b)  $600^\circ\text{C}$ , 0.05 mbar  $\text{PO}_2$ , (c)  $600^\circ\text{C}$ , 0.1 mbar  $\text{PO}_2$  and (d)  $300^\circ\text{C}$ ,  $10^{-4}$  mbar  $\text{PO}_2$

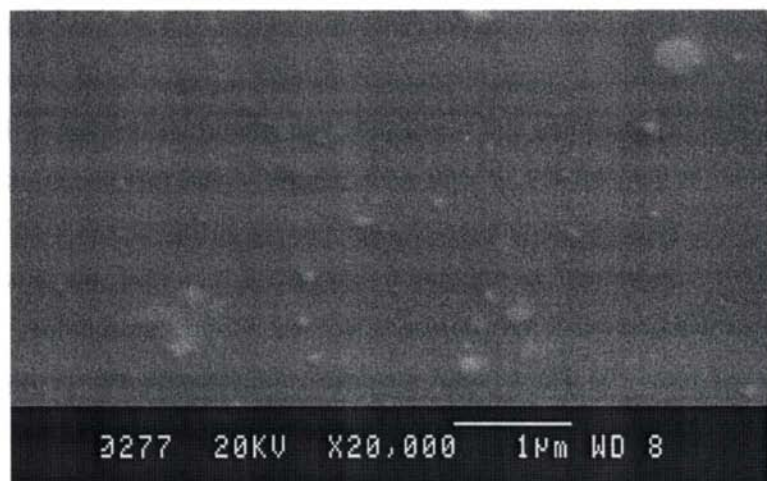


Figure 4.24. SEM micrographs of  $\text{Y}_2\text{O}_3:\text{Eu}$  thin films deposited at  $700^\circ\text{C}$ ,  $10^{-4}$  mbar

### 4C.3.3 Photoluminescence studies

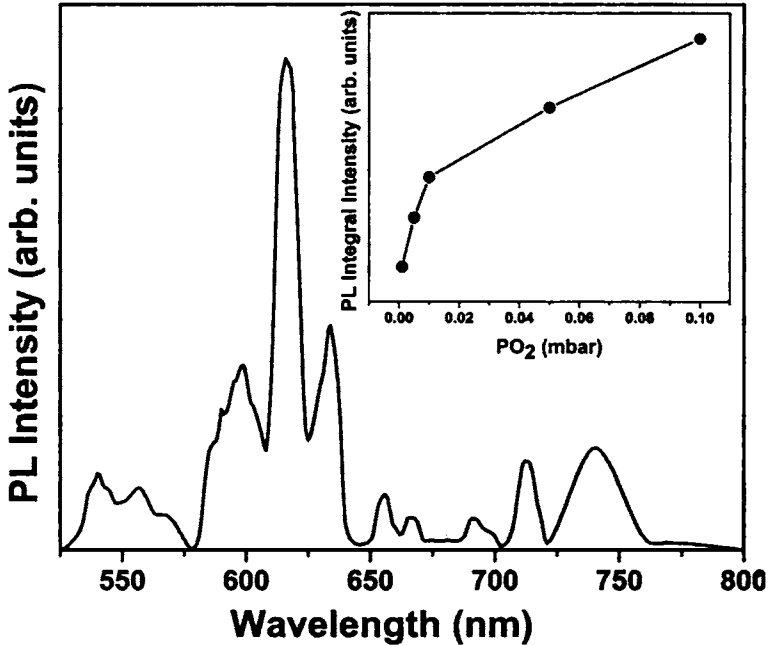


Figure 4.25. PL emission spectra of  $Y_2O_3:Eu$  thin films deposited at 0.1 mbar oxygen partial pressure. Inset shows the variation in integral intensity with  $PO_2$ ;  $T_s = 600^\circ C$

Figure 4.25 shows PL emission spectra of  $Y_2O_3:Eu$  films deposited at various oxygen partial pressure and at a substrate temperature of  $600^\circ C$ . The PL intensity was found to increase with increase in oxygen partial pressure. Thicknesses of the films were also found to increase with  $PO_2$ . The variation in deposition rate with  $PO_2$  is shown in figure 4.26. This was quite different from the results obtained for Zhang *et al.* [59] as they observed a decrease in thickness for films deposited at higher  $PO_2$  (The pressure range used by them was 0.01 - 0.1 mbar). They had also observed that the energetic plume created by the laser

ablation became shorter and narrower as the gas pressure ( $PO_2$ ) in the deposition chamber was increased [59]. In the present study, we observed an increase in plume density and length with increase in  $PO_2$ .

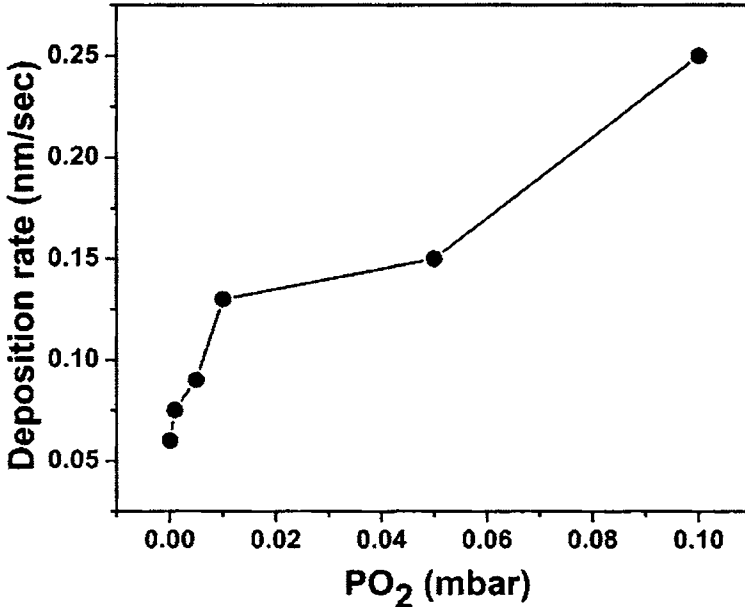


Figure 4.26. Variation of deposition rate of  $Y_2O_3$  thin films with  $PO_2$

The increase in plume intensity accompanied by an increase in emission intensity was also observed in our earlier studies in ZnO plasma [60]. With the increase in oxygen partial pressure, an increase in the density of Zn neutrals was observed [60]. In conjunction to that, an increase in Y neutrals might have occurred with the increase in  $PO_2$  which resulted in increased plasma emission intensity. The differences in the results with Zhang *et al.* [59] may be due to the difference in laser fluence (Zhang *et al.* used a laser fluence of  $5.2 \text{ J/cm}^2$ ) used.

Moreover they observed shortening of plasma plume with increase in  $PO_2$  while we observed an increase of the plasma plume.

Figure 4.27 shows PL emission spectra of films deposited at  $10^{-4}$  mbar at various substrate temperatures.

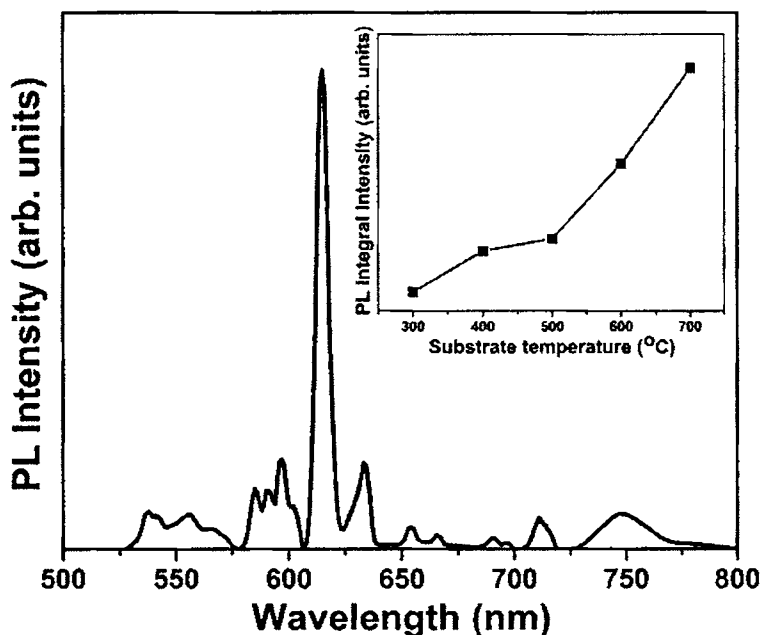


Figure 4.27. PL emission spectra of  $Y_2O_3:Eu$  thin films deposited at  $700^\circ C$ . Inset shows the variation in integral intensity with substrate temperature;  $PO_2 = 10^{-4}$  mbar

The PL shows highly resolved spectrum of  $Eu^{3+}$ , intensity maximum being observed at 615 nm. The peak emission can be attributed to  ${}^5D_0 - {}^7F_2$  transition in  $C_2$  symmetry. The mechanisms that are responsible for the PL emission are 1) direct excitation of the  $Eu^{3+}$  ion 2) excitation via a charge-transfer state between the Eu ion and neighboring O ions and 3) excitation via

the  $Y_2O_3$  host lattice.  $Eu^{3+}$  ions are supposed to replace  $Y^{3+}$  ions in the host lattice, thereby creating a charge transfer state (CTS) with neighboring oxygen atoms. These CT states absorb light from the incoming radiation, from which resonant transfer takes place to  $Eu^{3+}$  ions resulting in corresponding red PL emission. The emission spectrum consists of several lines which gives information about  $Eu^{3+}$  site symmetry in the lattice. In  $Y_2O_3$ , each Yttrium atoms are surrounded by six oxygen atoms (instead of eight) making it intrinsically a defect phosphor.

These defects can be along body diagonal ( $C_2$  symmetry), or along face diagonal of a cube ( $S_6$  symmetry) [42]. Only  $1/3^{rd}$  of the Y atoms occupy  $S_6$  symmetry while remaining  $2/3^{rd}$  of atoms occupies  $C_2$  symmetry [42]. The optical transitions in  $Eu^{3+}$  states are more likely to occur in the  $C_2$  site rather than in  $S_6$  site due to its more stable inversion symmetry of the lattice [42]. Therefore only certain magnetic dipole transitions are allowed in the  $S_6$  sites, while the electric dipole transitions are preferred in  $C_2$  sites. More over  $S_6$  site are less in number which will reduce the intensity of PL emission of magnetic dipole transitions [59].

In the observed emission spectra, the lines at 538-585 nm ( ${}^5D_1 - {}^7F_1$ ) corresponds to magnetic dipole transitions while that at 590-715 nm ( ${}^5D_0 - {}^7F_j$ ,  $j = 0$  to 4) corresponds to electric dipole transitions which include emission peak at 615 nm. In the observed spectra the relative intensity of magnetic dipole transitions are less compared to that of electric dipole transitions. Here, from the PL spectra it is concluded that  $Eu^{3+}$  ions are incorporated in to the host lattice and most of the ions predominantly replace yttrium ions with  $C_2$  symmetry.

The PLE spectra (figure 4.28) shows clearly distinct bands, one corresponding to band to band excitation of the host (212 nm) and the charge transfer band (245 nm). These excitations correspond to the peak emission wavelength at 615 nm, intensity maximum being observed for charge transfer band and resonant transfer takes place from CT states. The PLE also exhibits the high crystalline quality of the deposited films.

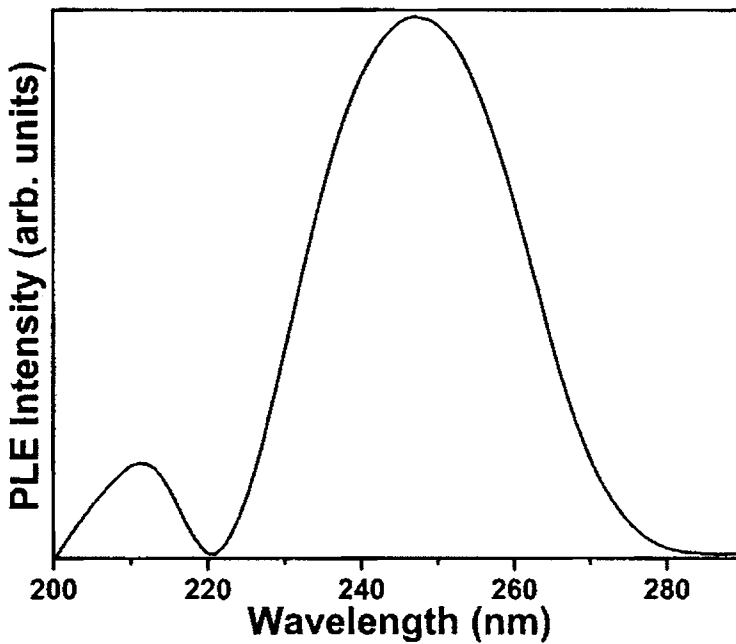


Figure 4.28. PLE excitation spectra  $Y_2O_3:Eu$  thin films deposited at  $700^\circ C$  and  $10^{-4}$  mbar  $PO_2$ . ( $\lambda_{em} = 615$  nm)

#### 4C.3.4 The CIE coordinates

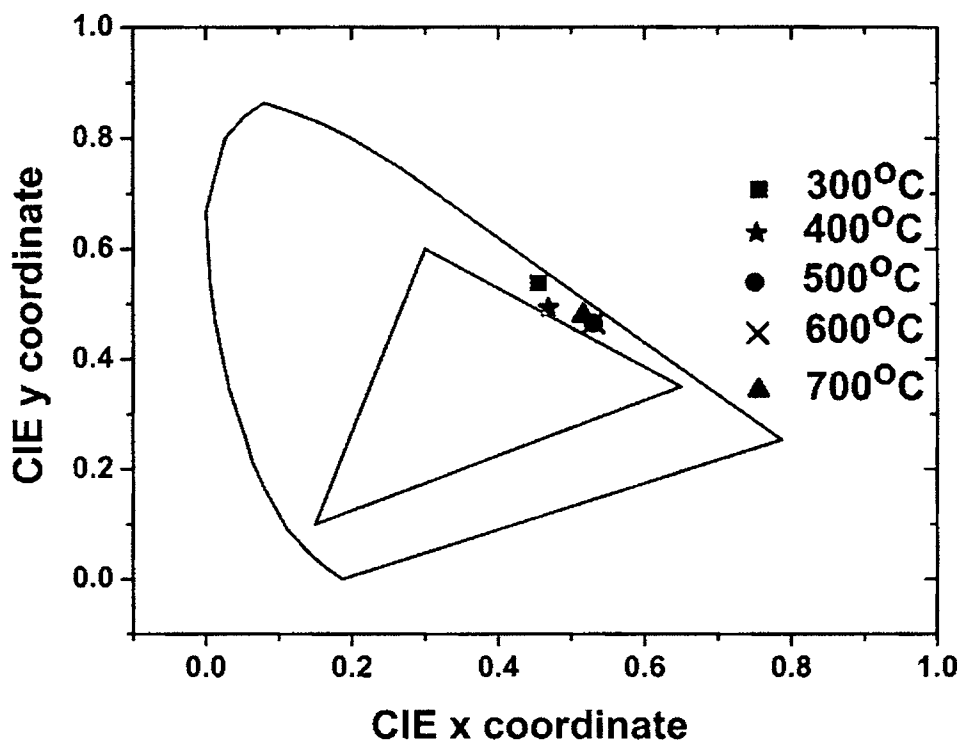


Figure 4.29. CIE chromaticity diagram of the  $Y_2O_3:Eu$  thin films deposited at various substrate temperature.

The CIE coordinates of the deposited films lie in the yellowish-orange range of the coordinate diagram (figure 4.29). It is observed that as temperature increases the coordinates shift to red region of the diagram. The coordinates of the film that showed maximum PL intensity are  $(x,y) = (0.52, 0.47)$ .

## Conclusion

Eu doped  $Y_2O_3$  thin films were deposited on amorphous fused silica substrates using pulsed laser ablation technique. The effect of oxygen partial pressure ( $PO_2$ ) and substrate temperature on the structural and optical characteristics of the deposited films were investigated. All the deposited films were crystalline, irrespective of oxygen partial pressure and substrate temperature used for deposition. Film deposited at 0.05 mbar  $PO_2$  showed better crystallinity with minimum FWHM at a substrate temperature of 600°C. All the films deposited at various substrate temperatures and different partial pressure (at 600°C) exhibited red luminescence peaking at 615 nm corresponding to  $^5D_0$ - $^7F_1$  transition in  $Eu^{3+}$ . PLE spectra exhibited two bands one corresponding to band to band excitation (212 nm) of the host and other to charge transfer band excitation (245 nm).

## References

1. T. Minami *Solid state Electron.* **47**, 2237 (2003)
2. A. H. Kitai, *Thin Solid Films*, **445**, 367(2003)
3. K. G. Cho, D. Kumar, P. H. Holloway, and R. K. Singh, *Appl. Phys. Lett.*, **73**, 3058 (1998)
4. T. Minami, T. Shirai, T. Nakatani and T. Miyata, *Jpn. J. Appl. Phys.*, **39**, L524 (2000)
5. M. L. Pang, W. Y. Shen, and J. Lin, *J. Appl. Phys.*, **97**, 033511 (2005)
6. I. K. Jeong and H. L. Park and S. Mho *Solid State Commun.*, **105**, 179 (1997)
7. T. Minami, Y. Kuroi, T. Miyata, H. Yamada and S. Takata, *J. Lumin.*, **72**, 997 (1997)

8. M. Flynn and A. H. Kitai, *J. Electrochem. Soc.*, **148**, H149 (2001)
9. T. Minami, T. Maeno, Y. Kuroi and S. Takata *Jpn. J. Appl. Phys.* **34**, L684 (1995)
10. T. Minami, Y. Kuroi and S. Takata, *J. Vac. Sci. Technol. A* **14**, 1736 (1996)
11. L. C. Williams, D. Norton, J. Budai and P. H. Holloway, *J. Electrochem. Soc.*, **151**, H188 (2004)
12. J. S. Lewis and P. H. Holloway, *J. Electrochem. Soc.*, **147**, 3148 (2000)
13. J. P. Bender, J. F. Wager, J. Kissick, B. L. Clark and D. A. Keszler, *J.Lumin.*, **99**, 311(2002)
14. V. Bondar, S. Popovich, T. Felter and J. F. Wager, *Mater. Res. Symp. Proc.* **667**, G761 (2001)
15. T. Miyata, Y. Mochizuki and T. Minami, *IEICE Trans. Electron.*, **E88**, 2065 (2005)
16. Z. Liu, X. Jing and L. Wang, *J. Electrochem. Soc.*, **154**, H500 (2007)
17. C. Baker, J. Heikenfeld and A. J. Steckl, *IEEE J. Selected top. Quantum Elec.*, **8**, 1420 (2002)
18. M. Iwasaki, D. N. Kim, K. Tanaka, T. Murata and K. Morinaga, *Sci. Technol. Adv. Mat.*, **4**, 137 (2003)
19. T. Miyata, Y. Mochisuki and T. Minami. *IEICE Trans. Electron.* **E88**, 2065 (2005)
20. T. K. Tran, W. Park, J. W. Tomm, B. K. Wagner, S. M. Jacobsen, C. J. Summers, P. N. Yocom and S. K. McClelland *J. Appl. Phys.* **78**, 5691(1995)
21. I. K. Jeong, H. L. Park and S. Mho *Solid State. Commun.* **105**, 179 (1997)

22. L. Satyanarayana, C. V. Gopal Reddy, S. V. Manoram and V. J. Rao, *Sens. Actuators, B*, **46**, 1 (1998).
23. J. Hsieh, K. T. Chu, C. F. Yu and M. S. Feng, *J. Appl. Phys.* **76**, 3735 (1994)
24. Z. Xu, Y. Li, Z. Liu and D. Wang *J. Alloys Compd.* **391**, 202 (2005)
25. S. M. Chung, S. H. Han and Y. J. Kim *Mater. Lett.* **59**, 786 (2004)
26. J. H. Kim and P. H. Holloway, *Appl. Phys. Lett.* **84**, 2070 (2004)
27. S. M. Chung and Y. J. Kim *J. Vac. Sci. Technol. A* **22**, 140 (2004)
28. R. Reshmi, K. Mini Krishna, R. Manoj and M. K. Jayaraj, *Surf. Coat. Technol.* **198**, 345 (2005)
29. K. Mini Krishna, M. Nisha, R. Reshmi, R. Manoj, A. S. Asha and M. K. Jayaraj *Materials Forum* **29**, 243 (2005)
30. Y. E. Lee, D. P. Norton and J. D. Budai *Appl. Phys. Lett.* **74**, 3155 (1999)
31. S. S. Yi, I. W. Kim, J. S. Bae, B. K. Moon, S. B. Kim and J. H. Jeong, *Mater. Lett.* **57**, 904 (2002)
32. K. Mini Krishna, G. Anoop and M. K. Jayaraj, *J. Electrochem. Soc.*, **154**, J310 (2007)
33. K. Mini Krishna, G. Anoop and M. K. Jayaraj, *J. Electrochem. Soc.*, **154**, J379 (2007)
34. Y. J. Kim, Y. H. Jeong, K. D. Kim, S. G. Kang, K. G. Lee, J. I. Han, Y.K Park and K. I. Cho *J. Vac. Sci. Technol. B* **16**, 1239 (1998)
35. B. El Dasher, Y. Pang, H. M. Miller, P. Wynblatt, A. D. Rollett, and G. S Rohrer, *J. Am. Ceram. Soc.*, **87**, 724 (2004)
36. M. Clement, E. Iborra, J. Sangrador, A. Sanz-Herva, L. Vergara, and M. Aguilar, *J. Appl. Phys.*, **94**, 1495 (2003)

37. R. Reshmi, M.Phil thesis, Cochin University of Science and Technology (2004)
38. S. H. M. Poort., D. Cetin, A. Meijerink., and G. Blasse *J.Electrochem.Soc.* **144**, 2179 (1997)
39. Y. E. Lee, D. P. Norton, C. Park, and C.M. Rouleau, *Appl. Phys. Lett.*, **89**, 1653 (2001)
40. S. L. Hones, D. Kumar, K.G. Cho, R. K. Singh, and P. H. Holloway, *Displays* **19**, 151 (1999)
41. S. H. Yanga, T. J. Hsueha and S. J. Chang, *J. Cryst. Growth*, **287**, 194 (2006)
42. K. G. Cho, D. Kumar, P. H. Holloway, and R. K. Singh, *Appl. Phys. Lett.*, **73**, 3058 (1998)
43. J. S. Bae, J. H. Jeong, S. S. Yi and J. C. Park, *Appl. Phys. Lett.*, **82**, 3629 (2003)
44. S. S. Yi, K. S. Shim, H. K. Yang, B. K. Moon, B. C. Choi, J. H. Jeong, J. H. Kim and J. S. Bae, *Appl. Phys. A*, **87**, 667 (2007)
45. S. H. Shin, J. H. Kang, D. Y. Jeon and D. S. Zang, *J. Lumin.*, **114**, 275 (2005)
46. S. H. Shin, J. H. Kang, D. S. Zang, D. Y. Jeon, S. H. Choi, S. H. Lee, Y. C. You and D. S. Zang, *Solid State Commun.*, **135**, 30 (2005)
47. S. L. Jones, D. Kumar, R. K. Singh, and P. H. Holloway, *Appl. Phys. Lett.*, **71**, 404 (1997)
48. S. Sakuma, H. Kominami, Y. Neo, T. Aoki, Y. Nakanishi and H. Mimura, *Appl. Surf. Sci.*, **244**, 458 (2005)
49. J. Hao, S. A. Studenikin and M. Cocivera, *J. Lumin.*, **93**, 313 (2001)

50. T. Minami, Y. Kobayashi, T. Miyata and M. Yamazaki, *Thin solid films*, **443**, 91 (2003)
51. A. Konrad, U. Herr, R. Tidecks, F. Kummer and K. Samwer, *J. Appl. Phys.*, **90**, 3516 (2001)
52. F. Parsapour, D. F. Kelley and R. S. Williams, *J. Phys. Chem. B*, **102**, 7971 (1998)
53. H. J. Gao, D. Kumar, K. G. Cho, P. H. Holloway, R. K. Singh, X. D. Fan, Y. Yan and S. J. Pennycook, *Appl. Phys. Lett.*, **75**, 2223 (1999)
54. D. Kumar, K. G. Cho, Z. Chen, V. Craciun, P. H. Holloway, and R. K. Singh, *Phys. Rev. B*, **60**, 331 (1999)
55. D. Kumar, J. Sankar, K.G Cho, V. Craciun and R.K Singh, *Appl. Phys. Lett.*, **77**, 2518 (2000)
56. J. Y. Cho, K.Y. Ko and Y.R. Do, *Thin Solid Films*, **515**, 3373 (2007)
57. L. Chen, *Pulsed Laser Deposition of Thin Films*, edited by D. B. Chrisey and G. K. Hubler, Wiley, New York, 1994, p. 184.
58. M.V. Nazarov, J. H. Kang, D.Y. Jeon, E.-J. Popovici, L. Muresan and B.S. Tsukerblat, *Solid State Commun.*, **133**, 183 (2005)
59. S. Zhang and R. Xiao *J. Appl. Phys.*, **83**, 3842 (1998)
60. K. J. Saji, N. V. Joshy, and M. K. Jayaraj, *J. Appl. Phys.*, **100**, 043302 (2006)
61. JCPDS card no: 11-0687
62. JCPDS card no: 36-1479

## **CHAPTER 5**

---

### **Fabrication of ACTFEL device**

---

*Thin film electroluminescent devices with  $\text{ZnGa}_2\text{O}_4:\text{Mn}$  with as active phosphor layer were fabricated on glass substrates. The active layer and top insulator were deposited using rf magnetron sputtering technique. Active layer was deposited at elevated substrate temperature with out any post deposition annealing. The dependence of phosphor layer thickness on luminance intensity, emission wavelength and color coordinates of the devices were studied keeping the thickness of the other layers constant. The emission spectra indicate the presence of Mn at different sites of the host lattice.*

## 5.1. Introduction

Currently the ACTFEL device industry widely uses sulphides as phosphor hosts. But oxides have been considered as an alternate among the researchers around the world [1, 2]. However the lack of efficient transport of high energy electrons and difficulty in obtaining good crystalline thin films has limited the interest in oxides as potential EL phosphors. Empirically, oxides have larger band gaps than sulfides and are not as capable of transporting significant current densities of hot electrons. Also oxides tend to be more refractory than sulfides and achieving good crystallinity at processing temperatures compatible with glass substrates is difficult or impossible with most oxide phosphors. Moreover, it is hard to reduce the defect density in phosphor films by a post-annealing process at high temperatures due to low softening temperature of the glass substrate [3]. However Lewis *et al.* [4] has fabricated TFEL devices using  $Zn_2GeO_4:Mn$  as active layer on glass substrates through RTA process. Typical green oxide phosphors used for ACTFEL devices are  $ZnGa_2O_4:Mn$ ,  $Zn_2SiO_4:Mn$ ,  $Zn_2GeO_4:Mn$ ,  $Zn_2Ge_xSi_{1-x}O_4:Mn$ , and  $Ga_2O_3:Mn$  [3]. Also thick dielectric electroluminescent (TDEL) devices based on oxide phosphor using various deposition techniques with post deposition treatments have been reported. The host materials used was  $ZnGa_2O_4$  [5-9],  $Zn_2SiO_4$  [10],  $Zn_2Ge_xSi_{1-x}O_4$  [11],  $Y_2O_3$  [12] and  $Ga_2O_3$  [13-15]. These films were deposited on a 0.2 mm thick  $BaTiO_3$  sheet and post deposition annealing was carried out in the temperature range 700 to 1100°C. Here  $BaTiO_3$  substrate acts as a substrate as well as an insulating layer. Further more,  $BaTiO_3$  can be annealed at much higher temperature than typical glass substrates.

In this work ACTFEL devices using  $\text{ZnGa}_2\text{O}_4:\text{Mn}$  as phosphor layer is fabricated using rf magnetron sputtering technique. The effect of active layer thickness on the electroluminescent behaviour is studied.

## **5.2. Experiment**

Green emitting Alternating current thin film electroluminescent devices were fabricated on 1 X 1" ITO/ATO/Ohara glass substrates (supplied by Planar Inc.) in the conventional MISIM structure (figure 5.1). The phosphor layer,  $\text{ZnGa}_2\text{O}_4$  doped with Mn and top insulator layer ( $\text{BaTa}_2\text{O}_6$ ) was deposited using rf magnetron sputtering technique. The phosphor layer was deposited on ATO/ITO/glass substrates at an rf power of 125 W in argon ambient of 0.015 mbar at a substrate temperature of 500°C and 600°C. The target to substrate distance was kept at 4.5 cm. Five ACTFEL devices with different active layer thickness (750 nm, 1000 nm, 1500 nm and 2000 nm at 600°C and 1500 nm at 500°C) were fabricated by varying the deposition time, keeping other parameters like rf power, rate of deposition, argon ambient constant. The top insulator  $\text{BaTa}_2\text{O}_6$  was sputtered at room temperature in an Ar ambient of 0.01mbar with substrate to target distance of 6 cm. Metal electrode (Al) of thickness 200 nm was deposited by thermal evaporation. The electroluminescent spectra (EL) were recorded using a 0.32 m monochromator (Triax- 320) coupled with Hamamatsu R928 photomultiplier tube. 1 KHz trapezoidal wave from a pulsed signal generator (Digilog Instruments Ltd.) was used to excite the fabricated TFEL devices. The sputtering parameters used for the deposition of various layers of ACTFEL devices are tabulated in table 5.1

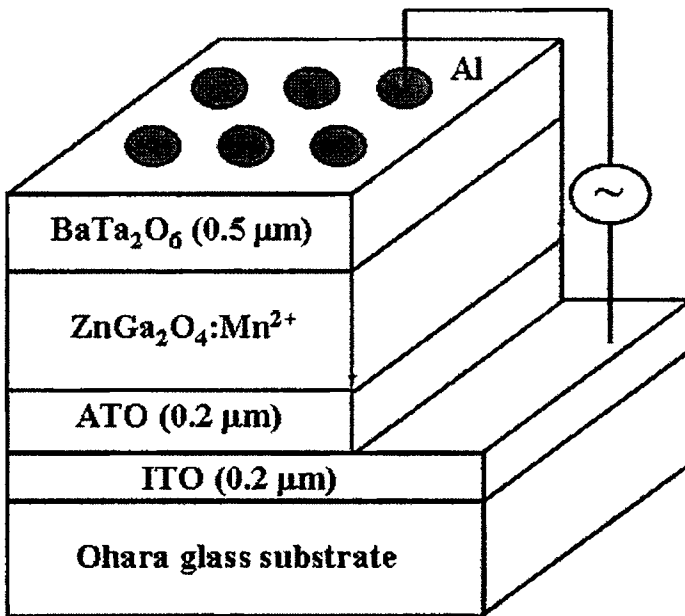


Figure 5.1 The EL device structure

## 5.3. Results and discussion

### 5.3.1 Electroluminescence studies

Figure 5.2 shows electroluminescent spectra of the devices having various active layer thicknesses when excited with 1 KHz and 40 V above threshold. The corresponding variation in EL intensity with thickness is shown in figure 5.3. The observed asymmetric spectra show a significant variation in intensity and emission wavelength with active layer thickness variation. The emission spectra can be de-convoluted in to two/three Gaussian components and the component wavelengths are tabulated in table 5.2. All devices emit light in

the green region of the visible spectra which can be attributed to  ${}^4T_1 - {}^6A_1$  transitions in  $Mn^{2+}$ .

Table 5.1. Experimental parameters

Target	ZnGa <sub>2</sub> O <sub>4</sub> :Mn powder	BaTa <sub>2</sub> O <sub>6</sub> powder
RF Power (W)	125	100
Ar gas pressure (mbar)	0.015	0.01
Base vacuum (mbar)	$6 \times 10^{-6}$	$6 \times 10^{-6}$
Substrate temperature (Ts)(°C)	500 and 600	R.T
Target to substrate distance (cm)	4.5	6

For the device ZGO-1 (device with lowest active layer thickness), the intensity of 502 nm peak was observed to be less which means that density of  $Mn^{2+}$  ions that substitute intrinsic tetrahedral  $Zn^{2+}$  site is very low. Only two emission wavelengths could be observed for ZGO-1, ZGO-2 and ZGO-3 devices and for the ZGO-4 device, all the three peaks are observed. As the thickness increases it is observed that intensity of 502 nm increases while intensity of 520 nm component remains same. For the device with active layer thickness 2000 nm (ZGO-4) emission spectra can be de-convoluted in to three wavelengths with their peak emission intensity at 499 nm, 510 nm and 520 nm. This asymmetric spectrum was also observed in corresponding PL spectra of ZnGa<sub>2</sub>O<sub>4</sub>:Mn thin films (section 4A.3.3(b)). Trans *et al.* [16] and Yu *et al.* [17] also observed similar asymmetric spectra in PL spectra. According to them these emission

lines arouse due to incorporation of  $Mn^{2+}$  at different sites in the spinel host lattice. Three emission sites were proposed namely  $Mn^{2+}$  (1) at intrinsic tetrahedral  $Zn^{2+}$  site, (2) at slightly distorted  $Zn^{2+}$  site or interstitial  $Mn^{2+}$  and (3) at octahedral  $Ga^{3+}$  site. The corresponding wavelengths were 503 nm, 515 nm and 520 nm. These observations were on the bulk powder phosphors.

Table 5.2 Characteristics of EL emission from  $ZnGa_2O_4:Mn$  ACTFEL devices operating at 1KHz

EL Device	Substrate Temperature (°C)	Thickness of phosphor layer (nm)	$V_{Th}$ (Volts)	Peak emission Wavelengths (nm)	CIE	
					x	y
ZGO-1	600	750	100	500 521	0.156	0.681
ZGO-2	600	1000	130	504 523	0.162	0.653
ZGO-3	600	1500	160	502 520	0.130	0.640
ZGO-4	600	2000	180	499 510 521	0.141	0.673
ZGO-5	500	1500	150	503 520	0.156	0.621

Therefore there is a great probability for  $Mn^{2+}$  ions to occupy all available sites. It is reported that at high temperatures  $Mn^{2+}$  at  $Ga^{3+}$  site will migrate to tetrahedral  $Zn^{2+}$  site. But in this case substrate temperature is 600°C which is comparatively low for  $Mn^{2+}$  ions to migrate to tetrahedral site which is the most appropriate site for green emission. Due to low substrate temperature,

the chance for migration from octahedral to tetrahedral sites is very low. In order to probe whether temperature or thickness is the main reason for this, device with active layer deposited at 500°C was fabricated (ZGO-5).

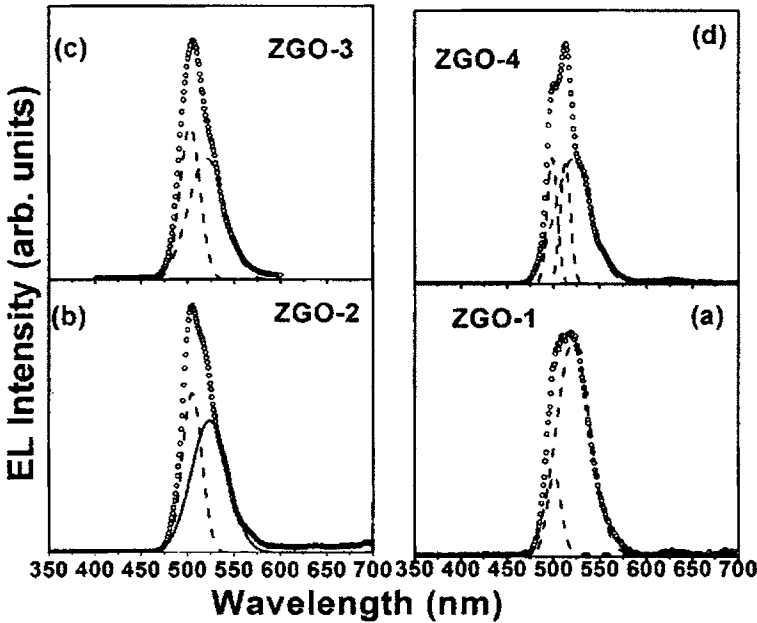


Figure 5.2 EL spectra of the ACTFEL devices at various substrate temperature and phosphor layer thickness (a) 600°C, 750 nm, (b) 600°C, 1000 nm, (c) 600°C 1500 nm, (d) 600°C, 2000 nm.

Interestingly the device showed similar emission properties but with decreased intensity, as that fabricated at 600°C with same phosphor layer thickness (figure 5.4). So it is clear that thickness of the active layer is the primary factor for this distribution of activator ions in the lattice.

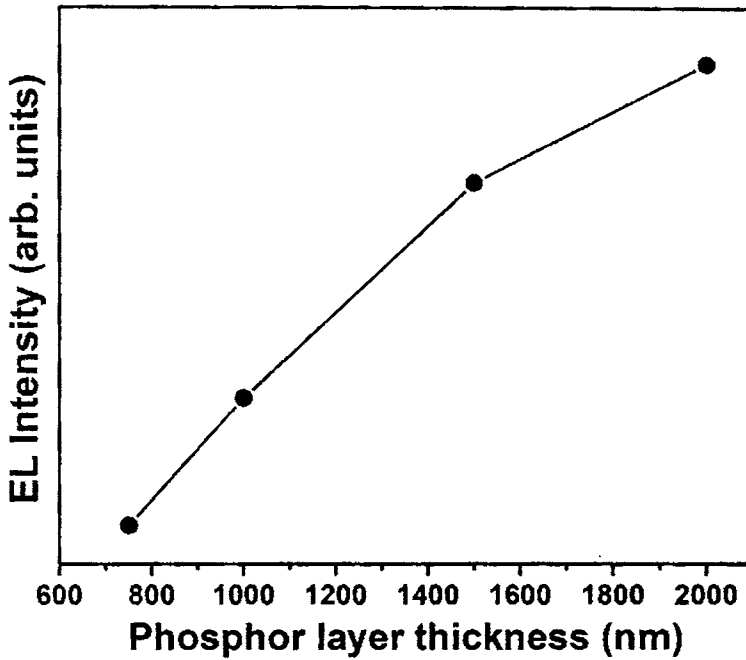


Figure 5.3 Variation in EL intensity with active layer thickness and deposited at 600°C

On comparing PL and EL, in the EL spectra, no luminescence from the host could be observed. This can be explained as follows. The dominant excitation mechanism in TFEL devices is identified as direct impact excitation of luminescent center or activator by hot electrons. A direct evidence for direct impact excitation is reported in ZnS and ZnS:Mn thin films [18, 19].

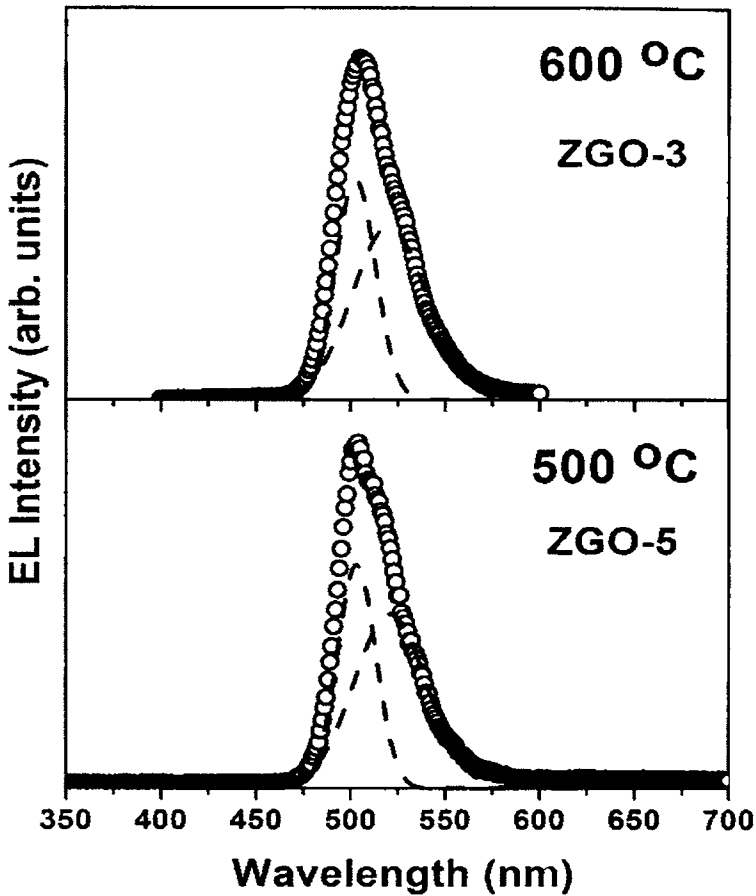


Figure 5.4 Comparison between EL devices with active layer deposited at 500°C and 600°C

However excitation mechanism involving energy transfer from the ZnS host is also proposed by Okamoto *et al.* in ZnS:TbF<sub>3</sub> and ZnS:Mn based TFEL devices [20]. They observed that in a lower time scale (< 2μs), both host and activator luminescence could be recorded. And above this time scale only activator luminescence is observed. On analyzing the life time measurements

they found that broad band emission related to host was decreasing while that of activator keeps on increasing. But in our experiment (both PL and EL) we are recording the spectra relatively in a larger time scale. Therefore to probe the exact mechanism we need to have the source that responds below  $2\mu\text{s}$ . Also EL is relatively less efficient process. Therefore to create electron-hole pairs in the host lattice and then transfer the energy to activator is rather inefficient when compared to excitation with photons.

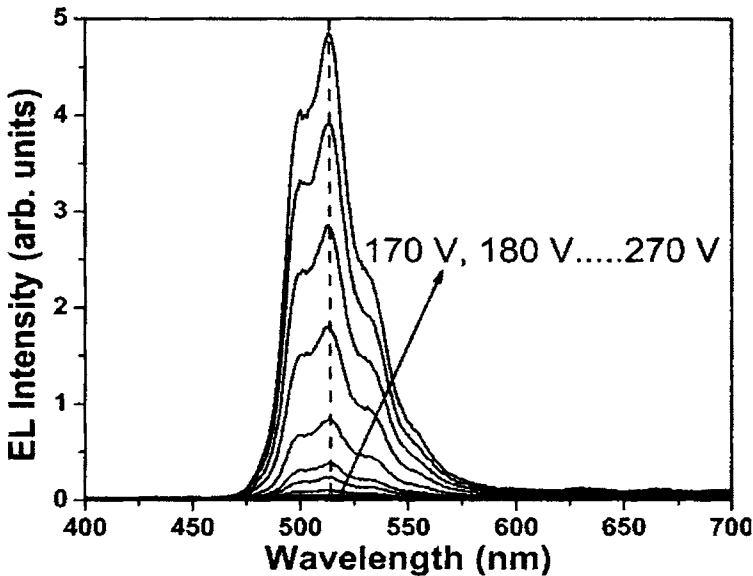


Figure 5.3 EL spectra of ZGO-4 device at various applied voltages @1 kHz

Therefore the probability for direct impact excitation is high compared to other transfer mechanisms from the host to activator. While excitation via photon, the energy of photon is equivalent or more to create an electron-hole pair in the host lattice and the probability for a transfer mechanism from the host is high along with direct excitations. But there is a saturation level for this

energy transfer and the remaining excited electrons will relax back to host valence band giving rise to broad band host emission. This could be the reason for the presence of host luminescence in PL and not in EL.

The EL spectrum of the ZGO-4 device at various drive voltage is shown in figure 5.3. From the EL spectra one can evaluate the uniformity of  $Mn^{2+}$  ions in the host lattice by analyzing the peak emission wavelength shift. If there is a considerable shift in the peak wavelength one could easily predict that  $Mn^{2+}$  distribution in the host lattice is non-uniform. But in this case all the devices did not show any shift in the peak emission wavelength. Therefore it is concluded that  $Mn^{2+}$  is uniformly distributed in the  $ZnGa_2O_4$  host.

### 5.3.2 Luminance-Voltage characteristics

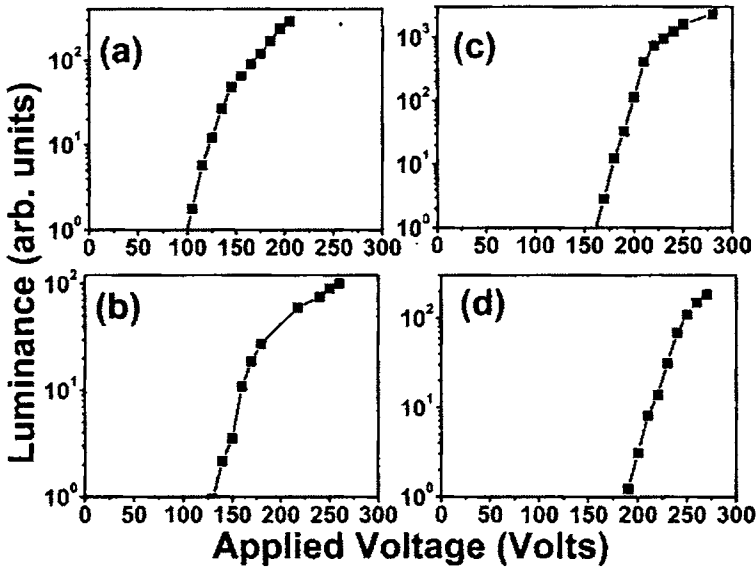


Figure 5.4 Luminance-voltage curves of the devices fabricated by varying active layer thickness. (a) 750 nm, (b) 1000 nm, (c) 1500 nm and (d) 2000 nm

Figure 5.4 shows luminance (in arb. Units) vs voltage plots of the devices fabricated. The devices show variation in threshold voltage as thickness is varied which is expected as there is a direct correlation between threshold voltage and thickness of the active layer. The device with lowest active layer thickness has minimum  $V_{th}$  and maximum for the device with highest active layer thickness.

### 5.3.3 The CIE coordinates

The CIE coordinates of the devices fabricated lie in the green region of the coordinate diagram (figure 5.5). It also shows the high purity of the emission wavelength. The coordinates are given in the table 5.2.

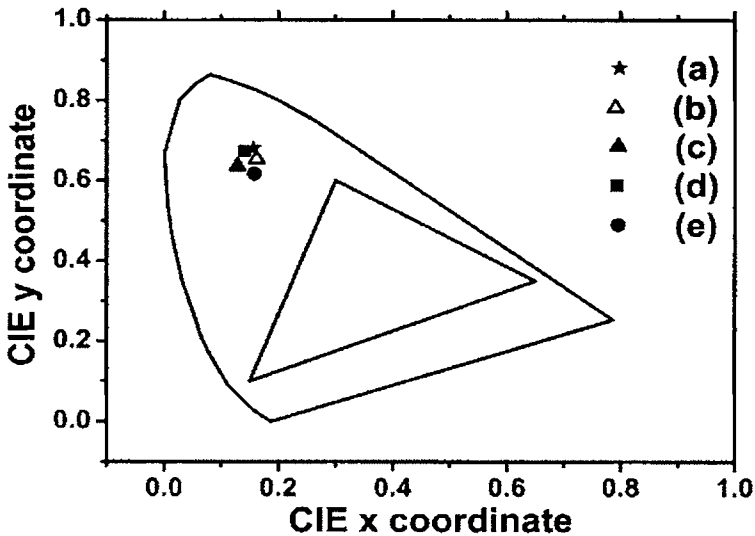


Figure 5.5 The CIE coordinates of fabricated devices (a) ZGO-1, (b) ZGO-2, (c) ZGO-3, (d) ZGO-4 and (e) ZGO-5

### 5.3.4 Charge-Voltage characteristics

Figure 5.6 shows the Q-V plot of the ZGO-3 device. Here the external charge that builds in the sense capacitor is plotted against the instantaneous voltage applied to the TFEL device. The external charge was measured using the conventional sawyer tower circuit [21]. As expected the area of the loop increases with the maximum applied voltage. The area of the loop gives the input power drawn by the device. Each of the curves correspond to maximum voltages of 200 V and 250 V and as in the general case the loop area increases with increase in applied voltage.

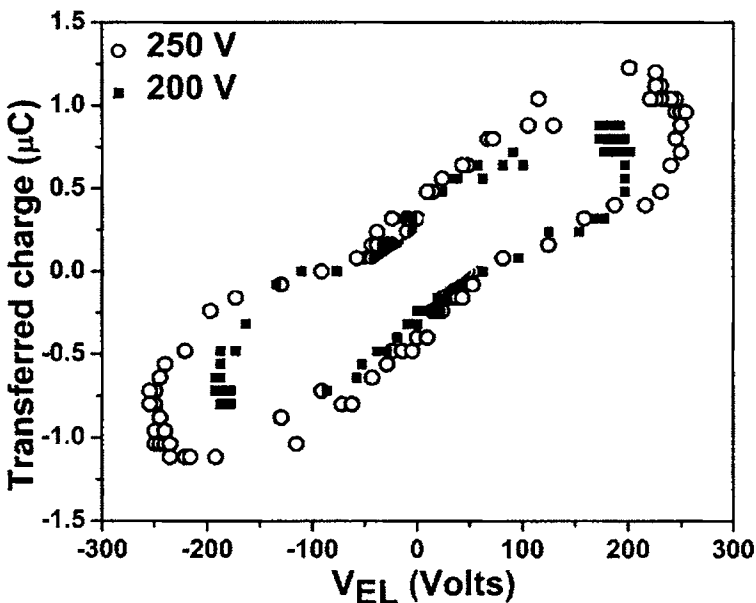


Figure 5.6 The Q-V plot of ZGO-3 device operated at  $V_{\text{max}}$  200 V and 250 V driven at 1.5 KHz

## 5.4 Zn<sub>2</sub>GeO<sub>4</sub>:Mn and Y<sub>2</sub>O<sub>3</sub>:Eu based devices

Devices with active layers Zn<sub>2</sub>GeO<sub>4</sub>:Mn and Y<sub>2</sub>O<sub>3</sub>:Eu were also fabricated. For Zn<sub>2</sub>GeO<sub>4</sub>:Mn devices, the deposition conditions are tabulated in the table 5.3.

Table 5. 3 Experimental parameters for Zn<sub>2</sub>GeO<sub>4</sub>:Mn ACTFEL device

Target	ZnO powder	Zn <sub>2</sub> GeO <sub>4</sub> :Mn powder	BaTa <sub>2</sub> O <sub>6</sub> powder
RF Power (W)	100	150	100
Ar gas pressure (mbar)	0.015	0.015	0.01
Base vacuum (mbar)	6X10 <sup>-6</sup>	6X10 <sup>-6</sup>	6X10 <sup>-6</sup>
Substrate temperature (Ts) (°C)	R.T	650	R.T
Target to substrate distance (cm)	4.5	4.5	6
Deposition time (minutes)	3, 9, 12	30,60,120	120

Devices were fabricated with and without ZnO buffer layer and varying the active layer thickness. The top insulator used was BaTa<sub>2</sub>O<sub>6</sub>. But consistent luminescence was not observed in all cases, even though the device start emission at a low voltage (40 V) when compared to ZnGa<sub>2</sub>O<sub>4</sub>:Mn devices. The emission color as observed by human eye was greenish white and the devices were burned out at comparatively low voltages (< 200 V). However the devices fabricated with ZnO buffer layer showed better performance even though those one also burned out. Since devices with ZnO buffer layer showed better reliability, devices were fabricated by increasing the ZnO buffer layer thickness

up to 250 nm (by varying the deposition time). Still no consistent electroluminescence could be obtained (even though it will start emitting light) from the devices fabricated. Several mechanisms are proposed for a device failure. One of the major device failure mechanisms is localized destructive break down (LDBD) in which break down occurs at weak points in the device area [22]. This happens due to non-uniformity in the thickness as thinner layer will feel higher electric field and will start luminesce even below threshold region and at higher voltages arcing will start around these weak points causing the breakdown in that region only. More over if there are several micro-structural defects like pin holes in the dielectric layer, which is possible during the growth via sputter deposition, the dielectric break down occurs at higher voltages causing over heating and the top electrode Al will start to sublime in to the damaged area. This will cause arcing and will result in the formation of  $\text{Al}_2\text{O}_3$  resulting in an open circuit [22]. There are two types of break down mechanisms namely self healing type which contributes to the defect isolation and propagating type that promotes the propagation of failure. The device breakdown may arise due to several reasons like (a) variation of the deposited layer thickness, (b) presence of foreign particles and pin holes and (c) heterogeneity of activator distribution [22]. The possibility of all the above mentioned reasons cannot be eliminated in the case of device breakdown in  $\text{Zn}_2\text{GeO}_4:\text{Mn}$  devices fabricated in the present study.

ACTFEL devices were also fabricated using  $\text{Y}_2\text{O}_3:\text{Eu}$  as active layer. Here  $\text{Y}_2\text{O}_3:\text{Eu}$  phosphor layer was deposited using pulsed laser deposition. The deposition parameters are tabulated in table 5.4. For the top insulator, sputtered

BaTa<sub>2</sub>O<sub>6</sub>, sputtered ZrO<sub>2</sub> and laser ablated Al<sub>2</sub>O<sub>3</sub> were used. But no electroluminescence could be observed from any of the fabricated devices.

Table 5.4 Experimental parameters for Zn<sub>2</sub>GeO<sub>4</sub>:Mn ACTFEL device

Target	Y <sub>2</sub> O <sub>3</sub> :Eu sintered target
Laser fluence	2 J/cm <sup>2</sup>
Oxygen partial pressure, PO <sub>2</sub> (mbar)	0.05, 0.1
Base vacuum (mbar)	6X10 <sup>-6</sup>
Substrate temperature (Ts) (°C)	600°C
Target to substrate distance (cm)	4
Deposition time (minutes)	60, 120

But the all the devices could with stand high voltages (300 V). Reports on ACTFEL devices based on Y<sub>2</sub>O<sub>3</sub>:Eu is scarce. Minami *et al.* has reported fabrication of TFEL device using Y<sub>2</sub>O<sub>3</sub>:Eu with a luminance of 144 Cd/m<sup>2</sup> [12, 23]. They had also reported high luminance from Y<sub>2</sub>O<sub>3</sub>:Mn devices fabricated on BaTiO<sub>3</sub> substrates [12]. In their study, the Y<sub>2</sub>O<sub>3</sub> layer was deposited using rf magnetron sputtering. But in the case of Y<sub>2</sub>O<sub>3</sub>:Mn no PL and EL could be observed in the as deposited films. But both PL and EL could be observed only after annealing at high temperatures in the range 900-1000°C [12]. They observed that only monoclinic Y<sub>2</sub>O<sub>3</sub>:Mn exhibits both PL and EL while cubic Y<sub>2</sub>O<sub>3</sub>:Eu does not exhibits PL. However no EL could be observed from the

TFEL devices fabricated even though as grown  $Y_2O_3$  was cubic [12]. Suyama *et al.* has also reported that no electroluminescence could be obtained from the  $Y_2O_3:Eu$  EL device [24]. But they observed an electroluminescence from the device fabricated with  $ZnS/Y_2O_3:Eu/ZnS$  multilayer structure. Here  $ZnS$  acts as an accelerating layer. They conclude that poor hot electron transport of  $Y_2O_3$  layer could be the reason for absence of EL from  $Y_2O_3:Eu$  device [24]. So in our case also this could be the reason for not obtaining EL from the device fabricated using  $Y_2O_3:Eu$ .

## Conclusion

Green emitting ACTFEL devices were fabricated on glass substrates in conventional MISIM structure, using  $ZnGa_2O_4:Mn$  as active layer, with out any post-deposition treatments. The active layer,  $ZnGa_2O_4:Mn$  was sputtered in Ar ambient with a substrate temperature of 500 and 600°C. The effect of active layer thickness on luminance output was studied. The EL intensity was found to increase with active layer thickness. The EL spectra shows a broad green emission and the spectra can be de-convoluted in to three peaks. These three peaks correspond to  $Mn^{2+}$  at different sites of the  $ZnGa_2O_4$  host lattice. Transferred charge was measured using Sawyer-tower circuit. The device fabricated using  $Zn_2GeO_4:Mn$  and  $Y_2O_3:Eu$  did not show any electroluminescence even though they showed excellent photoluminescence.

## References

1. T. Minami, *Solid state electron.*, **47**, 2237(2003)
2. A. H. Kitai, *Thin Solid Films*, **445**, 367(2003)
3. T. Feng, Ph.D thesis, University of Florida (2001) pp 97

4. J. S. Lewis and P. H. Holloway, *J. Electrochem. Soc.*, **147**, 3148 (2000)
5. T. Minami, Y. Kuroi, T. Miyati, H. Yamada and S. Takata, *J. Lumin.*, **72**, 997 (1997)
6. M. Flynn and A. H. Kitai, *J. Electrochem. Soc.*, **148**, H149 (2001)
7. T. Minami, Y. Kuroi and S. Takata, *J. Vac.Sci.Tech. A*, **14**, 1736 (1996)
8. T. Minami, H. Toda and T. Miyata, *J. Vac. Sci. Tech. A*, **19**, 1742 (2001)
9. T. Minami, T. Maeno, Y. Kuroi and S. Takata, *Jpn. J. Appl. Phys.*, **34**, L684 (1995)
10. T. Minami, Y. Kuroi, H. Yamada, S. Takata, T. Miyata, Proceedings of fourth Asian symposium on Information display,77 (1997)
11. T. Miyata, Y. Mochizuki and T. Minami, *IEICE Trans. Electron.*, **E88**, 2065 (2005)
12. T. Minami, Y. Kobayashi, T. Miyata and M. Yamazaki, *Thin solid Films*, **443**, 91 (2003)
13. J. Hao, Z. Lou, I. Renaud and M. Cocivera, *Thin Solid Films*, **467**, 182 (2004)...
14. T. Minami, T. Nakatani and T. Miyata, *J. Vac. Sci. Tech. A*, **18**, 1234 (2000)
15. P. Wellenius, A. Suresh, and J. F. Muth, *Appl. Phys. Lett.*, **92**, 021111 (2008)
16. T. K. Tran, W. Park, J. W. Tomm, B. K. Wagner, S. M. Jacobsen, C. J. Summers, P. N. Yocom and S. K. McClelland *J. Appl. Phys.* **78**, 5691(1995)
17. C. F. Yu and P. Lin, *J. Appl. Phys.*, **79**, 7191 (1996)
18. D. C. Krupka, *J. Appl. Phys.*, **43**, 476 (1972)

19. H. Kobayashi, S. Tanaka, H. Sasakura and Y. Hamakawa, *J. Appl. Phys.*, **52**, 1637 (1973)
20. K. Okamoto and S. Miura, *Appl. Phys. Lett.*, **49**, 1596 (1986)
21. J. F. Wager and P. D. Keir, *Annu. Rev. Mater. Sci.* **27**, 223 (1997)
22. A. N. Krasnov, *Prog. Cryst. Growth ch.*, **37**, 123 (1998)
23. T. Minami, Y. Kuroi, H. Yamada, S. Takata and T. Miyata, Eighth International Workshop on Inorganic and Organic Electroluminescence, Berlin, Germany, August 13–15, 1996, Wissenschaft & Technik Verlag, Berlin, 303 (1996)
24. T. Suyama, K. Okamoto and Y. Hamakawa, *Appl. Phys. Lett.*, **41**, 462 (1982)

# CHAPTER 6

---

## Summary and scope for future work

---

### 6.1 Summary

The dissertation is focused on synthesis of bulk oxide phosphors, thin film deposition of synthesized oxide phosphors using rf magnetron sputtering or pulsed laser deposition techniques and fabrication of alternating current thin film electroluminescent (ACTFEL) devices. The phosphors investigated for possible applications in alternating current thin film electroluminescent (ACTFEL) devices, are  $\text{ZnGa}_2\text{O}_4:\text{Mn}$ ,  $\text{Zn}_2\text{GeO}_4:\text{Mn}$ ,  $\text{Mg}_2\text{GeO}_4:\text{Mn}$  and  $\text{Y}_2\text{O}_3:\text{Eu}$ .

Green emitting  $\text{Zn}_2\text{GeO}_4:\text{Mn}^{2+}$  bulk oxide phosphor was prepared by high temperature solid state reaction. The effect of Mg incorporation on structural and luminescent properties has been studied. Structural analysis shows that only up to 25 at. % Mg, solid solution is formed and beyond this concentration, phase segregation occurs. The possible mechanism of luminescence in this particular system has been identified as energy transfer from a sub-band state to  $\text{Mn}^{2+}$  levels. Similarly red emitting  $\text{Mg}_2\text{GeO}_4:\text{Mn}^{2+}$  has been prepared using solid state reaction and the effect of Zn incorporation on structural and luminescent properties has been studied. The band gap of the  $\text{Mg}_2\text{GeO}_4:\text{Mn}^{2+}$  has been engineered via Zn addition for making it as a phosphor material for electroluminescent display applications.

Thin films of  $\text{ZnGa}_2\text{O}_4:\text{Mn}$ ,  $\text{Zn}_2\text{GeO}_4:\text{Mn}$  were deposited using rf magnetron sputtering and  $\text{Y}_2\text{O}_3:\text{Eu}$  using pulsed laser ablation (PLD) technique. The main objective of the work was to deposit these refractory oxides in to thin film form with out any post deposition annealing. Usually oxide phosphors based EL devices were fabricated on thick ceramic substrates which will act as both substrate and insulator. But fabrication of these thick dielectric electroluminescent (TDEL) devices requires high temperature post-deposition annealing, well above  $1000^\circ\text{C}$  which prevents the use of conventional glass substrates. So in the present study, thin films of oxides were deposited without any post-deposition treatments, but via substrate heating in the regime R.T- $700^\circ\text{C}$ . Crystalline films of  $\text{ZnGa}_2\text{O}_4:\text{Mn}$ ,  $\text{Zn}_2\text{GeO}_4:\text{Mn}$  and  $\text{Y}_2\text{O}_3:\text{Eu}$  was deposited on amorphous quartz substrates which also gave luminescence output. RF magnetron sputtered  $\text{ZnGa}_2\text{O}_4:\text{Mn}^{2+}$  thin film crystallizes even at room temperature. The influence of a dopant source on structural and luminescent properties of  $\text{ZnGa}_2\text{O}_4:\text{Mn}^{2+}$  thin films have been studied. Two dopant sources were chosen, one  $(\text{CH}_3\text{COO})_2\text{Mn}$  and the other was  $\text{MnO}$ . The target material showed excellent luminescence while sputter deposited thin films grown using the targets doped with two different dopant sources exhibited different luminescent characteristics. The film that deposited using  $(\text{CH}_3\text{COO})_2\text{Mn}$  as dopant source doesn't gave any luminescent output while that deposited using the target prepared using showed luminescence, with a substrate heating at and above  $500^\circ\text{C}$ . The films deposited at  $600^\circ\text{C}$  showed maximum luminescent intensity compared to that deposited at other substrate temperatures.

Finally ACTFEL devices were fabricated on ITO/ATO coated glass substrates using sputtered  $\text{ZnGa}_2\text{O}_4\text{:Mn}$  and the device showed green luminescence.

Even though  $\text{Zn}_2\text{GeO}_4\text{:Mn}$  crystallizes at lower substrate temperature, usually post-deposition annealing is carried out to get crystalline films on amorphous substrates. However, crystalline films were obtained via substrate heating and depositing on single crystalline substrates. So the present work focused on depositing crystalline  $\text{Zn}_2\text{GeO}_4\text{:Mn}$  on amorphous substrates without any post deposition treatments. Crystalline  $\text{Zn}_2\text{GeO}_4\text{:Mn}$  could be deposited on quartz substrates at a substrate temperature of  $650^\circ\text{C}$ . The optimized rf power was 150 W. In order to increase the crystalline quality of the  $\text{Zn}_2\text{GeO}_4\text{:Mn}$  films, a buffer layer of ZnO was deposited. ZnO is chosen because it is relatively easy to deposit crystalline ZnO by any method with (002) orientation. By depositing ZnO as a buffer layer, the  $\text{Zn}_2\text{GeO}_4\text{:Mn}$  films were found to be highly oriented along (220) plane. Enhanced luminescence output was observed when ZnO was used as a buffer layer for growing  $\text{Zn}_2\text{GeO}_4\text{:Mn}$  thin films on amorphous quartz substrates. Tauc plot analysis shows increased defect density in the films deposited with ZnO as buffer layer.

Red emitting  $\text{Y}_2\text{O}_3\text{:Eu}^{3+}$  thin films were deposited using pulsed laser ablation technique. High quality thin films of  $\text{Y}_2\text{O}_3\text{:Eu}$  could be deposited on amorphous quartz substrates. The films were highly oriented along its cubic (222) plane. The FWHM of (222) plane was found to be minimum for 0.05 mbar oxygen partial pressure. The effect of substrate temperature on structural and luminescent properties was also studied. The PL intensity was found to be a maximum for the film deposited at  $700^\circ\text{C}$ , which was the maximum temperature

used in this experiment.

Green emitting ACTFEL device in the conventional MISIM structure has been fabricated on glass substrates using  $\text{ZnGa}_2\text{O}_4\text{:Mn}$  as active layer. The active layer was deposited at  $600^\circ\text{C}$  with out any post-deposition treatments. The effect of thickness of active layer on device performance has been studied. The EL output of the device has been found increasing with the active layer thickness. From the EL spectrum, the emission band corresponding to three different sites of Mn has been observed and the emission varies with the active layer thickness. Host band emission was not observed in EL unlike PL emission from the thin films.

## 6.2 Scope for future work

The performance of the devices fabricated in the present study has to be enhanced manifold for practical applications. In the present study, the sputtered thin films were deposited only in Ar ambient. The effect of oxygen partial pressure ( $\text{PO}_2$ ) on thin films was not studied, even though the presence of  $\text{O}_2$  may degrade the crystalline quality of the as deposited films. The EL emission from the device fabricated using  $\text{ZnGa}_2\text{O}_4\text{:Mn}$  showed the presence of Mn at different sites. In order to enhance the luminescence output the Mn ions should replace Zn at tetrahedral sites. Therefore the device performance may be studied after annealing the device in  $\text{H}_2$  ambient just after depositing the  $\text{ZnGa}_2\text{O}_4\text{:Mn}$  layer.

Since oxide phosphors have an inherent defect of incapability of transporting high energy electrons through the lattice, usually accelerating layers are deposited in multilayers or active layer will be sandwiched between

accelerating layers. Generally sulphides are used as accelerating layers. Recently multi-component amorphous oxides have been found as suitable candidate for transparent thin film transistor applications, due to its high mobility and carrier concentration. So these oxides can be used as accelerating layers in the oxide phosphor based ACTFEL devices which could also avoid the difficulty in depositing sulphide layers in oxide based devices. The high luminance, flexible EL lamps are being fabricated on flexible oxide ceramic substrates which will open a new way in the world of flexible displays.

White light emitting diodes (w-LEDs) are considered as next generation solid state lighting systems due to their lower power consumption, high efficiency and long life time. Phosphor converted LEDs (pcLEDs) are used as white LEDs where blue LEDs are used as primary light sources for phosphors and a phosphor is used to down convert this light in to yellow light. The mixing of blue and yellow lights will give a white light. Suitable oxide phosphors may be investigated for the fabrication of white light emitting diodes.